

11-16-2015

Near-field Microwave Microscopy for Surface and Subsurface Characterization of Materials

Maria Fernanda Cordoba Erazo

University of South Florida, maria15@mail.usf.edu

Follow this and additional works at: <http://scholarcommons.usf.edu/etd>

 Part of the [Electrical and Computer Engineering Commons](#), and the [Materials Science and Engineering Commons](#)

Scholar Commons Citation

Cordoba Erazo, Maria Fernanda, "Near-field Microwave Microscopy for Surface and Subsurface Characterization of Materials" (2015).
Graduate Theses and Dissertations.
<http://scholarcommons.usf.edu/etd/5930>

This Dissertation is brought to you for free and open access by the Graduate School at Scholar Commons. It has been accepted for inclusion in Graduate Theses and Dissertations by an authorized administrator of Scholar Commons. For more information, please contact scholarcommons@usf.edu.

Near-field Microwave Microscopy for Surface and Subsurface Characterization of Materials

by

María Fernanda Córdoba Erazo

A dissertation submitted in partial fulfillment
of the requirements for the degree of
Doctor of Philosophy
Department of Electrical Engineering
College of Engineering
University of South Florida

Major Professor: Thomas Weller, Ph.D.
Jing Wang, Ph.D.
Sanjuktha Bhanja, Ph.D.
Ryan Toomey, Ph.D.
Kenneth Church, Ph.D.

Date of Approval:
October 28, 2015

Keywords: Microwave Probe, Electromagnetic Properties, High-Resolution, Imaging, Microscope

Copyright © 2015, María Fernanda Córdoba Erazo

DEDICATION

To the loving memory of my mother Gloria Erazo.

ACKNOWLEDGMENTS

I would like to express my gratitude to Dr. Thomas Weller for giving me the opportunity to conduct this research under his guidance and for always being receptive to my ideas. I am amazed that despite his great knowledge and expertise in RF and microwaves, he remains humble and kind. I want to thank my committee members Dr. Ryan Toomey, Dr. Jing Wang, Dr. Sanjuktha Bhanja, and Dr. Kenneth Church for taking the time to review this dissertation and participating in the oral defense. I also want to thank Dr. Rasim Guldiken for accepting being the chair of the oral defense.

I am grateful to my lab mates in 412 and colleagues for their friendship and interesting conversations. Thanks to I. Nassar, S. Gupta, E. Rojas, M. Grady, E. Benabe, D. Lugo, A. Menon, E. Gonzalez, D. Hawatmeh, A. Dey, R. Ramirez, A. Qaroot, and M. Abdin. I would like to thank Arya Menon for reading this dissertation and providing valuable feedback. Special thanks to Juan De Dios Castro for providing The PDMS-Ba_{0.55}Sr_{0.45}TiO₃ samples and helping with the scanning electron microscopy images. I also want to thank Czeslaw Tarnawa and Tony Villacana in the Engineering Machine Shop for their valuable help with the machining of the pieces used throughout the development of this research. Special thanks to Robert Tufts, Richard Everly, and Sclafani Louis-Jeune at the Nanotechnology Research and Education Center for their advice and help regarding material processing and characterization.

I will be forever thankful to my mother Gloria Erazo, from whom I learnt with love and kindness the importance of family and education as pillars in life, and the value of courage and perseverance to make dreams come true. I am very thankful to my uncles Edgar Erazo and Hermes Erazo for their love, understanding, and support despite the distance. Last but not least, I want to sincerely thank Horacio Coy, without his support this endeavor would not have been possible.

TABLE OF CONTENTS

LIST OF TABLES	iii
LIST OF FIGURES	iv
ABSTRACT.....	viii
CHAPTER 1 : INTRODUCTION	1
1.1 Overview and Motivation	1
1.2 Research Objectives	5
1.3 Contributions	5
1.4 Dissertation Organization	7
CHAPTER 2 : LITERATURE REVIEW AND BACKGROUND	8
2.1 Introduction	8
2.2 Near-Field Microwave Microscopy	8
2.3 Evanescent Fields.....	12
2.4 Spatial Resolution of a Near-Field Microwave Microscope.....	16
2.5 Characterization of Materials Using Near-Field Microwave Microscopy	18
2.5.1 Surface Characterization of Solids and Liquids	19
2.5.2 Sub-surface Characterization of Solids	24
2.6 Cavity-Perturbation Theory and Modeling of Tip-Sample Interaction	28
2.7 Resonant Properties and Coupling of a Resonant Probe	33
2.7.1 One-Port Resonator.....	37
2.7.2 Two-Port Resonator	37
2.8 Conclusion	38
CHAPTER 3 : DIELECTRIC RESONATOR-BASED MICROWAVE MICROSCOPE	40
3.1 Introduction	40
3.2 Experimental Setup	42
3.3 Dielectric Resonator-Based Probe Design.....	44
3.4 Distance Following Feedback System.....	51
3.5 Conclusion	52
CHAPTER 4 : COAXIAL TRANSMISSION LINE RESONATOR-BASED MICROWAVE MICROSCOPE.....	53
4.1 Introduction	53
4.2 Experimental Setup	53
4.3 Coaxial Transmission Line Resonator-Based Probe Design and Distance Following Feedback System	55
4.4 Electrochemical Etching of the Tungsten Tip	62
4.5 Conclusion	65

CHAPTER 5 : CAPABILITIES OF THE DR-BASED NFMM AND THE COAXIAL TRANSMISSION LINE RESONATOR-BASED NFMM.....	67
5.1 Note to Reader	67
5.2 Introduction	67
5.3 Material Differentiation.....	68
5.3.1 Differentiation of Bulk Dielectric Materials	68
5.3.2 Differentiation of Liquids	70
5.3.3 Differentiation and Detection of Subsurface Materials.....	76
5.4 Imaging Capability	78
5.5 Conclusion	87
CHAPTER 6 : CHARACTERIZATION OF PRINTED MATERIALS AND DEVICES, AND FLEXIBLE CERAMIC COMPOSITES USING NFMM.....	89
6.1 Note to Reader	89
6.2 Introduction	89
6.3 Characterization of Direct Digital Additive Manufactured Conductive Materials and Thick Film Resistor	91
6.3.1 Non-contact Characterization of Polymer Thick Film Printed Resistors	91
6.3.2 Non-Contact Characterization of Conductive Inks	99
6.4 Characterization of Flexible Ceramic Composites.....	106
6.5 Conclusion	110
CHAPTER 7 : SUMMARY AND RECOMMENDATIONS.....	112
7.1 Summary	112
7.2 Recommendations	113
REFERENCES.....	115
APPENDIX A: COPYRIGHT PERMISSIONS	121
A.1 Permissions for Chapter 1	121
A.2 Permissions for Chapter 2.....	125
A.3 Permissions for Chapter 3.....	130
A.4 Permission to Use Miscellaneous Materials from Previous Publication in European Microwave Conference Included in Chapter 5	131
A.5 Permission to Use Miscellaneous Materials from Previous IEEE Publications Included in Chapter 6.....	132
ABOUT THE AUTHOR	END PAGE

LIST OF TABLES

Table 2-1	Comparison of some scanning probe microscopy techniques used for materials characterization.	12
Table 2-2	Summary of lateral spatial resolution achieved by several NFMM.	17
Table 2-3	Summary of several NFMM probe design capabilities.	28
Table 2-4	Z_{in} , F_r and Q for series and parallel resonator topologies	34
Table 3-1	Equivalent lumped circuit parameters of the DR-based microwave probe.	47
Table 4-1	Voltage used during electrochemical etching of tungsten tips.	65
Table 5-1	$\Delta\epsilon'_r$ of the DR-based and coaxial transmission line resonator-based NFMM designs.	69
Table 5-2	Permittivity and loss tangent of liquids used (measured a 5.72 GHz using the 8570B Agilent Probe).	71
Table 5-3	$\Delta\epsilon'_r$ of the DR-based NFMM.	73
Table 6-1	Signal-to-noise ratio at different tip-sample distances.	94
Table 6-2	Resistor dimensions and computed electrical resistance.	98
Table 6-3	Electrical conductivity of standard conductive samples measured using a Jandel RM3000 four point probe.	101
Table 6-4	Roughness measurement method comparison.	105
Table 6-5	Electrical conductivity measurement method comparison.	105

LIST OF FIGURES

Figure 1-1	Examples of 3D printed microwave devices.....	3
Figure 1-2	Examples of microwave components that use flexible PDMS-CaTiO ₂ composite material..	4
Figure 2-1	Illustration of an NFMM.....	9
Figure 2-2	Illustration of a resonant microwave probe when an MUT is placed at a distance d from the tip.....	11
Figure 2-3	Illustration of the (a) traveling wave described by (14) and (b) evanescent wave described by (15).	15
Figure 2-4	E-field plots of the tip-sample interaction for different tip radius.....	18
Figure 2-5	Microstrip line resonator probe (left) and NFMM image of a hard drive disk showing regions with higher permeability (darker regions) (right) from [47] © 1999.....	20
Figure 2-6	Cavity coaxial resonator-based NFMM from [7] © 1998.	21
Figure 2-7	Coaxial transmission line-based NFMM (left) and Q versus sheet resistance of a variable-thickness aluminum thin film (right) from [16] © 1998.....	23
Figure 2-8	Testing sample and measured phase of reflection coefficient image at different operating frequencies from [27] © 2011.	25
Figure 2-9	Experimental setup of the TM-NFMM and measured topography and S_{21} parameters images of the testing sample (bulk silicon with varying doping profile along the cross-section) from [45] © 2014.	26
Figure 2-10	Lumped-element circuit model of a parallel RLC resonator interacting with a conductive sample through C_x	32
Figure 2-11	(a) Lumped-element circuit model and (b) frequency response of a one-port parallel RLC resonator.....	34
Figure 2-12	Effect of C_c on the coupling of a parallel RLC resonator to a source.....	36
Figure 2-13	Magnitude of input impedance versus frequency for a 1-port RLC parallel resonator coupled to a source through a capacitor $C_c=0.16$ pF.	37
Figure 2-14	Insertion loss versus frequency for a 2-port RLC parallel resonator.	38

Figure 3-1	DR-based NFMM.....	41
Figure 3-2	(a) Illustration of the DR-based microwave microscope.	43
Figure 3-3	(a) Schematic of the dielectric resonator (DR)-based near-field scanning microwave probe..	45
Figure 3-4	Lumped-element circuit model of the DR-based microwave probe and (a) insulating sample (b) metallic sample.	46
Figure 3-5	(a) Schematic of the tip-insulating sample interaction.	48
Figure 3-6	(a) Schematic of the tip-metallic sample interaction.	49
Figure 3-7	Schematic of the co-simulation of the microwave probe.....	50
Figure 3-8	Simulated and measured S_{21} vs. frequency of the DR-based microwave probe.	51
Figure 3-9	Measured and simulated S_{21} parameters of the DR-based probe when the tip is far from and in contact with a conductive sample.....	52
Figure 4-1	(a) Illustration of the coaxial transmission line resonator-based NFMM experimental setup.....	54
Figure 4-2	Schematic of the coaxial-based probe.	55
Figure 4-3	(a) Schematic of the distance following feedback system.	57
Figure 4-4	Measured output electrical current of the quartz tuning fork vs. frequency with and without a parasitic compensation circuit.	58
Figure 4-5	(a) Frequency spectra of the tuning fork for $L=1900\text{ }\mu\text{m}$ and different values of h distance.	58
Figure 4-6	Output voltage of the quartz tuning fork vs. tip-sample distance.....	59
Figure 4-7	(a) Micrograph showing the direction of scan for profile measurement of a $\text{Ba}_{0.5}\text{Sr}_{0.5}\text{TiO}_3$ trace on alumina substrate.....	60
Figure 4-8	Schematic of the co-simulation of the microwave probe.....	61
Figure 4-9	(a) Simulated S_{11} parameter vs. frequency for different TG values.	62
Figure 4-10	Illustration of the electrochemical etching of a tungsten tip.	63
Figure 4-11	Illustration of the experimental setup used for electrochemical etching of tungsten tips.	64
Figure 4-12	SEM micrographs of fabricated tips (a) 1, (b) 2, (c) 3 and (d) 4.....	65

Figure 5-1	(a) F_r and (b) Q of the DR-based microwave probe using tip of apex radius of 25 μm for different insulating bulk samples.	69
Figure 5-2	(a) F_r and (b) Q of the coaxial transmission line resonator-based microwave probe using tip of apex radius of 10 μm for different insulating bulk samples.	70
Figure 5-3	Lumped-element circuit model of the tip-liquid interaction for $d > 0$ mm (non-contact), and for $d < 0$ mm (probe tip submerged in the liquid).	72
Figure 5-4	(a) Measured F_r vs. d plot for different low loss liquids.	73
Figure 5-5	(a) Measured F_r vs. d plot for different lossy liquids.	74
Figure 5-6	Simulated F_r (a) and Q (b) of the lumped-element circuit vs. C_s for low-loss liquids.	75
Figure 5-7	(a) Schematic of the simulated sample.	77
Figure 5-8	(a) Measured F_r vs. tip-sample distance for different bulk substrates coated with a 5 μm thick parylene-C layer.	78
Figure 5-9	(a) MMIC phase shifter scan area.	80
Figure 5-10	Line profile along the 10 μm wide microstrip line.	81
Figure 5-11	MMIC detector and scan area.	81
Figure 5-12	(a) Illustration of the tip, MMIC detector and mineral oil seen from the side.	82
Figure 5-13	(a) Illustration of the tip and MMIC detector seen from the side.	82
Figure 5-14	Line profile along the 10 μm wide microstrip line for the tip in air and oil.	83
Figure 5-15	Electric field distribution of the tip-mineral oil interaction for non-contact operation (left) and tip immersed in mineral oil (right).	83
Figure 5-16	Resonance frequency and quality factor plots for parylene-C/Au/glass sample obtained using tips with apex radius of (a)-(b) 10 μm and (c)-(d) 4 μm	85
Figure 5-17	Normalized F_r (a) and (b) profile scans along x using tip with apex radius of 10 μm and 4 μm	86
Figure 5-18	Electric field distribution of the tip-sample interaction.	86
Figure 5-19	Illustration of the determination of the A_w using a measured profile.	87
Figure 6-1	Printed resistor illustration (a) and micrograph (b).	92

Figure 6-2	(a) Q and F_r plot versus d for DuPont 7082..	93
Figure 6-3	Topography of the printed resistor obtained through NFMM.....	95
Figure 6-4	Profiles along the width (a) and length (b) of the resistor using NFMM.....	96
Figure 6-5	Electrical resistance image and equivalent lumped-element circuit model.	97
Figure 6-6	Simulated electrical current density plot on the resistor.	99
Figure 6-7	SEM micrographs of the cross section of CB028 around the middle of the trace (a) and close to the side edge of the trace (b).	100
Figure 6-8	Photograph of the additive manufactured CB028 slot ring resonator.....	100
Figure 6-9	Calibration plot.....	101
Figure 6-10	Topography (left) and conductivity (right) images of CB028.	102
Figure 6-11	(a) SEM of the cross section of a CB028 sample.	104
Figure 6-12	(a) Schematic of the microstrip line using a composite conductive material.	106
Figure 6-13	Fork output voltage versus d for PDMS- $\text{Ba}_{0.5}\text{Sr}_{0.5}\text{TiO}_3$ 49% with and without parylene-C coating.	107
Figure 6-14	(a) Surface topography and (b) F_r image of PDMS- $\text{Ba}_{0.55}\text{Sr}_{0.45}\text{TiO}_3$ 49% coated with a 10 μm thick parylene-C layer.	109
Figure 6-15	System noise measured at $d= 100$ nm.	110

ABSTRACT

This dissertation presents an investigation on the capabilities of Near-Field Microwave Microscopy (NFMM) for the characterization of surface and subsurface materials. Subsurface characterization refers to the detection, differentiation and imaging of dielectric, and metallic features that are coated with an insulating layer. The design, simulation and modeling, and testing of a dielectric resonator (DR)-based NFMM and a coaxial transmission line resonator-based NFMM are discussed in detail in this work. Additionally, materials differentiation and imaging capabilities of each microscope are examined using several bulk samples, liquids, GaAs MMIC circuits, and gold/glass testing patterns.

The 5.7 GHz DR-based NFMM uses a microwave probe that consists of a commercial gold-coated probe tip coupled to a DR through a non-resonant microstrip line. The probe is enclosed in an aluminum cavity to preserve the quality factor of the probe ($Q=986$) and therefore to enhance its sensitivity. The development of a lumped-element model of this DR-based probe is discussed in this work. Characteristics of this design are its high Q and the ability to resolve differences in permittivity (ϵ'_r) of insulating bulk samples and liquids as small as $\Delta\epsilon'_r=1.75$ and $\Delta\epsilon'_r=0.04$, respectively. The imaging capabilities of this design were verified using a GaAs MMIC phase shifter. It was found that a 10 μm wide microstrip line is successfully resolved and that the spatial resolution of the microscope is 50 μm when using a tungsten tip with an apex radius of 25 μm . Additionally, measurement of the electrical resistance of an additive manufactured resistor was measured using the DR-based NFMM without the need of contacts. The percent difference between the electrical resistance measured using the DR-based NFMM and a four-point probe is 9.6%. Furthermore, the DR-based NFMM allows simultaneous imaging of topography and RF electrical conductivity of rough thick films without the need of an additional distance sensor; this ability is demonstrated for a rough CB028 thick film.

The 5GHz coaxial resonator transmission line-based NFMM employs a half-wavelength coaxial transmission line resonator terminated in a sharp tungsten tip as the microwave probe. A quartz-tuning fork based distance following feedback system is integrated with the microwave probe in order for the NFMM to operate in non-contact mode. The Q of the probe is degraded by 30% ($Q=55$) due to the presence of the quartz tuning fork. Despite the low Q, this NFMM is able to differentiate several insulating bulk samples ($3.8 < \epsilon'_r < 25$) even if they are coated with an insulating layer of thickness similar to the apex radius of the tungsten tip. Finally, the coaxial resonator transmission line-based NFMM is able to image subsurface permittivity distribution of a flexible polymer-composite PDMS- $\text{Ba}_{0.55}\text{Sr}_{0.45}\text{TiO}_3$ 49% which is coated with 10 μm thick parylene-C layer. Measurements performed at a tip-sample distance of 100 nm reveal that within an area of 50 μm x 50 μm , the relative permittivity of the polymer-composite is not constant but varies between 6.63 and 11.78.

CHAPTER 1 : INTRODUCTION

1.1 Overview and Motivation

As the demand for higher operating frequencies and higher integration density of devices and systems increases, an understanding of the electromagnetic properties of the materials used becomes indispensable. Electromagnetic properties of materials have been successfully measured in the microwave frequency region using transmission line methods [1, 2], resonant cavities [3, 4], and open-ended coaxial probes [5]. However, these methods provide an averaged value of the electromagnetic properties over a macroscopic area that is on the order of the wavelength at the operating frequency. For example, the area of study for a cavity with a resonance frequency of 5 GHz is about 6 cm x 6 cm. Local variations, which significantly impact the performance of miniaturized devices, especially as frequency increases, are not resolved.

Near-field microwave microscopy (NFMM) is a metrology tool able to image the electromagnetic properties of materials (ϵ_r , μ_r , σ) on scales much shorter than the wavelength at the operating frequency [6]. Since the microwaves are able to penetrate non-conducting materials, NFMM enables the characterization of materials under test (MUT) at the surface and in the subsurface, which is of importance not only in the characterization of multilayer structures and subsurface defect detection, but also in biomedical applications such as imaging of tumor cells. Thus, NFMM contributes in areas such as biology, materials science, and fundamental physics. Moreover, localized study of electromagnetic properties through NFMM contributes to the understanding of dependence of inhomogeneities and defects of the materials on the performance of microwave devices and systems.

Over the last two decades, several NFMMs have been successfully used for the characterization of bulk materials [7-9] and thin films [10-18]. Tunability of BaSrTiO₃ ferroelectric thin films has been studied in [19]. A common characteristic of the materials studied so far is that they are flat and their surface is smooth which facilitates the NFMM imaging over the sample. However, materials such as conductive DuPont CB028, insulating ULTEM, and insulating Acrylonitrile Butadiene Styrene (ABS) used in additive manufactured devices have higher roughness ($\approx \mu\text{m}$) [20]. Direct Digital Manufacturing (DDM) is a popular 3D additive manufacturing process used in the development of low cost complex microwave structures such the periodic spiral antenna [21] and band-pass filter [22] shown in Figure 1-1(a) and (b). One of the challenges of the characterization of these materials using NFMM is that the high roughness of the materials limit the use of certain NFMMs such as the commercial available atomic force microscope (AFM)-based NFMM considering the limited z-travel of most common piezotransducers [23]. Thus, it is required to integrate a distance-following feedback system compatible with the rough nature of the sample with the NFMM so that the microscope can operate in close proximity to the sample ($\approx \text{nm}$) in order to achieve high resolution and sensitivity while preserving the microscope and sample integrity. Another challenge involved in the NFMM characterization of printed materials and structures is that the available models of the NFMM-sample interaction are approximations that consider the sample to be flat and uniform. However, printed materials are non-uniform in addition to being rough. For example, once cured, printed DuPont CB028 is comprised of silver flakes, solvent, and air voids which are unevenly distributed across the sample.

Other materials compatible with additive manufacturing processes and suitable for microwave components are polymer-ceramic composites such as PDMS loaded with BaTiO₃, NdTiO₃, Ba_{0.55}Sr_{0.45}TiO₃, and MgCaTiO₂. Polymer-ceramic composites are materials that have enormous potential applications in microwave devices not only because of their flexibility but also because they are low cost, low loss, and a wide range of permittivity ($3 < \epsilon'_r < 23$) can be obtained by controlling the sintering process and the amount of the ceramic material used [24].



(a)



(b)

Figure 1-1 Examples of 3D printed microwave devices. (a) Sinuous cavity-backed periodic spiral antenna taken from [21] © EurAAP 2015; used with permission. (b) 2.45 GHz band-pass filter from [22] © 2015.

Figure 1-2(a) shows a 4.2 GHz flexible patch antenna using a PDMS-MgCaTiO₂ as substrate [25]. Figure 1-2 (b) presents a 3D miniaturized printed balun that has multiple layers that include ABS in the bottom and PDMS-MgCaTiO₂ 25% in the middle layer and top layers [26]. To the best of the author's knowledge, characterization of flexible polymer-ceramic using NFMM has not yet been reported. NFMM imaging of dielectric constant and topography of flexible polymer-ceramics can contribute to the understanding of the microstructural material formation, which will contribute to the understanding of the performance of the microwave component.

The study of flexible polymer-ceramic composites using NFMM also involves the challenge of exploring the capabilities of the NFMM for subsurface characterization of materials since it has been found that the NFMM is able to operate in non-contact mode if an insulating flexible layer is deposited on the composite. This presents a major challenge since previous research on materials characterization of bulk materials and thin films using NFMM has been mostly dedicated to the imaging of the surface electromagnetic properties of these materials. Subsurface characterization of materials is not only of relevance for the study of ceramic composites but also for quality control and defect detection in microwave integrated circuits. For instance, microelectronics circuits are shielded from corrosion and

contamination using a passivation layer in order to prevent degradation of circuit performance and extension of operational lifetime.

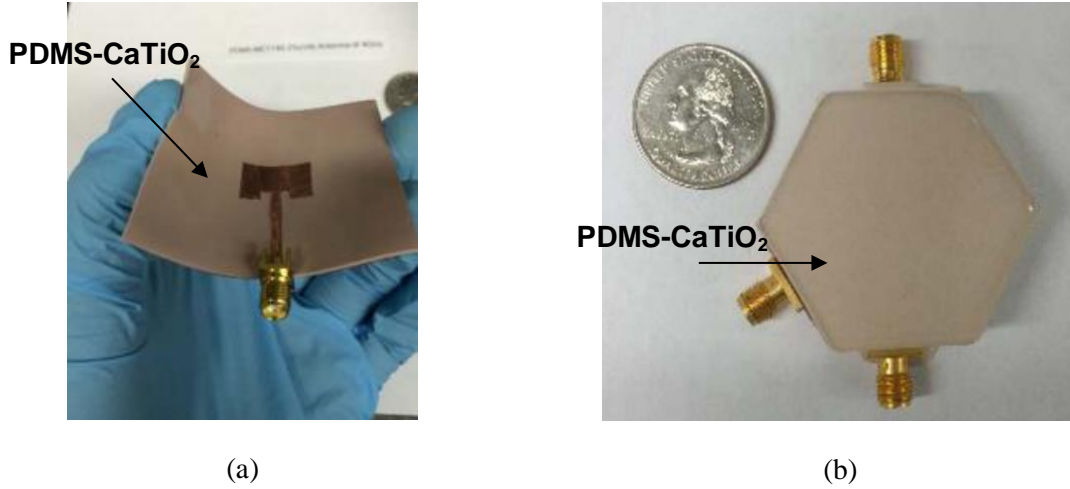


Figure 1-2 Examples of microwave components that use flexible PDMS-CaTiO₂ composite material. (a) 4.2 GHz Patch antenna from [25] © 2015. (b) Miniaturized 3D printed balun from [26] © 2015.

A limitation of the passivation layer is that it restricts the electrical and morphological characterization that can be carried out on the materials being coated. Typical techniques employed for characterizing the topography and elemental composition of the materials underneath the surface, such as scanning electron microscopy (SEM) and energy dispersive X-ray spectroscopy (EDS), are destructive and require the sample to be diced in order to study the cross section. Typical methods for measuring electrical properties of materials such as the open ended coaxial probe and four-point probe method require the probe to be in contact with the sample and measurement accuracy is limited by the size and thickness of the sample. Few works have explored the capabilities of NFMM for subsurface characterization of materials. Most of the research on subsurface imaging using NFMM has been focused on the identification and imaging of metallic features coated by conductive [27] and insulating layers [28, 29]. However, there is a lack of information on the study of the electromagnetic properties of coated samples using NFMM. In NFMM, the extension of the evanescent fields in the material is controlled by

the probe tip-sample distance and the probe-tip size. Investigation of the influence of these parameters on the subsurface detection capability of NFMM can contribute to the measurement of the electromagnetic properties of materials below the material's surface.

1.2 Research Objectives

Despite the research available regarding the characterization of materials using NFMM, there is still a need for continuing the investigation and understating of capabilities of NFMM for the study of new materials that are present in complex microwave structures such as additive manufactured devices, multilayered circuits, and flexible components. Thus, the main objective of this work is to examine the capabilities of NFMM for surface and subsurface characterization of smooth and rough materials.

Examination of the NFMM capabilities requires the design of a non-contact NFMM sensitive to variations in the electromagnetic properties of the materials as well as the understanding of the interaction of the microscope with the materials. To accomplish this task, this work also aims to develop non-contact NFMM able to differentiate surface and subsurface conductive and dielectric materials. Other goals include the simulation and creation of lumped-element circuit models of the microscope and sample that can contribute towards understanding the NFMM measurement.

1.3 Contributions

A summary of the contributions of this work is presented below:

1. Development of a DR-based NFMM ($Q=986$) operating at 5.72 GHz able to differentiate several bulk insulating samples ($3.8 < \epsilon'_r < 25$) and liquids ($2.3 < \epsilon'_r < 32$) with a minimum resolvable difference in permittivity of $\Delta\epsilon'_r = 1.78$ and $\Delta\epsilon'_r = 0.04$, respectively. The spatial resolution of the NFMM is 25 μm .

2. Development of a height control mechanism for the DR-based NFMM that employs the resonant frequency and quality factor of the microwave probe for the simultaneous non-contact imaging of topography and conductivity of rough DuPont CB028 thick films used in additive manufactured microwave devices.

3. Non-contact measurement of electrical resistance of additive manufactured resistors using the DR-based NFMM. The relative percent difference in electrical resistance obtained between NFMM and four-point probe measurements is 14.7%. Advantages of the NFMM measurement are that it is non-destructive and no contact pads are required.

4. Development of a coaxial resonator transmission line-based NFMM able to operate in non-contact mode using a quartz tuning fork-based distance following feedback system integrated with the microwave probe. The NFMM is able to differentiate several insulating bulk materials ($3.8 < \epsilon'_r < 25$) even if they are coated with an insulating layer whose thickness is on the order of the tip apex size.

5. Study of the influence of the presence of the quartz tuning fork-based distance following feedback system on the performance of the coaxial resonator transmission line-based NFMM.

6. Study of the influence of the presence of the coaxial resonator transmission line-based NFMM on the performance of the quartz tuning fork-based distance following feedback system.

7. Development of lumped-element circuit models of the DR-based microwave probe and coaxial resonator transmission line-based probe which contributes towards the understanding of the behavior of the NFMM in presence or absence of samples.

8. Non-contact subsurface characterization of PDMS-Ba_{0.55}Sr_{0.45}TiO₃ 49% flexible polymer-composite which is coated with a 10 μm thick parylene-C layer using the coaxial resonator transmission line-based NFMM.

1.4 Dissertation Organization

This dissertation is organized into six chapters, including this Chapter 1. Chapter 2 presents a background review about NFMM and evanescent waves as well as literature review on the application of NFMM for the study and imaging of bulk materials, thin films, liquids, and subsurface features. Chapter 3 discusses the design, simulation and modeling of a DR-based NFMM. Additionally a height control system of the NFMM that uses the measurement of the resonant frequency of the DR-based microwave probe is discussed. Chapter 4 presents the design, simulation and modeling of a coaxial resonator transmission line-based NFMM. Details about the coupling between the probe tip of the microscope and the quartz tuning fork-based distance following feedback system and included in the chapter. Chapter 5 examines the materials differentiation and imaging capabilities of the designed NFMM using bulk insulating materials, liquids and GaAs MMIC circuits. Chapter 6 presents the characterization of printed materials and devices using the DR-based NFMM and the characterization of polymer-ceramic PDMS-PDMS-Ba_{0.55}Sr_{0.45}TiO₃ 49% coated with a 10 µm thick parylene-C layer using the coaxial resonator transmission line-based NFMM.

CHAPTER 2 : LITERATURE REVIEW AND BACKGROUND

2.1 Introduction

The main objective of this chapter is to provide the reader with the necessary concepts and theory required facilitate the understanding about NFMM and its application in materials characterization. In the first section, explanation of the main components and operation of the NFMM is discussed. Subsequently, definition and theory of evanescent waves as well as its influence on the sub-wavelength spatial resolution achieved by NFMM is presented. Afterwards, a summary of the spatial resolution that has been achieved with several NFMM designs is discussed. Additionally, a brief review of the use of several NFMM for qualitative and quantitative characterization of a wide range of materials including, bulk dielectrics, thin films, and NaCl solution is also presented. Cavity perturbation theory and tip-sample interaction models play a key role in quantitative characterization of materials and are discussed in this chapter as well. Finally, equations used to calculate the quality factor of the resonant microwave probes from measured S-parameters are discussed.

2.2 Near-Field Microwave Microscopy

Near-field microwave microscopy is a non-destructive technique used to measure the electromagnetic properties of materials on length scales shorter than the wavelength at the operation frequency [6]. The near-field term refers to the type of field interaction between the sensing probe of the microscope and the material under test (MUT). The basic components of an NFMM are the microwave source, the sensing probe and the detection system. An illustration of an NFMM is shown in Figure 2-1.

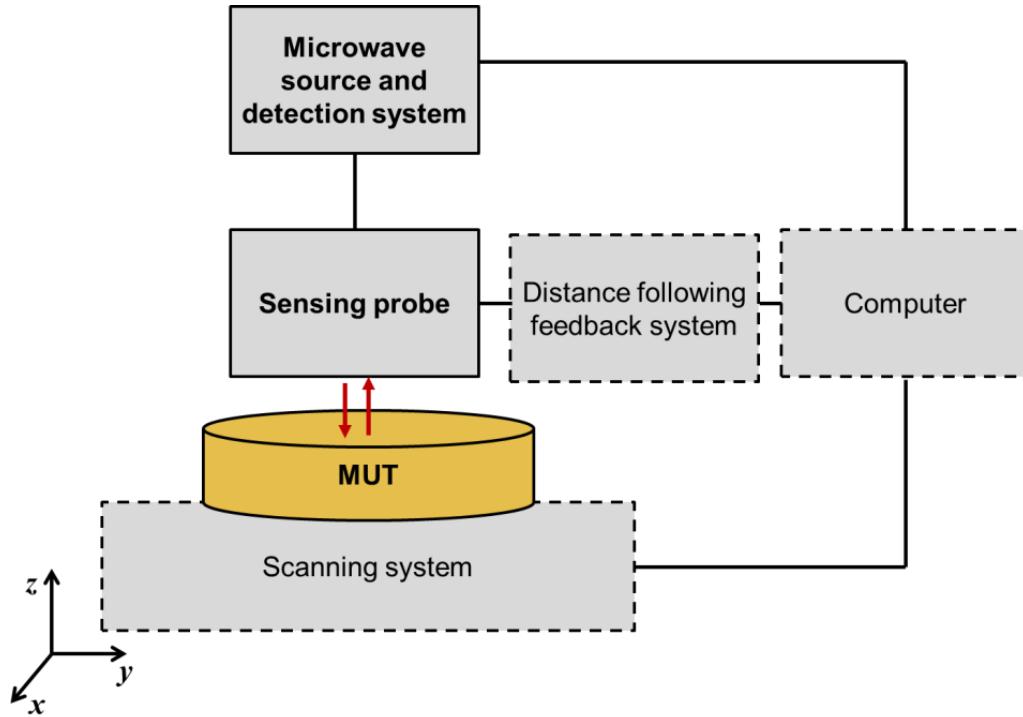


Figure 2-1 Illustration of an NFMM.

A vector network analyzer (VNA) is usually employed as the microwave source and detection system. The sensing probe is the basic NFMM component that directly interacts with the MUT to be examined. The sensing probe can be kept in contact or at some small distance from the MUT, typically less than one-tenth of probe tip size (D) in order for the probe to be sensitive to the sample [6]. To accomplish this task, a distance-following feedback system and a computerized scanning system are integrated to the NFMM. The scanning system is used to move the sample under the sensing probe following a rectangular grid pattern to create an image of the electromagnetic properties over the surface. If a distance-following feedback system is used, both the electromagnetic properties and topography images can be obtained. A scanning system typically employs a combination of stages with coarse and fine resolution motion along the xyz axis in the order of micrometers and nanometers, respectively. Typical distance-following mechanisms are optical beam-bounce based feedback [30], tunneling current-based feedback [31, 32] or quartz tuning-fork-based feedback [33, 34].

The sensing probe can be resonant or non-resonant, the former being more sensitive to detect small changes of the electromagnetic properties of the sample than the latter [35]. As depicted in Figure 2-2, resonant sensing probes consist of a resonator terminated in a sensitive detection element such as an aperture [36] or a sharpened conductive tip [16, 19, 31], whose size D is much smaller than the wavelength at the operating frequency ($D \ll \lambda$). The fields at the end of the conductive tip are evanescent and they store electric or magnetic energy in the near-field of the tip, rather than carrying energy as traveling waves do in the far-field. Thus, evanescent waves are responsible for the high-resolution imaging capabilities of an NFMM since these waves are frequency-independent and are concentrated in a small region ($\approx D$). However, these fields decay exponentially with distance, on a length scale on the order of D , requiring the MUT to be placed in close proximity to the tip, at a distance d usually less than D in order for the resonant probe to be sensitive to the MUT's electromagnetic properties. In order to provide an understanding the evanescent nature of waves, derivation of solutions to the wave equation is presented in the next section.

When the MUT is brought close to the probe tip, the charges on the tip are redistributed and the reactive fields around the tip are perturbed; this field perturbation is translated into changes in the resonant frequency F_r and quality factor Q of the resonator. Changes in the resonant properties of the probe can be correlated with the material properties using semi-empirical methods and/or theoretical models based on resonant perturbation theory. Semi-empirical methods employ calibration samples with known electromagnetic properties to establish a calibration data set. The electromagnetic property of an unknown sample can then be obtained through interpolation. This method has been successfully employed in [12, 37, 38]. A summary of the theoretical models used for correlating the measured F_r and Q , with the electromagnetic properties of the MUT is presented in section 2.6. Drawbacks of the theoretical approach are that the models used rely on approximations of the tip shape to simple geometrical shapes such as spheres, and that the geometry of the tip and the tip-sample distance must be known [6].

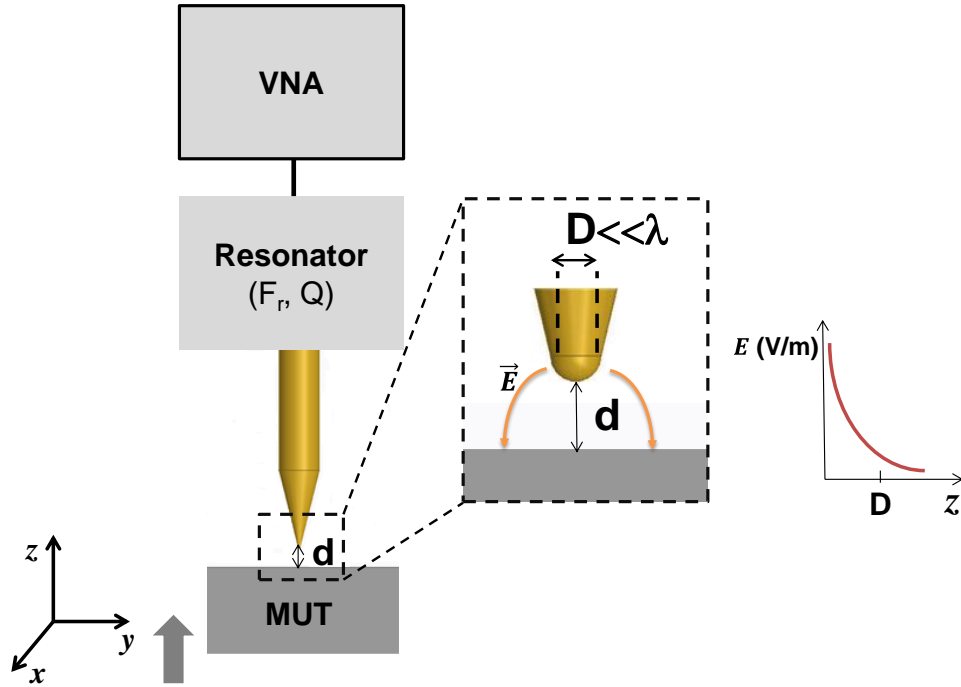


Figure 2-2 Illustration of a resonant microwave probe when an MUT is placed at a distance d from the tip. The inset shows the tip-sample interaction. The fields at the end of the probe tip are evanescent and decay exponentially in the space.

NFMM complements other scanning probe microscopy techniques such as AFM and near-field optical microscopy (NFOM), in that the characterization of the samples can be performed at the surface as well as in the subsurface of the material. Additionally, NFMM operates in a frequency region (DC-THz) not covered by other techniques, as shown in Table 2-1. Compared to AFM, scanning electron microscopy (SEM) and scanning tunneling microscopy (STM), NFMM is able to not only provide topography of the sample, but also the material properties. Other advantages of NFMM over other techniques include not having material limitation as well as not requiring vacuum to operate. Table 2-1 gives a comparison of some commonly used scanning probe microscopy techniques in terms of sample requirements, frequency range, vacuum requirement, and information acquired and image subsurface capability.

Table 2-1. Comparison of some scanning probe microscopy techniques used for materials characterization

Scanning Probe Microscopy	Materials studied	Destructive technique	Vacuum Required	Frequency range	Information acquired	Image subsurface features
AFM	<i>Solids and liquids</i> * Conductor * Insulator * Semiconductor * Biological	No (Non-contact operation)	No	-	* Topography	No
SEM	<i>Solids</i> * Conductor * Surface preparation is required for insulating samples	Yes	Yes	-	* Topography	No
STM	<i>Solids</i> * Conductors * Semiconductor	No	Yes (for fine resolution)	DC	* Topography * Density of states	No
NFOM	<i>Solids</i> * Conductor * Insulator * Semiconductor	No	No	300 THz-750 THz [39]	* Optical information (index of refraction) * Topography	No
NFMM	<i>Solids and liquids</i> * Conductor * Insulator * Semiconductor * Biological	No (Non-contact operation)	No	0.1GHz-140 GHz [39]	* Topography * Permittivity * Conductivity * Permeability	Yes

2.3 Evanescent Fields

Evanescent waves formed at the end of a conductive probe tip of a NFMM whose size is much smaller than λ (small antenna) are also called reactive or non-propagating waves and contribute to the total field in the near-field. These waves are formed as a result of scattering of electromagnetic radiation in fiber optics in a sub-wavelength aperture in a waveguide, in a fiber optic under total internal reflection condition, in the near-field of an antenna and at the end of the NFMM probe tip [6]. Evanescent waves and traveling waves are solutions of the wave equations given by (assuming time-harmonic fields $e^{j\omega t}$ and source-free and lossless media) [40]

$$\nabla^2 \mathbf{E} + k^2 \mathbf{E} = 0 \quad (1)$$

$$\nabla^2 \mathbf{H} + k^2 \mathbf{H} = 0 \quad (2)$$

where, \mathbf{E} , \mathbf{H} and k are the electric and magnetic field, and wave number respectively. The wave number is often called also phase constant and it is given as

$$k = w\sqrt{\epsilon\mu} \quad (3)$$

Solutions to the wave equations can be found using separation of variables method. In a rectangular coordinate system the solution for \mathbf{E} can be considered as

$$\mathbf{E}(x, y, z) = f_x(x)f_y(y)f_z(z) \quad (4)$$

Replacing (4) into (1), three differential equations are obtained

$$\frac{d^2}{dx^2} f_x(x) + k_x^2 f(x) = 0 \quad (5)$$

$$\frac{d^2}{dy^2} f_y(y) + k_y^2 f(y) = 0 \quad (6)$$

$$\frac{d^2}{dz^2} f_z(z) + k_z^2 f(z) = 0 \quad (7)$$

where, the wave number is expressed in terms of k_x , k_y and k_z as

$$k^2 = k_x^2 + k_y^2 + k_z^2 \quad (8)$$

Solutions to (5), (6) and (7) can take different forms (cosines, sines, real or complex exponentials) depending on the boundary conditions. In general, the solutions can be expressed in terms of complex exponentials as

$$f_x(x) = \mathbf{E}_x e^{-jk_x x} \quad (9)$$

$$f_y(y) = \mathbf{E}_y e^{-jk_y y} \quad (10)$$

$$f_z(z) = \mathbf{E}_z e^{-jk_z z} \quad (11)$$

Combining (9), (10) and (11) into (4)

$$\mathbf{E}(x, y, z) = \mathbf{E}_0 e^{-j(k_x x + k_y y + k_z z)} \quad (12)$$

where, $\mathbf{E}_0 = \mathbf{E}_x \mathbf{E}_y \mathbf{E}_z$ is the E-field amplitude. In order to incorporate k into the E-field solution, k_z is expressed in terms of k_x, k_y and k as

$$\mathbf{E}(x, y, z) = \mathbf{E}_0 e^{-j(k_x x + k_y y)} e^{\pm j \sqrt{k^2 - (k_x^2 + k_y^2)} z} \quad (13)$$

This E-field solution (13) represents a traveling or an evanescent wave depending on the relationship between the terms k^2 and $k_x^2 + k_y^2$. If $k^2 > k_x^2 + k_y^2$, the solution is that of traveling waves,

whereas for $k^2 < k_x^2 - k_y^2$, the solution represents an evanescent wave. If phase propagation is assumed in the $+\hat{x}$ direction, the E-field solutions for traveling and evanescent waves are given by

$$\mathbf{E}(x, z) = \mathbf{E}_0 e^{-jk_x x} e^{-j\sqrt{k^2 - k_x^2} z} \quad (14)$$

$$\mathbf{E}(x, z) = \mathbf{E}_0 e^{-jk_x x} e^{-\sqrt{k^2 - k_x^2} z} \quad (15)$$

Equation (14) represents a traveling wave propagating along the $x - z$ plane, for which the amplitude of the field distribution on the wavefront is constant as illustrated in Figure 2-3 (a). On the contrary, (15) represents an evanescent wave oscillating along $+\hat{x}$ whose field distribution is not constant on the wavefront, but it decays along $+\hat{z}$ as shown in Figure 2-3 (b). In other words, an evanescent wave propagates in one direction and decays in another [41] and this decay occurs in a length scale that is much shorter than λ .

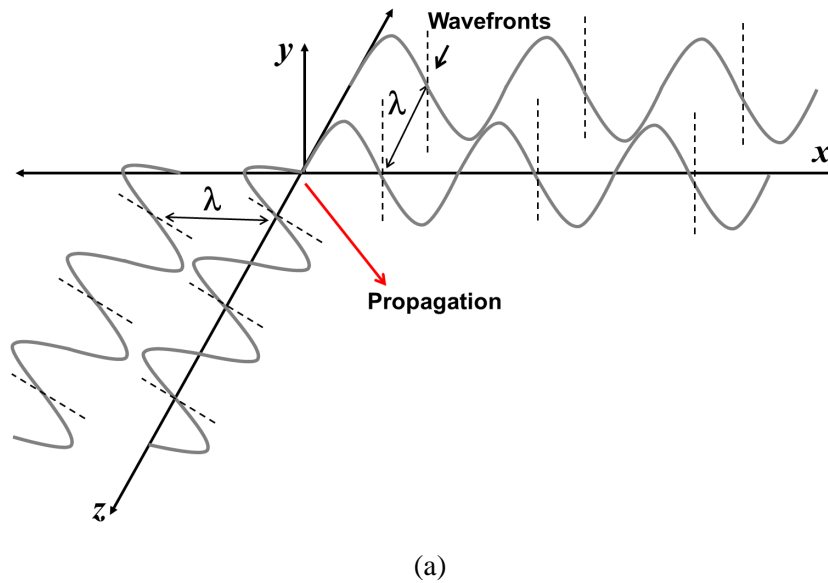
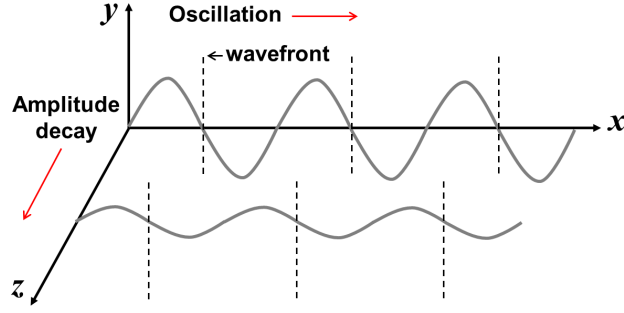


Figure 2-3 Illustration of the (a) traveling wave described by (14) and (b) evanescent wave described by (15).



(b)
Figure 2-3 (Continued)

2.4 Spatial Resolution of a Near-Field Microwave Microscope

Lateral spatial resolution in microscopy refers to the minimum distance between two points at which they can be distinguished as two points. A similar definition applies to NFMM, in which spatial resolution is considered as the smallest feature that the sensing probe is able to successfully resolve. Typically, it is verified by scanning a set of patterns with known lateral dimensions using a scanning step size smaller than the smallest features. Spatial resolution in NFMM contrary to far-field microscopes, such as optical microscopes and SEM, is not restricted by the diffraction limit of $\lambda/2$ established by Ernst Karl Abbe [42] because the fields that interact between the sample and the MUT in an NFMM are evanescent. These evanescent fields are responsible for the image construction in the near-field of the probe tip (source). Since the evanescent fields, not the traveling waves, are the responsible for the image formation, the spatial resolution of a NFMM is determined by the probe-tip geometry rather than the wavelength of the signal employed. Spatial resolution achieved by NFMM in early 1990s was in the order of $600\ \mu\text{m}$ ($\lambda_g/1000$ at 1 GHz) using a $\lambda/4$ microstrip line resonator terminated in a wire with radius of $50\ \mu\text{m}$ [43]. Significant improvement in the probe tip design over the last years has resulted in spatial resolution on the order of $50\ \text{nm}$ ($\lambda/2\text{e}6$ at 2.8 GHz). Table 2-2 summarizes the spatial resolution achieved by several NFMM.

Table 2-2. Summary of lateral spatial resolution achieved by several NFMM

Probe	Resolution	Year
$\lambda/4$ microstrip line resonator terminated in a wire with diameter of 100 μm [43].	$\lambda/1000$ (600 μm) at 1 GHz	1993
Coaxial transmission line terminated in tip with radius of 100 μm tip [92].	$\lambda/300$ (100 μm) at 10 GHz	1996
Stripline resonator terminated in a tip with radius of 2 μm [47].	$\lambda/750000$ (0.5 μm) at 1 GHz	1999
AFM-compatible coaxial probe with an apex radius of 5 nm [39].	$\lambda/2\text{e}6$ (50nm) at 2.8 GHz	2004

Improvement in the lateral spatial resolution of a microwave probe through the reduction of the tip size is accompanied by a degradation of the sensitivity of the probe. The influence of the tip size on the spatial resolution and sensitivity can also be understood through the E-field plots of the tip-sample interaction shown in Figure 2-4. The substrate is a SiO_2 bulk sample ($\epsilon'_r = 4$) and the tip-sample distance in all plots is 0.1 μm . The tip radius is varied from 1 μm to 30 μm . It is evident that the extension of the fields in the sample is deeper and wider for the tip with radius of 30 μm . However, better resolution can be obtained with the tip radius of 1 μm , as the fields are more confined. These observations are in agreement with previous works [31], where a commercially available STM uses several tips with different apex radius to examine the imaging capabilities of a hybrid NFMM-STM system.

In the next section, an overview of the study of materials with sub-wavelength resolution in the microwave frequency regime is presented. This includes the differentiation between materials with different electromagnetic properties and the mapping of these properties of solids and liquids.

Additionally, current results concerning sub-surface imaging of metallic and dielectric features using several NFMM is also presented.

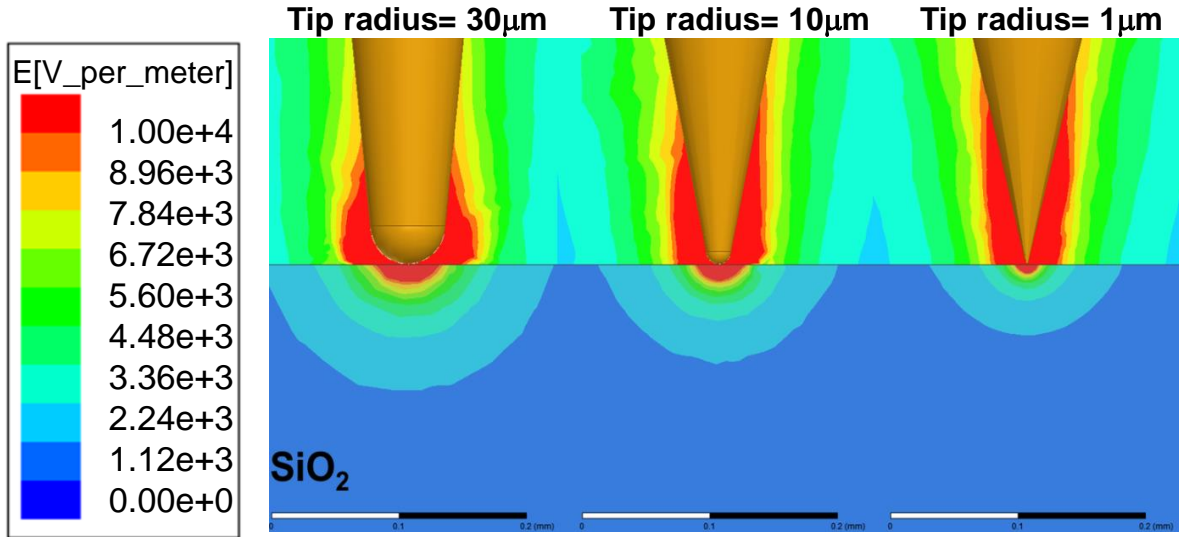


Figure 2-4 E-field plots of the tip-sample interaction for different tip radius. The extension of the fields in the sample is deeper and wider for the tip for a radius of 30 μm . However, better resolution can be obtained with the tip radius of 1 μm . Plots were obtained using Ansys Maxwell V.16.

2.5 Characterization of Materials Using Near-Field Microwave Microscopy

NFMM is a relatively new technique for characterization of materials compared to other widely used scanning probe microscopy techniques such as STM and AFM; the former was invented in 1982 and the latter in the late 1980's. Despite the novelty of NFMM, initial works on NFMM date back to the 1970's, when Ash and Nichols achieved sub-wavelength resolution (0.5 μm at 10 GHz) using an aperture-based microwave probe [36]. However, it was not until the development of STM and AFM that advances in other scanning probe microscopy techniques took place. Since the first works, many groups have contributed to the development and usage of NFMM for materials characterization. Recently, hybrid STM-NFMM and AFM-NFMM have been proposed [39], [31], [32], [44]. These combinations are powerful but also challenging since they require the sample to have a smooth and very clean surface, and for the STM-NFMM combination, the sample must be conductive and kept under very high vacuum.

Furthermore, two limitations of the AFM-based NFMM are that the vertical travel of the probe is dictated by the z -travel of the AFM head (which can be only a few micrometers) and the depth of study is limited to only about 500 nm since the probes use cantilevers whose tip size is about 100 nm [45].

In NFMM, characterization of materials can be qualitative or quantitative. Qualitative characterization contributes to materials differentiation and contrast. Typical 1D or 2D qualitative plots show the resonant properties of the sensing probe for different materials. On the contrary, quantitative characterization provides 1D or 2D plots of the measured electromagnetic property of the sample as a function of distance. In this section, a summary of previous works on qualitative and quantitative characterization of the surface and subsurface of materials using NFMM is presented.

2.5.1 Surface Characterization of Solids and Liquids

- Characterization of Solids

Although there are works about the characterization of materials using cavity perturbation approach in the UHF and microwave frequency regimes [46], it was not until 1993 that a microstrip line resonator-based NFMM operating at 0.8 GHz was presented as a suitable tool for high resolution imaging ($\lambda/1000$) of semi-conductive and conductive features [43]. The microstrip resonator is $\lambda/4$ long and it is tapered at one end to which a 0.1 mm wire is connected. Following works have improved the spatial resolution of the probes by reducing the tip size, and extended the use of NFMM for localized characterization of dielectric, magnetic bulk materials, and thin films. In [47], a microstrip line resonator based-NFMM operating at 1 GHz similar to that presented in [43], was proved to be useful for imaging defects on dielectrics, semiconductors, metals and magnetic bulk samples with spatial resolution of ($\lambda/750000$). Images showed contrast between lower/ higher permittivity regions over a carbon composite sample and lower/higher permeability regions over as section of a hard drive disk [47]. The NFMM was also successfully used to measure the width and depth of grooves in a copper plate. Figure 2-5 shows the

microstrip line resonator-based probe and the map of magnetic domains of a hard drive disk obtained with NFMM. The planar-based resonant probes presented have demonstrated that they are useful for the differentiation of several bulk materials; however, they have poor Q ($Q \approx 100$) which limits the sensitivity of the NFMM.

NFMM also has proven to be a powerful technique for localized characterization of polycrystalline ceramics such as polycrystalline yttria-stabilized zirconia (YSZ) [48], and ceramic composites such as $\text{CaTiO}_3\text{-MgTiO}_3\text{-MgTiO}_4$ [49] and $\text{BaTiO}_3\text{-CoFe}_2\text{O}_4$ [50]. In these works, images of the resonant properties of a commercial cavity coaxial resonator ($Q \approx 1000$) based-NFMM operating at 2.6 GHz in contact with the polished ceramic samples were acquired. F_r images in agreement with X-ray diffraction and energy-dispersive X-ray spectroscopy analysis revealed the distribution of different phases; and therefore different permittivity across the samples.

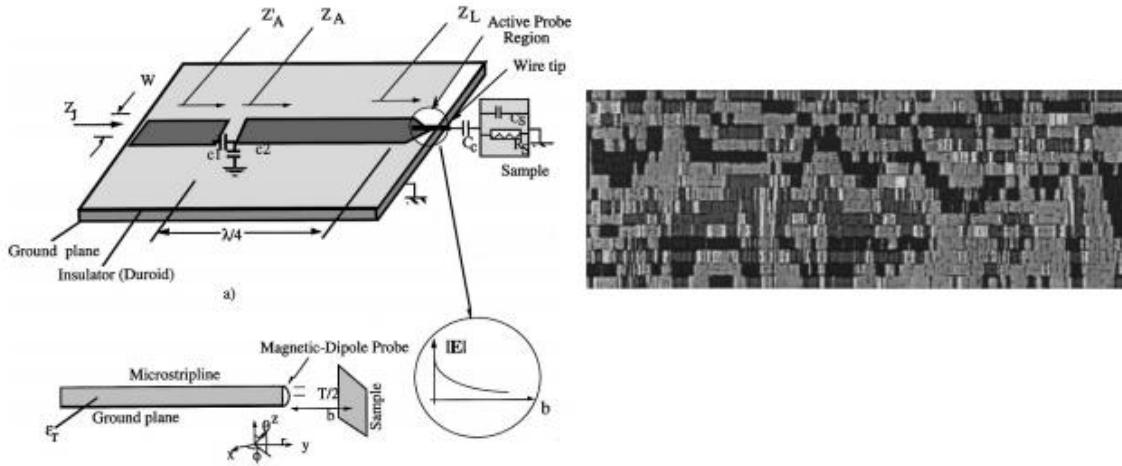


Figure 2-5 Microstrip line resonator probe (left) and NFMM image of a hard drive disk showing regions with higher permeability (darker regions) (right) from [47] © 1999.

Quantitative characterization of bulk dielectrics using NFMM is possible through calibration of the microwave probe using samples with known properties or through the use of cavity perturbation theory and analytical models of the electric field distribution around the tip and sample. In [51], a stripline resonator-based probe terminated in an etched stainless steel tip with diameter of $2 \mu\text{m}$ and resonating at 1

GHz was used for non-contact imaging of the dielectric constant of different smooth bulk samples ($3.6 < \epsilon'_r < 11.8$). The extraction of the dielectric constant was carried out by calibrating the NFMM using known samples. Calibration was also used in [52], for relating the measured shift in F_r of a coaxial transmission line resonator-based probe (9.08 GHz) to dielectric constant for a LaAlO_3 sample. A theoretical approach based on cavity perturbation theory and the method of images was proposed in [7], for measuring the dielectric constant of a wide variety of bulk insulating samples (YSZ, LaGaO_3 , CaNdAlO_4 , TiO_2 , BaTiO_3 , YAlO_3 , SrLaAlO_4 , LaAlO_3 , MgO and LiNbO_3) using the cavity coaxial resonator-based NFMM that operates at 1 GHz shown in Figure 2-6. The unloaded quality factor is 1700. The method of images was used for determining the electric field distribution around the tip and the insulating sample for in-contact and non-contact operation. The cavity perturbation method relates the electric field distribution around the tip and sample with the measured shift in the resonant properties of the resonator.

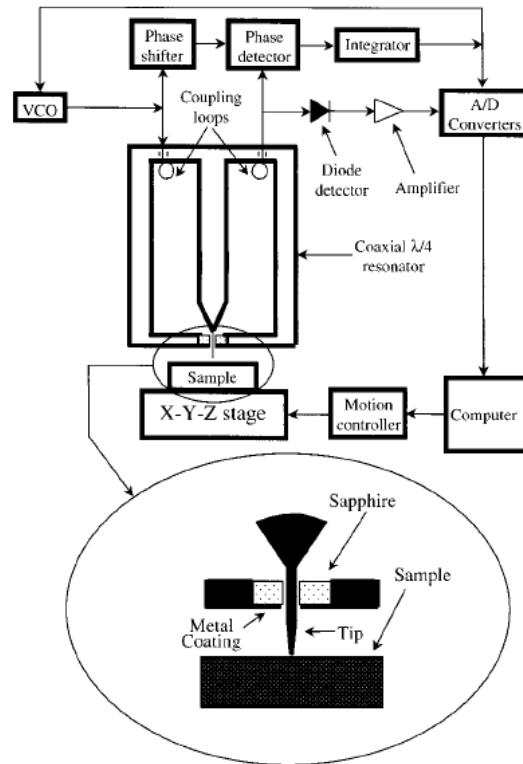


Figure 2-6 Cavity coaxial resonator-based NFMM from [7] © 1998.

Characterization of semiconductors has been mostly conducted in contact mode using a broadband commercial AFM-based NFMM (1-20 GHz) able to simultaneously image surface topography, and amplitude and phase of S_{11} [53]. From measured S_{11} at different bias conditions and by calibrating the NFMM using specially designed calibration standards, sample parameters such as doping concentration and capacitance can be obtained [30, 54-56]. Limitations of the commercial AFM-based NFMM are that it operates in contact mode and that its use for the study of photovoltaics may be limited since the samples are illuminated by the laser-beam bounce system found in the height control system. In order to circumvent these limitations, a coaxial resonator transmission line-based NFMM operating at 2.3 GHz in conjunction with a commercial quartz tuning fork-based height control system has been presented in [33]. This NFMM system allowed the simultaneous imaging of topography, S_{11} amplitude and DC current of a Cu (In, Ga) Se₂ sample under dark and illumination conditions.

NFMM has been extensively used for characterization of conductive [9-11, 16], dielectric [12-14, 44, 57], ferroelectric [15, 18, 19, 58] and anti-ferromagnetic [59] thin films. Quantitative measurement of low- k thin films with permittivity ranging between 2 and 3.5 has been carried out using a $\lambda/2$ parallel strip resonator terminated in a tip size of 3 μm [12]. The measured changes in F_r were correlated with the permittivity through calibration using only two standard samples (a metal and air). This was possible because they found that at certain tip-sample distance, the relation between ΔF_r and $\beta = (k-1)/(k+1)$ becomes linear. Limitation of this approach is that the measurements can be done only at certain tip-sample distance, which is not necessarily the best one to achieve good sensitivity or resolution. Quantitative characterization of conductive thin films has consisted of the measurement of the reflection coefficient and resonant properties of the probe as a function of the sheet resistance of thin films with different conductivities [9] or variable-thickness thin films [16]. Imaging of sheet resistance of an YBa₂Cu₃O_{7- δ} thin film on a sapphire wafer was carried out by monitoring the unloaded Q of the coaxial transmission line-based resonator shown in Figure 2-7 (left). In order to correlate the measured Q to sheet resistance, the microscope was calibrated using aluminum thin films with different thickness as presented

in Figure 2-7 (right). A dielectric resonator-based NFMM ($Q=11840$) has also been used to differentiate aluminum thin films with different thickness through S_{11} versus frequency measurements; however, imaging of sheet resistance or resistivity was not presented. Quantitative measurement of permittivity of ferroelectric thin films such as BaSrTiO_3 , $\text{BaTiO}_3\text{-CoFe}_2\text{O}_4$ and BiFeO_3 thin films is reported in [19], [60]. Permittivity and tunability images of 370 nm thick $\text{Ba}_{0.6}\text{Sr}_{0.4}\text{TiO}_3$ (BST) thin films obtained with an NFMM operating in contact with the sample is presented in [15]. The NFMM employs the open-ended coaxial probe terminated in a sharp tip of 1 μm radius. Measured ΔF_r and Q were correlated with the permittivity using calibration standards with known properties and resonant perturbation theory. The dc voltage required to measure tunability was applied between the probe tip and a grounded $\text{La}_{0.5}\text{Sr}_{0.5}\text{CoO}_3$ counter electrode deposited beneath the BST film.

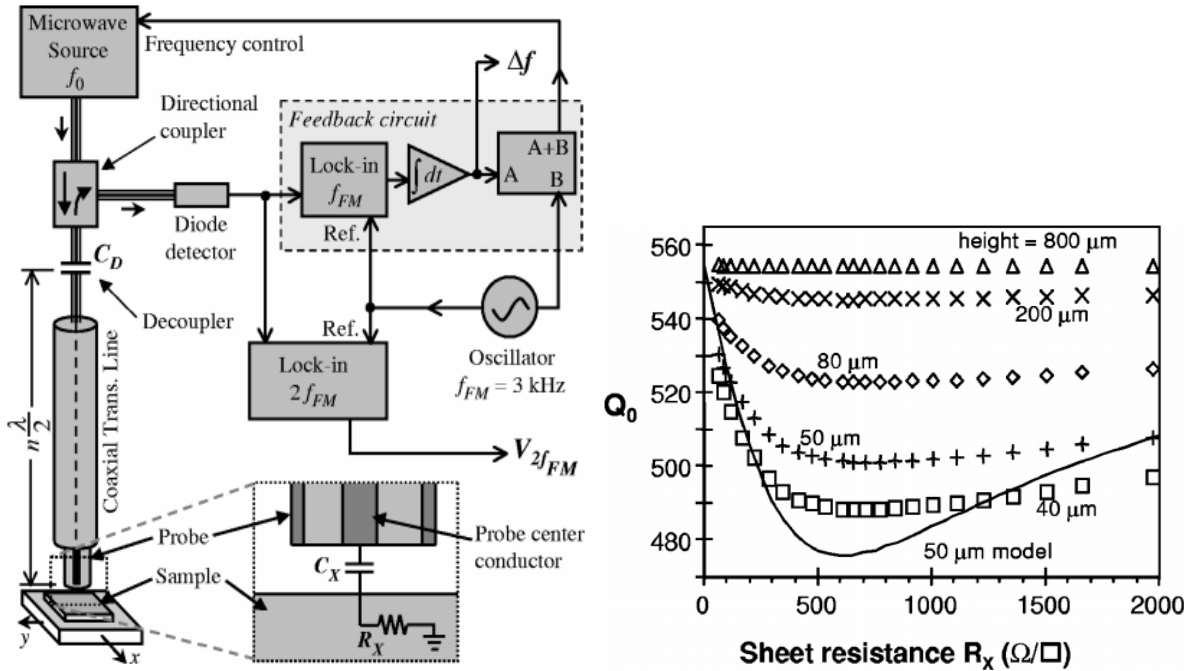


Figure 2-7 Coaxial transmission line-based NFMM (left) and Q versus sheet resistance of a variable-thickness aluminum thin film (right) from [16] © 1998.

- Characterization of liquids

NFMM has been mainly used for characterization of lossy liquids such as NaCl [61, 62]. In [62], the resonant properties of a $\lambda/4$ resonant coaxial probe were investigated in non-contact operation for water and different NaCl solutions. In order to avoid any contact between the tip and the liquid a 6 μm -thick Mylar layer covered the solution. It was found that the coaxial resonator based-NFMM was able to detect variations in NaCl concentration ranging from 0% to 30% in de-ionized water by studying the changes in F_r and Q . Capabilities of a coaxial resonator transmission line-based NFMM to sense NaCl concentration in an aqueous solution (0-0.25 mol/l) have been demonstrated in [61]. Compared to the previous work, the sensitivity of the NFMM to detect variations in NaCl concentration in an aqueous solution is determined through the study of the magnitude of the reflection coefficient at a fixed frequency of 2.4 GHz rather than through Q or F_r . Additionally, the measurements were performed under in-situ conditions (tip immersed 100 μm in the liquid), which required the adjustment of an impedance tuner so that the probe is critically coupled to the source when the tip is immersed in the liquid.

In [63], it was demonstrated that a hybrid STM-NFMM is able to image a graphite sample under water for frequencies up to 50 GHz. Although simultaneous mapping of topography and reflection coefficient of the probe was demonstrated and resolution in the order of nanometers was confirmed, no characterization of liquids was carried out.

2.5.2 Sub-surface Characterization of Solids

NFMM has been successfully used to detect the topography of metallic features coated by a conductive layer and insulating layer. Feature identification has been carried out by detecting changes in the output signals of NFMM ($\text{mag}(S_{11})$, $\text{phase}(S_{11})$, voltage) as the NFMM scans over a homogenous, uniform and known film containing the buried features; any detected change in the output reading represents a change in the buried material. In [27], a commercial hybrid AFM-NFMM was used to image

buried Al defects in a 120 nm thick Ni film deposited onto a Si substrate. The probe operated in contact mode and scanned over the testing sample using several operating frequencies ranging from 1 to 6 GHz in order to image features at different depths from 0 nm to 125 nm. Phase images shown in Figure 2-8, reveal that the Al patterns are resolved for an operating frequency of 1.878 GHz.

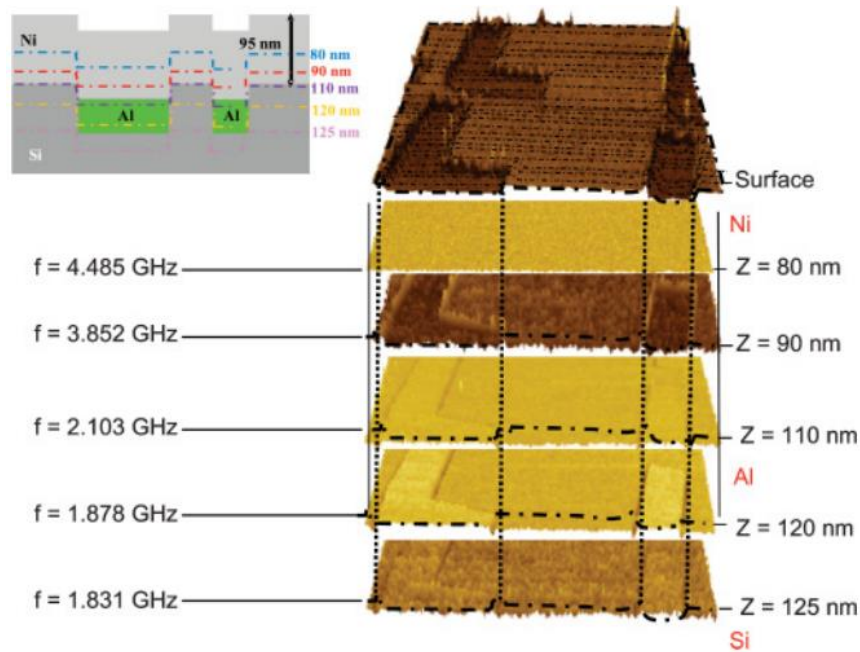


Figure 2-8 Testing sample and measured phase of reflection coefficient image at different operating frequencies from [27] © 2011.

Gold traces buried in an 800 nm thick SiO₂ layer have been imaged before and after 1000 thermal cycles also using a commercial AFM-NFMM operating in contact mode at 7 GHz [29]. Two limitations of the AFM-based NFMM are that the vertical travel of the probe is dictated by the z -travel of the AFM head (which can be only a few micrometers) and the depth of study is limited to only about hundreds of nanometers since the probes use cantilevers whose tip size is about 100 nm. Attempts to solve these limitations include the use of non-AFM probes with larger tip size. In [28], a coaxial resonator-based NFMM operating in non-contact mode at a frequency of 763 MHz is used to image MMIC spiral inductors, pads, and traces embedded at 0.8 μm and 8.6 μm below the surface using probe tips of radius 10 μm and 50 μm . Another approach recently presented to overcome the limited penetration depth is to

operate the commercial AFM-NFMM in transmission mode (TM-NFMM) rather than in reflection mode [45]. For this purpose, an SMA-type-probe acts as a radiating antenna and an AFM cantilever-type tip collects the signal that propagates from the SMA probe through the sample as illustrated in Figure 2-9. Images of surface topography and S_{21} parameters showed that the TM-NFMM is able to distinguish different doping levels along the cross section of a bulk silicon substrate. Disadvantages of this approach include the limitation of samples to be studied and the complex sample positioning setup.

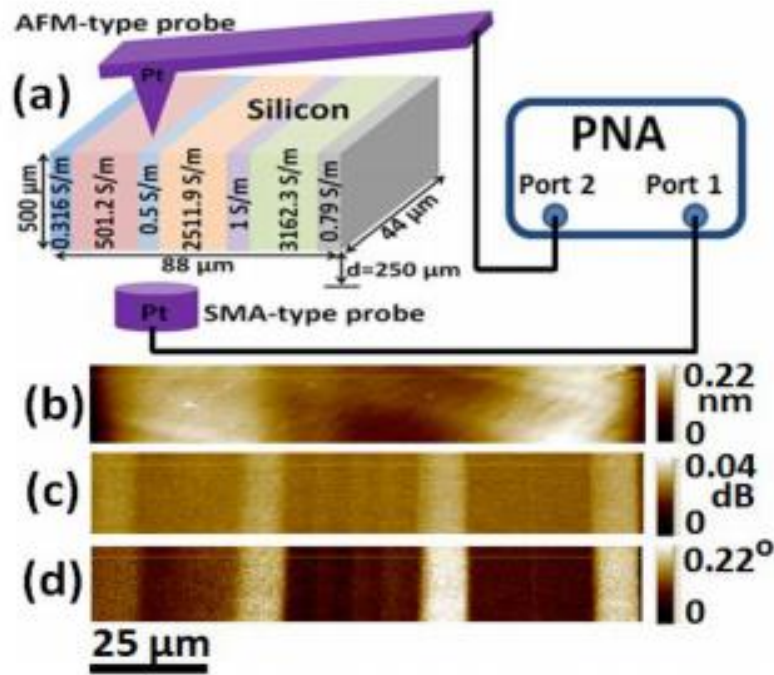


Figure 2-9 Experimental setup of the TM-NFMM and measured topography and S_{21} parameters images of the testing sample (bulk silicon with varying doping profile along the cross-section) from [45] © 2014.

Subsurface dielectric features have also been imaged at 60 GHz using a microstrip line resonator-based NFMM [64]. The imaged feature is a 200 μm wide resin ring pattern buried under 30 μm AZ4562 resin. The microwave probe consisted of a gold microstrip line deposited on an alumina substrate. The probe was tapered to 7 μm and the scanning was performed at a standoff distance of 5 μm. Magnitude and phase-shift images of reflection coefficient showed that the probe was able to resolve the buried ring.

Imaging of subsurface features immersed in a lossy liquid was presented in [65], where a Split-Ring Resonator (SRR) resonating at 1.2 GHz with dimensions of 20 mm x 20 mm is excited by a rectangular loop. This probe was used for detection of an Aluminum cube (3.2 mm x 3.2 mm x 3.2 mm) immersed at different depths (1 mm – 4 mm) in 1% NaCl solution. In this work, it was demonstrated that the SRR increased the evanescent fields around the probe, compared to the single rectangular loop, and that the increase in the fields improves the sensitivity of the probe to detect the aluminum box. Measurements consisted of 1-D scan profiles of phase change of the probe versus Y-distance showing the presence of the Aluminum box when it was immersed from 1 mm to 4 mm.

Before proceeding further with the background review of cavity perturbation theory and the modeling of the tip-sample interaction, a summary of the capabilities, advantages and limitations of several probes used in the NFMM discussed in this section is summarized in Table 2-3. Six criteria are selected for this comparison including vacuum requirements, approximated scan size, materials that can be characterized, probe size, depth of study, and Q. The designs with the highest Q are those that use cavity and DR-based probes; higher Q improves the sensitivity of the NFMM. The main disadvantage of these probes is that they are bulky compared to the other designs which complicates the integration with distance following feedback systems. On the contrary, coaxial-transmission line and planar-based probes are compact but their Q is not high. STM and AFM-based NFMM designs allow imaging of electromagnetic properties with very high resolution since the probe tip size is on the order of nanometers. This advantage may turn into a limitation if subsurface sensing at depths larger than a few hundreds of nanometers is desired. Additionally, these designs are intended to be used to study samples with very smooth surface and particularly for the AFM-based design, the scan area is limited to about 50 μm x 50 μm . Finally, important limitations of the STM-based NFMM design are that it requires vacuum to achieve the very high resolution images and the samples should be conductive.

Table 2-3. Summary of several NFMM probe design capabilities

Probe type	Vacuum	Scan size	Materials	Q	Depth of study	Probe Size
Coaxial transmission line	No	mm x mm	Smooth and rough conductive, dielectric, semiconductor (solids and liquids)	≈ 500	nm- μ m	nm- μ m
DR-based	No	mm x mm	Smooth and rough conductive, dielectric, semiconductor (solids and liquids)	≈ 10000	nm- μ m	nm- μ m
Cavity-coaxial	No	mm x mm	Smooth and rough conductive, dielectric, semiconductor (solids and liquids)	≈ 1500	nm- μ m	nm- μ m
Planar (microstrip, stripline)	No	mm x mm	Smooth and rough conductive, dielectric, semiconductor (solids and liquids)	≈ 200	nm- μ m	nm- μ m
STM-based	Yes	μ m x μ m	Smooth conductor (solids)	≈ 500	nm	nm
AFM-based	No	μ m x μ m	Smooth-conductive, dielectric, semiconductor (solids)	-	nm	nm

2.6 Cavity-Perturbation Theory and Modeling of Tip-Sample Interaction

The cavity-perturbation method provides a scheme that allows the correlation between the electromagnetic properties of the MUT and the measured shift in the resonant properties of the microwave probe of the NFMM. In this section, cavity-perturbation theory and particularly, equations for material-perturbation are presented. Study of perturbation of the resonant properties of a cavity under changes in its shape, materials that it is made of, and materials in its surroundings can be used for tuning the resonant frequency of the cavity and for the study of the electromagnetic properties of dielectrics, conductors, superconductors and semiconductors. The cavity perturbation method assumes that the cavity

has perfect conductivity and that the fields in the cavity before and after the perturbation are not significantly different; in other words, the perturbation must be small. There are three types of cavity perturbations: cavity-shape perturbation, material-perturbation, and wall-impedance perturbation [35]. Although cavity-shape perturbation and wall-impedance perturbation can be used for tuning resonance frequency of the cavity and for surface resistance measurement, respectively, in this section, only material-perturbation will be discussed. Material perturbation is widely used for the study of electromagnetic properties of materials and is divided into two cases, whole medium perturbation and small-object perturbation. Whole medium perturbation is typically used for characterization of gases and can be achieved by replacing the material in the region enclosed by the cavity by a different one. This change affects the resonant properties of the cavity and the amount of change can be related to the electromagnetic properties of the new medium. Small-object perturbation assumes that the sample introduced in the cavity is small so that only the electromagnetic properties of the space occupied by the sample are altered but the electromagnetic fields and the storage energy in the cavity do not change after the introduction of the sample.

The basic equation for material perturbation in (18) assumes that at the boundary of the cavity, the electric fields before and after perturbation satisfy (16) and (17) [35]

$$n \times \vec{E}_1^* = 0 \quad (16)$$

$$n \times \vec{E}_2 = 0 \quad (17)$$

$$\frac{\Delta\omega}{\omega_1} = \frac{\omega_2 - \omega_1}{\omega_1} = - \frac{\int_{V_c} \left[(\vec{E}_1^* \cdot \vec{E}_2)(\epsilon_2 - \epsilon_1) + (\vec{H}_1^* \cdot \vec{H}_2)(\mu_2 - \mu_1) \right] dv}{\int_{V_c} \left[(\vec{H}_1^* \cdot \vec{H}_2)\mu_1 + (\vec{E}_1^* \cdot \vec{E}_2)\epsilon_1 \right] dv} \quad (18)$$

where, \vec{E}_1^* , \vec{H}_1^* , ϵ_1, μ_1 , and ω_1 are the electric field, magnetic field, permittivity, permeability of the medium and angular resonant frequency of the unperturbed cavity, respectively. $\vec{E}_2, \vec{H}_2, \epsilon_2, \mu_2$ and ω_2 are the electric field, magnetic field, permittivity, permeability of the medium, and angular resonant frequency of the perturbed cavity, respectively. V_c is the region enclosed by the cavity.

For small-object perturbation ($\vec{E}_1 \approx \vec{E}_2$), (18) can be further expressed as

$$\frac{\Delta\omega}{\omega_1} = \frac{\omega_2 - \omega_1}{\omega_1} = - \frac{\int_{V_c} \left[|\vec{E}_1|^2 (\epsilon_2 - \epsilon_1) + |\vec{H}_1|^2 (\mu_2 - \mu_1) \right] dv}{\int_{V_c} \left[|\vec{H}_1|^2 \mu_1 + |\vec{E}_1|^2 \epsilon_1 \right] dv} \quad (19)$$

The denominator of the right side of (19) represents the stored electric and magnetic energy in the cavity, which remains constant (α) after the introduction of the sample as discussed previously. Thus, (19) can be further approximated by

$$\frac{\Delta\omega}{\omega_1} = \frac{\omega_2 - \omega_1}{\omega_1} = - \frac{\int_{V_c} \left[|\vec{E}_1|^2 (\epsilon_2 - \epsilon_1) + |\vec{H}_1|^2 (\mu_2 - \mu_1) \right] dv}{\alpha} \quad (20)$$

From (19), an increase in the permittivity and/or permeability due to the introduction of the sample will result in a reduction of the resonant frequency of the cavity.

Analytical solutions for the electric field distribution in (19) for the tip interacting in soft contact with a thick insulating sample of permittivity ϵ_2 have been found through method of images [7]. Two assumptions are made; the first one is that the tip can be represented by a conductive sphere of radius R_0 , which is supported by the fact that this region of the tip concentrates the majority of the fields. The sphere has a potential V_0 . The second approximation is that a quasi-static analysis can be conducted since the evanescent fields are confined in a region that is much smaller than the wavelength at the operating

frequency; therefore the propagating nature of the wave can be safely ignored. The electric field in the sample found through method of images and expressed as the superposition of the contribution of point charges is [7]

$$\vec{E}_1 = \frac{q}{2\pi(\varepsilon_0 + \varepsilon)} \sum_{n=1}^{\infty} \frac{1}{n} b^{n-1} \frac{r\vec{e}_r + (z + R_0/n)\vec{e}_z}{[r^2 + (z + R_0/n)^2]^{3/2}} \quad (21)$$

where $b = \frac{\varepsilon_2 - \varepsilon_1}{\varepsilon_2 + \varepsilon_1}$, $q = 4\pi\varepsilon_1 R_0 V_0$, \vec{e}_r and \vec{e}_z are the unit vectors along the direction of the cylindrical coordinates r and z , respectively. Inserting (21) into (20), the shift in the measured resonant properties Δf and ΔQ can be related to the electromagnetic properties of the sample [7]

$$\frac{\Delta f}{f_1} = A \left(\frac{\ln(1-b)}{b} + 1 \right) \quad (22)$$

$$\Delta \left(\frac{1}{Q} \right) = -(B + \tan \delta) \frac{\Delta f}{f_1} \quad (23)$$

where A and B are constants that depend on the tip and resonator and can be determined by calibrating the NFMM using a sample with known permittivity such as MgO or LaAlO₃. Equations similar to (22) and (23) have been presented in [17] for the quantitative characterization of dielectric films in contact and at a height h from the conductive sphere. The method of images can also be used to determine analytical expressions for the electromagnetic fields inside and at the surface of a conductive sample placed at a distance h from the conductive sphere [41]. Integration of the electromagnetic field expressions into the cavity perturbation equations allows the extraction of the surface resistance of the conductive sample.

In addition to the method of images, lumped-element circuit modeling of the resonator and tip-sample interaction have also been proposed as a framework to correlate the measured shift in the resonant

properties of the microwave probe to the sheet resistance of conductive samples. In [41], a coaxial transmission line resonator-based probe is modeled as a parallel RLC resonator with resistance R_0 , capacitance C_0 and inductance L_0 . The coupling between the probe tip and the conductive sample is modeled by the capacitance C_x and the losses of the sample are represented by R_x . The capacitor C_x is connected in series with R_x as illustrated in Figure 2-10.

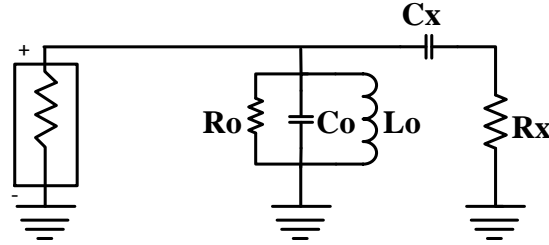


Figure 2-10 Lumped-element circuit model of a parallel RLC resonator interacting with a conductive sample through C_x .

Values for R_0 , C_0 and L_0 depend on the resonator design and the C_x can be found through the method of images, assuming the tip as a conductive sphere of radius R_0 placed at a height h from the infinite plane. C_x is expressed as [66]

$$C_x = 4\pi\epsilon_0 R_0 \sinh \alpha \sum_{n=1}^{\infty} \frac{1}{\sinh(n\alpha)} \quad (24)$$

where $\alpha = \cosh^{-1} \left(1 + \frac{h}{R_0} \right)$. Using Taylor series expansion and using the approximations, C_x can be reduced to [41]

$$C_x = 4\pi\epsilon_0 R_0 \left[\frac{1}{\alpha} \ln \left(\frac{0.693}{2} + \frac{h}{2R_0} \right) \right] \sinh \alpha \quad (25)$$

From (25), it can be clearly seen that the capacitance C_x increases with R_o and degrades if the sample moves away from the tip. Since C_x is the responsible for the tip-sample interaction, a greater C_x implies better sensitivity of the resonant probe to detect small variations in R_x . The relationship between the measured shift in the resonant frequencies and the circuit parameters C_x and R_x is defined under the limit $\omega C_x R_x \ll 1$ as [41]

$$\frac{\Delta f}{f_1} \cong -\frac{C_x}{2C_0} \quad (26)$$

$$\frac{Q_2}{Q_1} \cong 1 - R_0 \omega^2 C_x^2 R_x \quad (27)$$

The presented analytical equations and lumped-element circuit models of the tip-sample interaction along with cavity perturbation theory not only allow the extraction of the electromagnetic properties of the MUT but also contribute to the understanding of the functioning of the NFMM. However, these methods and equations rely on approximated and simplified models of the probe and sample. Models involving more complex tip-sample interactions are extremely challenging and time consuming, and require the use of numerical techniques and software such as Ansys Maxwell or Comsol Multiphysics.

2.7 Resonant Properties and Coupling of a Resonant Probe

The resonant properties F_r and Q are important figures of merit that describe a resonant probe (referred to as resonator in this section). F_r describes the frequency at which the electric and magnetic energy stored in the resonator are equal. Q , also denoted as Q_u (unloaded Q), establishes the relationship between the energy stored W to the average power dissipated in the resonator P_L [35].

$$Q = \frac{\omega W}{P_L} = \frac{\omega W}{P_d + P_c} \quad (28)$$

where P_L includes dielectric (P_d) and conductor (P_c) losses. Near resonance, a resonator can be modeled through series and parallel one-port RLC circuits. As an example, lumped element circuit model of a parallel RCL resonator is illustrated in Figure 2-11 (a). These models although simple are very useful for the understanding of the resonator operation near resonance. Frequency response of a parallel RLC circuit is shown in Figure 2-11 (b).

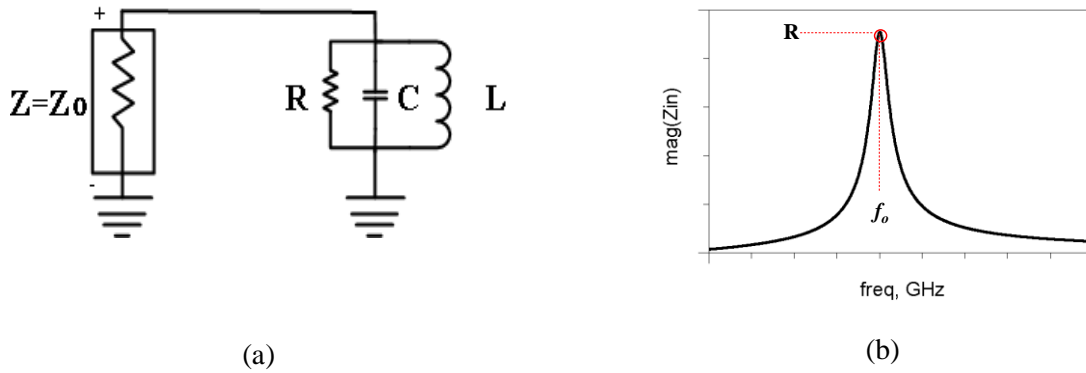


Figure 2-11 (a) Lumped-element circuit model and (b) frequency response of a one-port parallel RLC resonator.

At resonance, the input impedance is real and corresponds to R and $1/R$ for series and parallel resonator, respectively. Furthermore, F_r and Q also can be expressed in terms of RLC components as

Table 2-4. Z_{in} , F_r and Q for series and parallel resonator topologies

Resonator topology	Z_{in}	F_r	Q
Series	R	$\frac{1}{2\pi\sqrt{LC}}$	$\frac{1}{\omega_0 RC}$
Parallel	$1/R$	$\frac{1}{2\pi\sqrt{LC}}$	$\omega_0 RC$

Regardless of the resonator topology, Q can also be expressed in terms of the half-power bandwidth (BW) as

$$Q = \frac{1}{BW} = \frac{f_0}{f_2 - f_1} \quad (29)$$

This Q -BW relationship is very useful to visualize that a high resonator Q will have a narrow bandwidth and therefore higher selectivity. When the resonator is coupled a source, the resonator is not isolated anymore and the quality factor that describes the dissipation in the external circuit is the external quality factor Q_e whereas the loaded resonator is described by the loaded quality factor Q_L . Q , Q_L and Q_e are related through [67]

$$\frac{1}{Q_L} = \frac{1}{Q_e} + \frac{1}{Q} \quad (30)$$

The coupling between the resonator and the source is described by the coupling coefficient β , which equals the ratio between Q and Q_e . This relationship applies to both series and parallel RLC resonators [67].

$$\beta = \frac{Q}{Q_e} \quad (31)$$

Three different coupling cases can be determined from β . For $\beta=1$, the resonator is critically coupled to the source and the energy dissipation in the external source equals that in the resonator. For $\beta>1$, the resonator is over-coupled to source and more energy is dissipated in the external source than in

the resonator. For $\beta < 1$, the resonator is under-coupled to the source and more energy is dissipated in the resonator than in the external source. The difference between these three cases can be visualized through the simulation of a parallel resonator coupled to the source through a series capacitor C_c . The Smith chart in Figure 2-12 shows the S_{11} parameters of a parallel RLC resonator for different values of C_c (0.07 pF, 0.16 pF and 0.3 pF). For critical coupling the input impedance is $Z_{in} = Z_o$, whereas for over-coupling $Z_{in} = 6.4 * Z_o$ and for under-coupling $Z_{in} = 0.3 Z_o$. It is worth noting that although the resonator has a parallel RLC topology, the response is that of a series RLC resonator due to the inverting effect of the C_c capacitor [67].

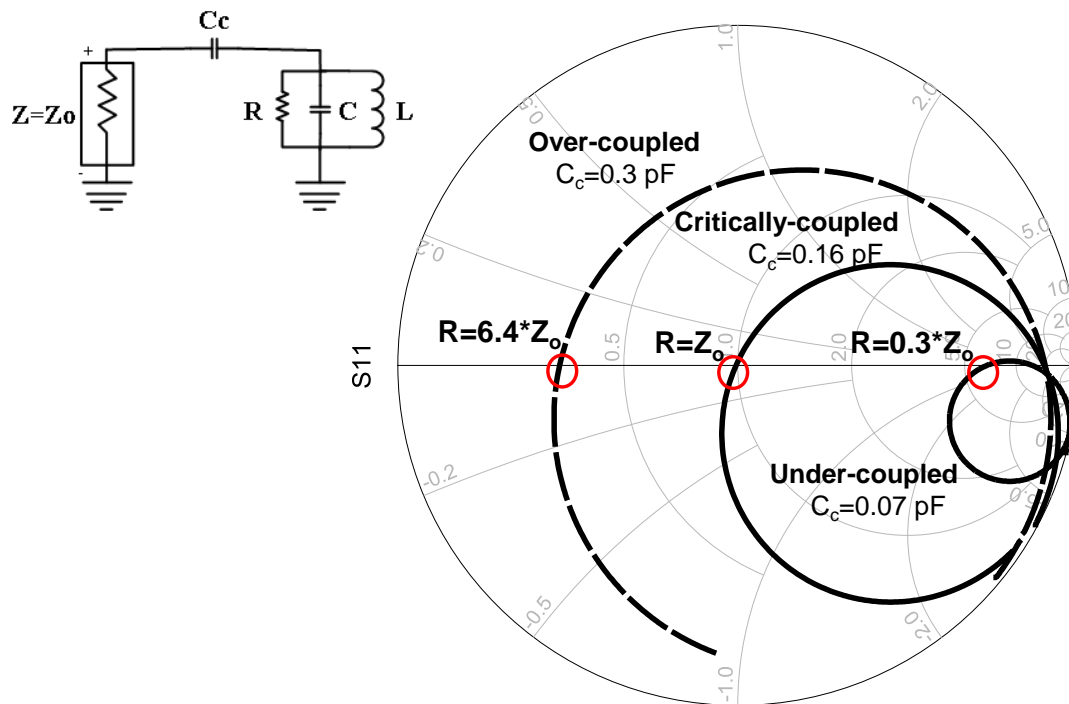


Figure 2-12 Effect of C_c on the coupling of a parallel RLC resonator to a source.

In this work F_r and Q are determined from the measured S-parameters as explained in the next sections. Other techniques employed to determine Q and the comparison between the accuracy of the techniques can be found in [68].

2.7.1 One-Port Resonator

Measured S-parameters are converted to input impedance in order to calculate Q. From $|Z_{in}|$ versus frequency data, f_2 and f_1 are determined at the points where $|Z_{in}| = 0.707R$, where R is the lumped resistance of a parallel resonator as illustrated in Figure 2-13. In this work, the resonator is critically coupled to the source; therefore $\beta=1$, $Q_e=Q$, and $Q_L=Q/2$. Once, f_2 and f_1 are known, (28) is used to calculate Q.

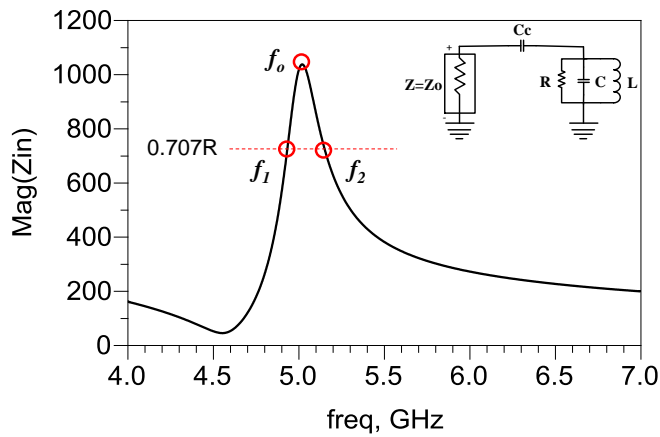


Figure 2-13 Magnitude of input impedance versus frequency for a 1-port RLC parallel resonator coupled to a source through a capacitor $C_c=0.16$ pF.

2.7.2 Two-Port Resonator

For a two-port parallel RLC resonator, the Q factor is also calculated using the measured S-parameters. A typical resonant curve of a two-port parallel RLC resonator is shown in Figure 2-. From this figure parameters necessary to calculate Q, Q_L and Q_e such as f_1 , f_2 , f_3 and f_4 can be obtained. Equations that relate these frequencies to the quality factors are [69]

$$Q = \frac{f_0}{f_3 - f_2} \quad (32)$$

$$Q_L = \frac{f_0}{f_4 - f_1} \quad (33)$$

The parameter x in Figure 2-14 is found through [70]

$$x \text{ (dB)} = 3 - 10 \log(1 + 10^{-0.1L_{ins}}) \quad (34)$$

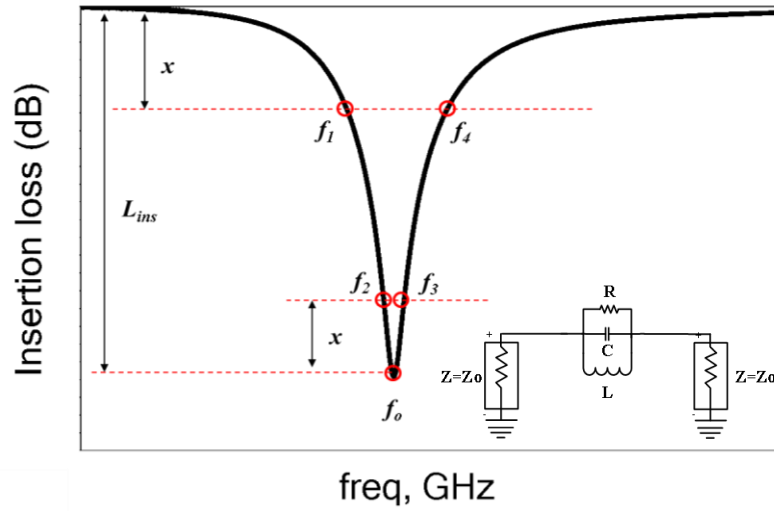


Figure 2-14 Insertion loss versus frequency for a 2-port RLC parallel resonator.

Q_e can be obtained using Q , Q_L and (30).

2.8 Conclusion

In this chapter, a review on the main components of NFMM and its operation, evanescent waves, cavity perturbation theory, and the expressions for the fields and lumped-element models describing the tip-sample interaction is presented. It has been demonstrated that NFMM is a powerful technique that can be used to study smooth bulk materials, lossy liquids, and thin films with sub-wavelength resolution. A

comparison between several microwave probe designs showed the advantages and limitations of each design regarding materials that can be studied, spatial resolution, and vacuum requirements. In the next chapters, two different NFMM designs that use a DR-based microwave probe and a coaxial transmission line-based probe will be presented and used for the measurement of electromagnetic properties of non-conventional materials and structures such as additive manufactured inks and resistors, and flexible ceramic composites.

CHAPTER 3 : DIELECTRIC RESONATOR-BASED MICROWAVE MICROSCOPE

3.1 Introduction

The sensitivity of an NFMM means the ability of the probe to detect small variations in the electromagnetic properties of the MUT, which can be maximized by improving the Q of the resonator used as a probe [71]. Examples of high Q resonators that can be used as probes in a NFMM are cavities and dielectric resonators (DR). DR offer advantages over cavities such as low cost, small size and light weight [35]. One of the first DR-based NFMM designs was presented by Kim *et al.* in 2003 [72]. The microwave probe resonating at 4.5 GHz consisted of a DR enclosed in a cylindrical cavity as illustrated in Figure 3-1. This design showed good sensitivity to Al thin films of thicknesses ranging from 5 nm to 15 nm deposited on a glass substrate. The main drawback of this design is that it does not use any tip-sample distance control system. Similar DR-based NFMM designs were presented by Kim *et al.* in 2003 and 2005 [34, 73]. The improvement in the NFMM design was that a quartz tuning fork-based distance control system was attached to the microwave probe so that simultaneously topography and NFMM images of patterned copper films on a silicon substrate were obtained. In the mentioned works, modeling of the probe and sample is not discussed.

In this chapter, the design, modeling, fabrication and testing of a DR-based microwave probe operating at 5.72 GHz is presented. The resonant probe consists of a DR coupled to a commercially available gold coated tip through a non-resonant microstrip line. Advantages of this design are that the probe exhibits high Q ($Q=986$) and the probe tips can be easily exchanged. The DR-based probe is simulated using a combination of circuit simulation and electromagnetic simulation. Circuit simulation is used for simulating the lumped-element circuit model of the microwave probe and HFSS is used for the simulation of the tip-sample interaction. To the best of the author's knowledge, this is the first time that a

lumped-element circuit model of a DR-based microwave probe is presented. Lumped-element circuit models of microwave probes are of significant importance in NFMM because they contribute with the understanding of the behavior of the microscope in presence or absence of the MUT. For instance, influence of design parameters such as coupling of the resonant probe to the source and Q of the probe on the microscope response can be initially investigated and optimized without requiring time consuming electromagnetic simulations.

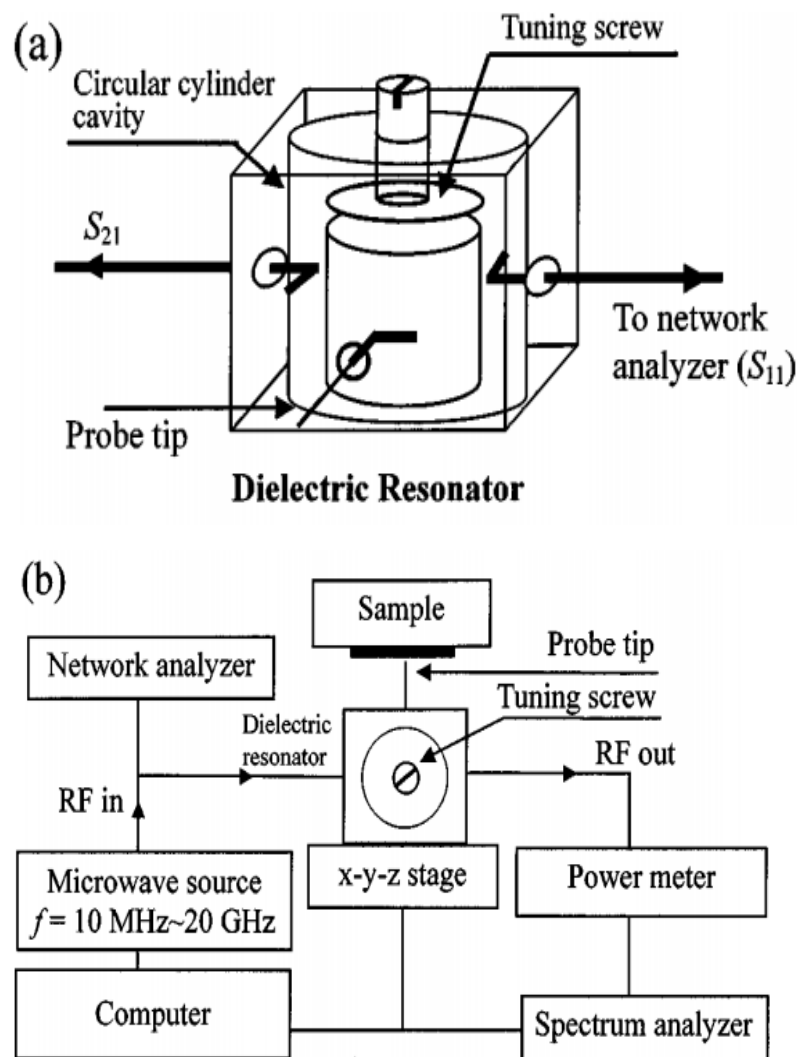
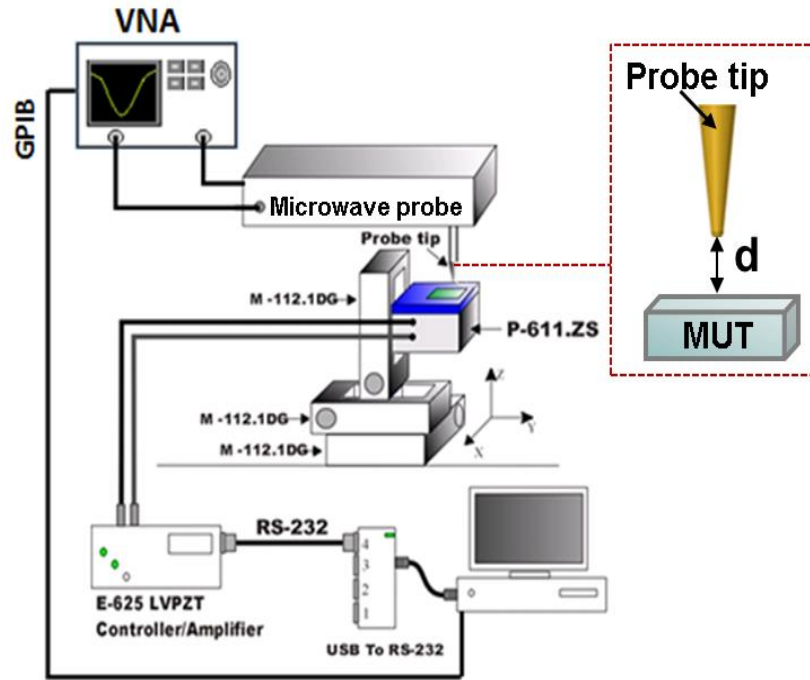


Figure 3-1 DR-based NFMM. (a) Microwave probe. (b) Experimental setup from [72] © (2003).

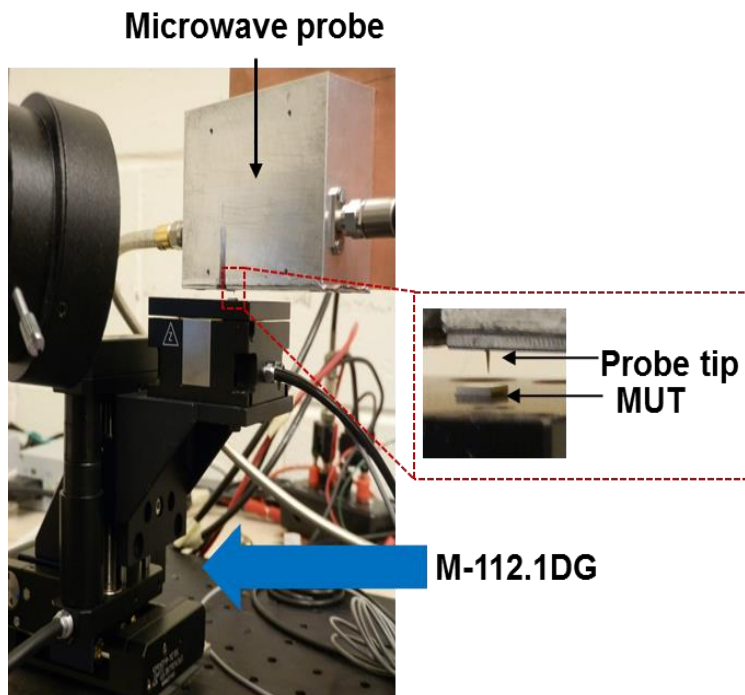
Additionally, a novel height control mechanism which detects the contact point between the probe tip and metallic samples is discussed. This mechanism allows the NFMM to scan over a metallic sample at a constant height reducing the surface topography artifacts from NFMM measurements. Advantages of this mechanism are that it is simple and low cost since no additional distance sensors are required.

3.2 Experimental Setup

An illustration of the DR-based NFMM experimental setup is shown in. It consists of an 8753 vector network analyzer (VNA) which is used as a microwave source and detection system, a dielectric resonator (DR) -based microwave probe and a scanning system. The scanning system employs a combination of xyz PI M112-1DG micro-translations stages and a PI P-611 z piezo-stage for coarse and fine displacement. The unidirectional repeatability of the PI M112-1DG is 100 nm and the closed loop resolution of the PI P-611 stage is 2 nm. During a scan, the microwave probe is kept fixed while the MUT, sitting on the positioning system, moves under the probe tip at a tip-sample distance d following a rectangular grid pattern. For positioning controlling, each M112-1DG stage is connected to a PI 863 Mercury controller and the PI P-611 stage is connected to a PI E-610 servo controller. All the controllers are computer-controlled using a set of programs created in LabVIEW 2010. The microwave probe and the scanning system are mounted on top of a table supported by an active isolation frame in order maximize vibration isolation. A photograph of the DR-based microwave probe, the scanning system and the MUT is shown in Figure 3-2(b).



(a)



(b)

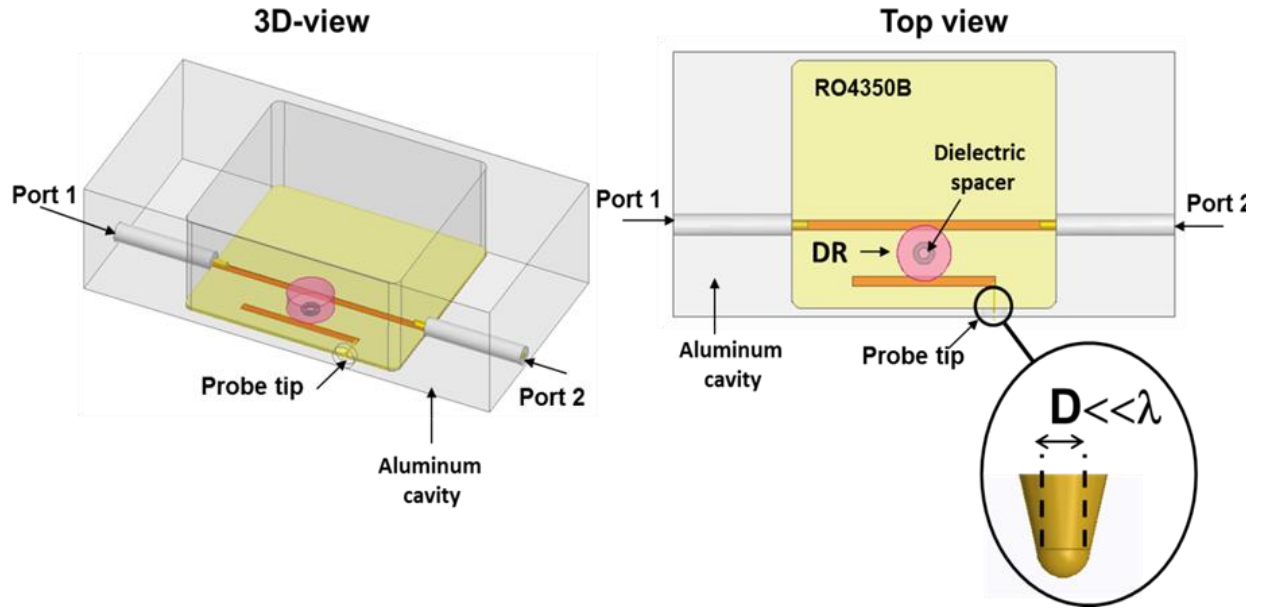
Figure 3-2 (a) Illustration of the DR-based microwave microscope. (b) Photograph of the DR-based microwave probe, positioning system and MUT.

3.3 Dielectric Resonator-Based Probe Design

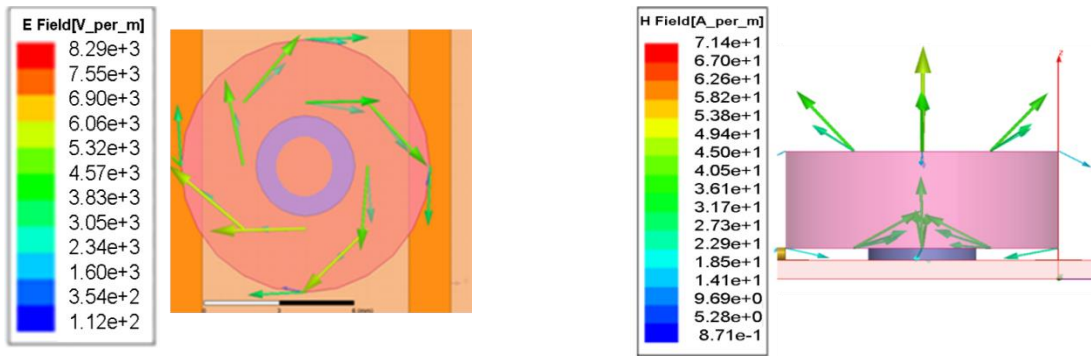
The microwave probe is comprised of a resonant circuit coupled to a conductive sharp tip as shown in Figure 3-3(a). The resonant circuit consists of a dielectric resonator mounted on a RO4350B substrate and magnetically coupled to a $50\ \Omega$ microstrip line. The diameter, height, dielectric constant and unloaded quality factor of the DR are 10.10 mm, 4.04 mm, 37 ± 0.2 and 8690 (Dielectric Materials-Part Number D101), respectively. The DR is operated in the TE_{108} mode with resonance frequency of 5.73 GHz, which represents the mode with the lowest resonance frequency. Characteristic electromagnetic fields of the TE_{108} mode are obtained from electromagnetic simulation of the microwave probe in the Ansys High Frequency Structure Simulator (HFSS) and are shown in Figure 3-3(b). To increase the coupling between the DR and the microstrip line, a dielectric spacer with thickness of 0.5 mm, radius of 2 mm, and dielectric constant of 11.5 ± 0.5 is placed under the DR. The sharp tip used is a commercially available gold-coated tungsten tip with radius of $25\ \mu\text{m}$ (Micromanipulator- model number 7G-25) that is attached to a microstrip line $3\lambda_d/4$ long. In order to prevent radiation, degradation of the resonator quality factor and interference of the electromagnetic waves from outside, the substrate is enclosed in a rectangular cavity. The length, width and height of the cavity are 50 mm, 45 mm and 22 mm, respectively. The tungsten tip protrudes beyond one of the walls of the cavity through a hole with diameter of 5 mm.

A lumped-element circuit model of the probe in the vicinity of resonance is presented in Figure 3-4. In the symmetry xx' plane, the DR is modeled by a parallel RLC circuit with parameters R_1 , L_1 , and C_1 , which depend on the DR characteristics, surroundings, and the distance between the resonator and the microstrip lines [37]. The magnetic coupling between the DR and the microstrip lines is modeled by the transformers with turns T_1 and T_2 . The parameters R_t , L_t and C_t model the tungsten tip. The coupling between the tip and the sample is represented by C_c . Insulating and semiconductor samples are modeled by R_s and C_s (see Figure 3-4(a)), whereas metallic samples are modeled by R_s and L_s (see Figure 3-4(b))

[39, 51]. The capacitance C_c has been approximated to the capacitance of a parallel plate capacitor in [71], where the tip is considered flat and the tip-sample distance is assumed to be significantly smaller than the tip size. A more general approach for calculating this capacitance was discussed in section 2.6. Lumped-element circuit models of resonant microwave probes based on stripline resonators and coaxial resonators have been discussed in [6, 37, 74, 75].



(a)



(b)

Figure 3-3 (a) Schematic of the dielectric resonator (DR)-based near-field scanning microwave probe. The inset shows the tip geometry, (b) Electric (left) and Magnetic (right) Field distributions for the $TE_{01\delta}$ mode in the equatorial and meridian plane simulated in HFSS, respectively.

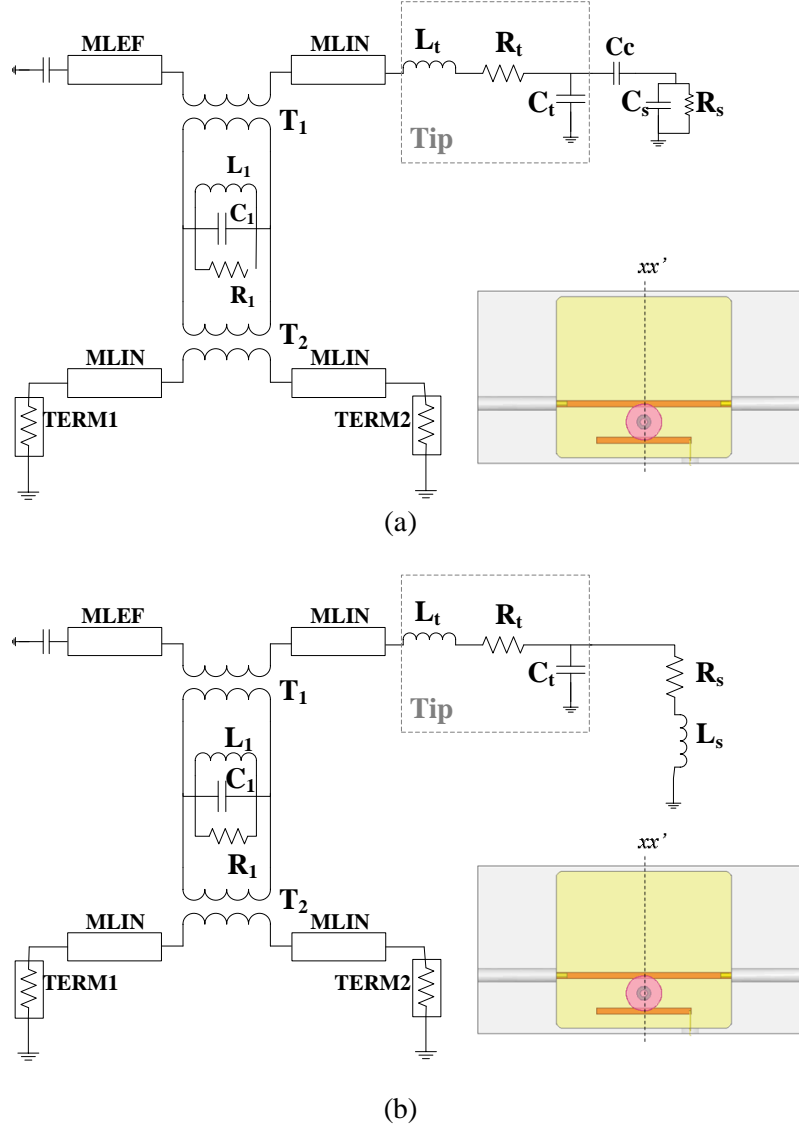


Figure 3-4 Lumped-element circuit model of the DR-based microwave probe and (a) insulating sample (b) metallic sample.

The equivalent values for R_1 , C_1 , L_1 , T_1 and T_2 are determined using [69, 76]

$$R_1 = 2\beta_c Z_0 \quad (35)$$

$$C_1 = \frac{Q}{2\pi f_0 R_1} \quad (36)$$

$$L_1 = \frac{R_1}{2\pi f_0 Q} \quad (37)$$

$$T_1 = T_2 = \sqrt{\frac{2\beta_c Z_0}{R_1}} \quad (38)$$

where $\beta_c=16.22$ and $Q=2608$ are found using (30), (31) and (32) and the measured S_{21} parameters of the DR-based microwave circuit without attaching the probe tip to the microstrip line. Values for L_t , R_t and C_t are determined by matching the measured S_{21} parameters of the DR-based microwave circuit (including the probe tip) to the models in Figure 3-4. Table 3-1 summarizes the equivalent lumped circuit parameters of the DR-based microwave probe.

Table 3-1. Equivalent lumped circuit parameters of the DR-based microwave probe

	R₁ (Ω)	L₁ (nH)	C₁ (pF)	T₁ and T₂	L_t (nH)	R_t (Ω)	C_t (pF)
Value	1600	0.017015	45.33	0.99 and 0.99	0.1	0.3	0.2

To gain a better understanding of the influence of the Q of the resonator and the coupling capacitance C_c on the sensitivity of the probe, circuit simulation of the circuit shown in Figure 3-4(a) is conducted in Keysight Technologies Advanced Design System (ADS). For clarification, sensitivity of a near-field resonant probe refers to the ability of the probe to detect small variations in the electromagnetic properties of the MUT (C_s (ϵ'_r) and R_s (ϵ''_r)). To study the influence of C_c on the sensitivity of the DR-based NFMM, C_c is varied between 50 fF to 200 fF for different C_s values ($50 \text{ fF} < C_s < 200 \text{ fF}$). From S_{21} plots in Figure 3-5(a), it is clear that the probe is sensitive to variations in C_s and that for a fixed C_c , F_r and Q decrease as C_s increases, and this change is more evident for higher C_c values. This result indicates that

the sensitivity of the probe can be enhanced by increasing C_c , which can be accomplished through a reduction of the tip-sample distance or/and an increase in the tip size.

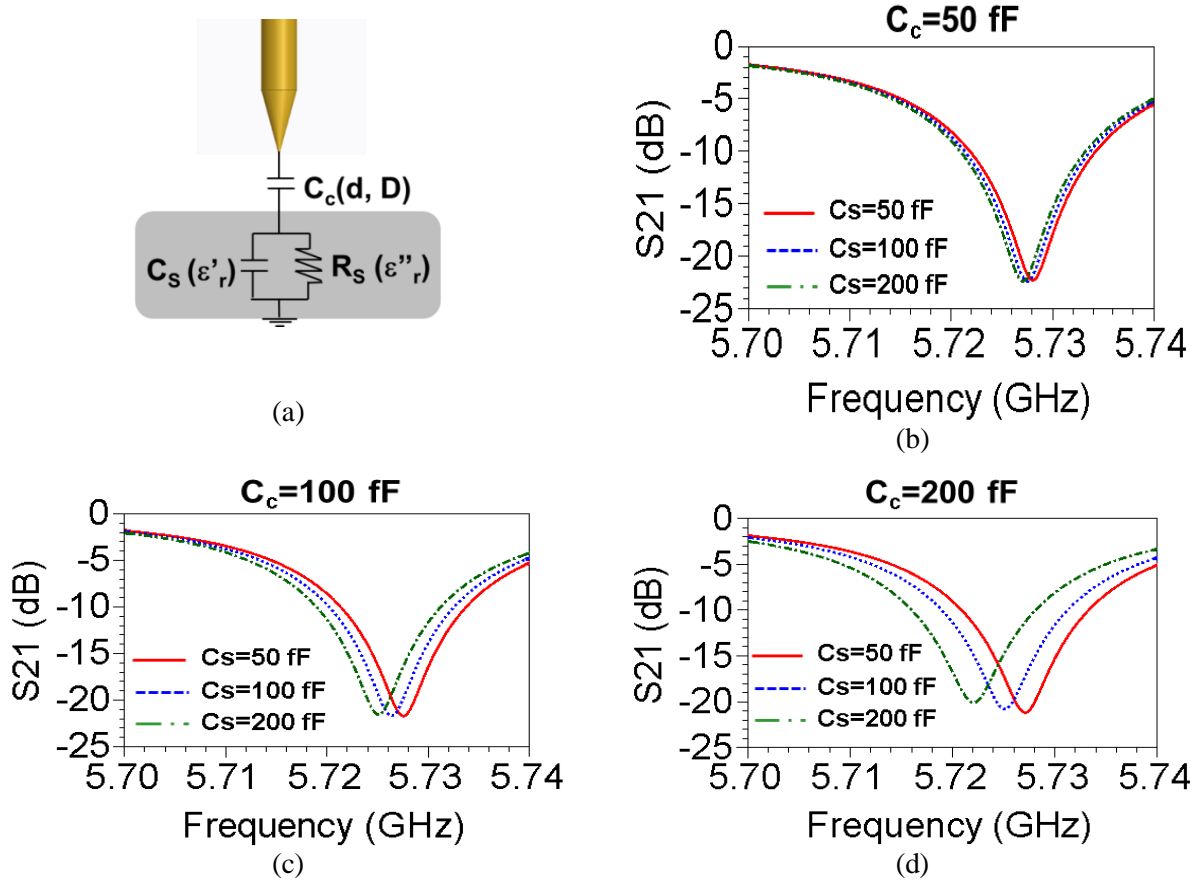


Figure 3-5 (a) Schematic of the tip-insulating sample interaction. $|S_{21}|$ parameter plots for different C_s values and (b) $C_c=50$ fF, (c) $C_c=100$ fF and (d) $C_c=200$ fF.

The influence of Q of the DR on the sensitivity of the NFMM to detect small variations in R_s is studied by varying R_1 , and therefore Q , for different R_s values ($0.16 \Omega < R_s < 1.06 \Omega$). Figure 3-6 (a) shows the lumped element circuit of a metallic sample where $L_s=0$ nH since the sample is considered to be non-magnetic. Figure (b) and Figure (c) show the S_{21} parameter of the probe for $C_c=200$ fF, $R_1=100 \Omega$ ($Q=116$) and $R_1=2000 \Omega$ ($Q=1909$), respectively. It can be observed that the sensitivity of the DR-based probe to detect small variations in R_s ($\Delta R_s = 1.06 \Omega - 0.69 \Omega = 0.37 \Omega$) increases as Q increases. The importance of using high Q resonators in NFMM for enhancing its sensitivity has been reported in [71].

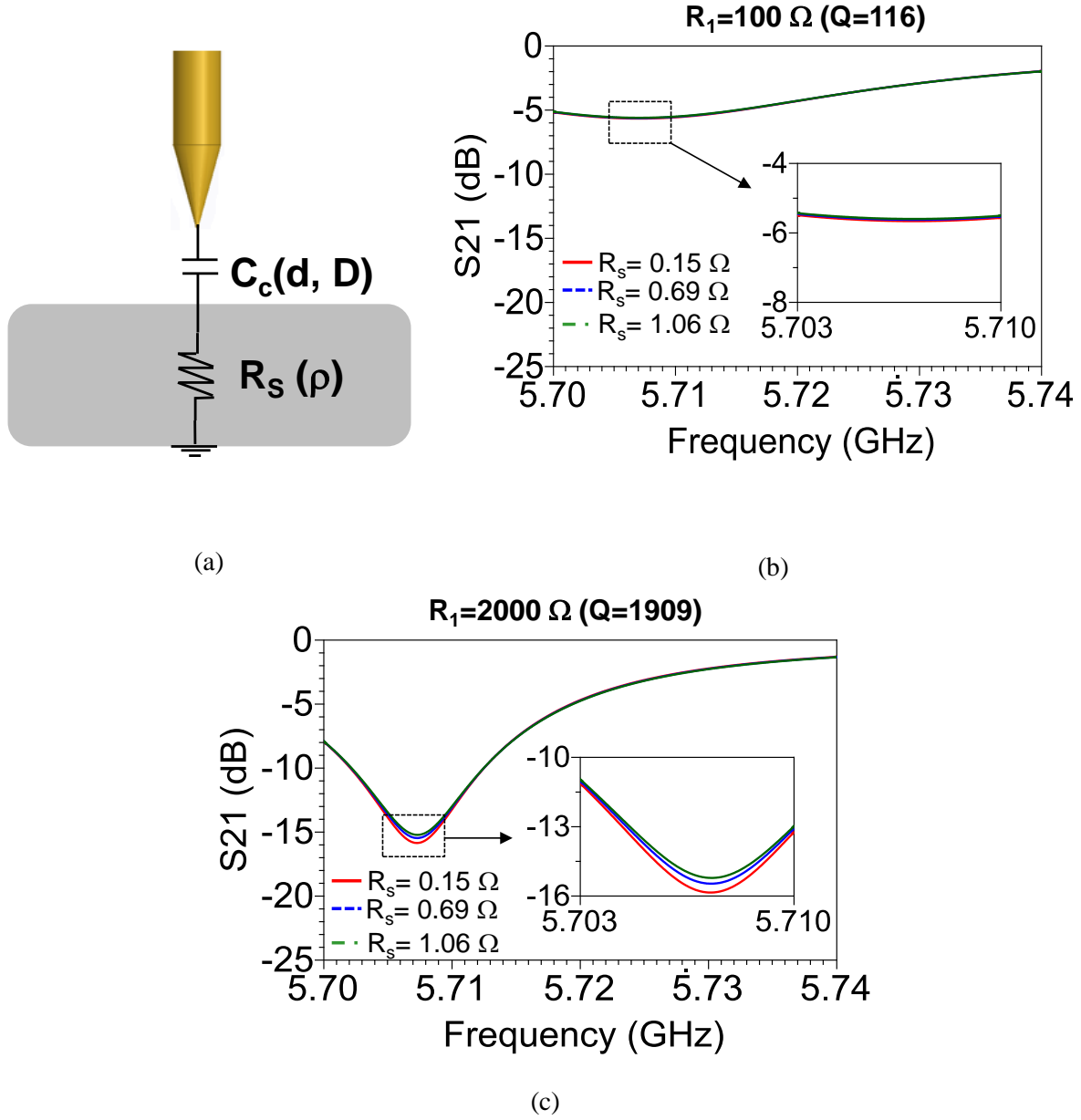


Figure 3-6 (a) Schematic of the tip-metallic sample interaction. $|S_{21}|$ parameter plots for different R_s values and (b) $R_1=100 \, \Omega$ ($Q=116$), (c) $R_1=2000 \, \Omega$ ($Q=1909$).

The microwave probe and MUT can also be effectively modeled using a combination of circuit and numerical electromagnetic simulation (referred to as co-simulation) in order to reduce the simulation time and computational resources required to model parts of the probe and sample that have different length scales and complexity. Circuit simulation using ADS is used to simulate the cavity, microstrip

lines, DR, and a section of the probe tip whereas the HFSS is used to simulate the interaction between the probe tip and sample as shown in Figure 3-7. The advantage of using HFSS to model the tip-sample interaction over the lumped-element circuit model in Figure 3-4 is that knowledge of the relationship between the electromagnetic properties of the sample, and R_s , L_s and C_s parameters is not required. The S1P block in Figure 3-7 contains the imported Touchstone S-parameter file from the HFSS simulation. The schematic of the tip and sample used in HFSS is shown in the inset of Figure 3-7; de-embedding of the length L_p is carried out in HFSS in order to move the reference plane to the end of the cavity.

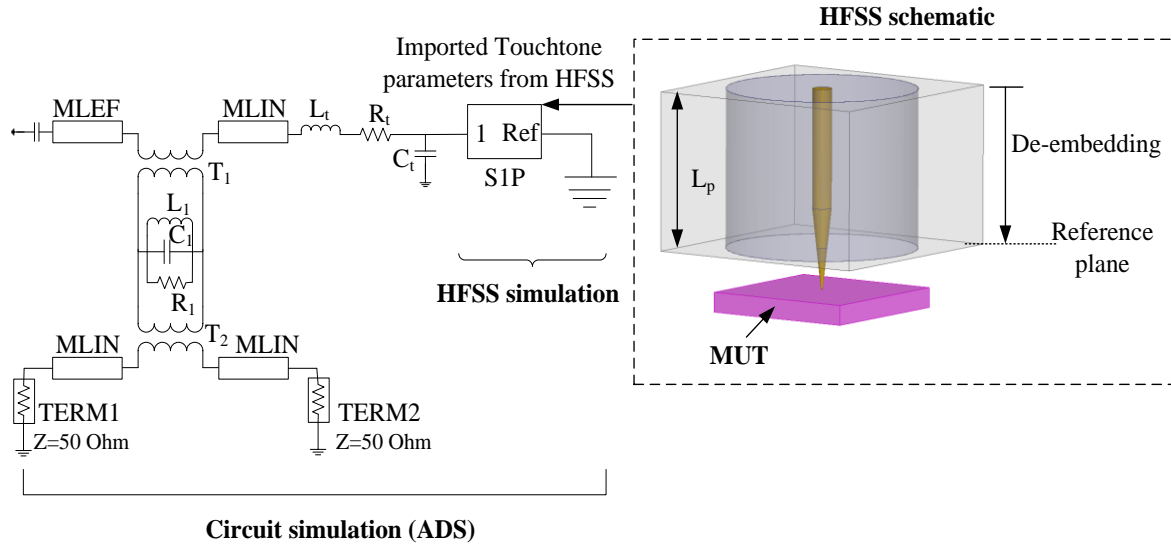


Figure 3-7 Schematic of the co-simulation of the microwave probe. The circuit combines circuit components such as coaxial lines and a capacitor along with the full-wave simulation of the tip-fork-sample interaction.

The co-simulated and measured frequency response of the microwave probe for the MUT being air is shown in the $|S_{21}|$ parameter plot in Figure 3-8. It can be seen that measured and simulated F_r are 5.726 GHz and 5.723 GHz, respectively. The measured and simulated Q factor are calculated using (32) and (34) and are found to be $Q = 982$ and $Q = 1144$, respectively. Frequency response obtained with the model shown in Figure 3-4 is in good agreement with measurements.

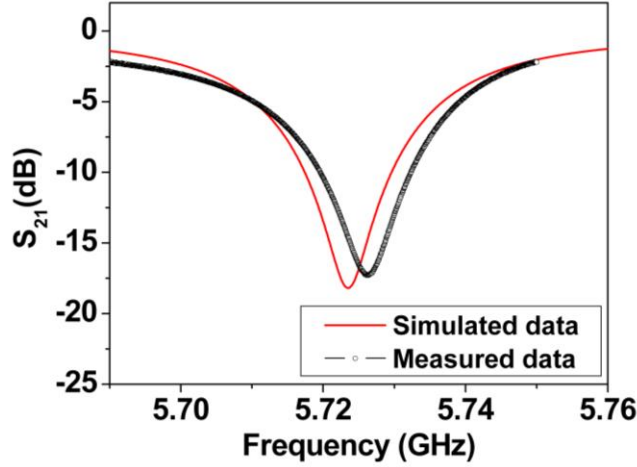


Figure 3-8 Simulated and measured S_{21} vs. frequency of the DR-based microwave probe.

3.4 Distance-Following Feedback System

The DR-based NFMM employs a simple and low-cost distance-following feedback mechanism that does not require distance sensors to be attached to the probe and can be used when studying metallic samples. This mechanism monitors the frequency shift that occurs at the contact point between the tip and the conductive sample. Circuit simulations of the lumped-element circuit model shown in Figure 3-4 (b) when the tip is in contact ($C_c = 0$ fF), and when it is far from the conductive sample ($C_c = 0.2$ pF) are carried out using ADS.

Figure 3-9 shows the modeled and measured S_{21} parameter of the microwave probe for $d = 0$ μm and $d = 10$ mm. It can be seen that at the contact point with the metal, the resonance frequency shifts upwards by about 18.4 MHz compared to the position far from the sample. Thus, this mechanism allows imaging of the conductivity and topography simultaneously; the contact point is first established by monitoring the resonance frequency. After detecting the soft contact, the sample can be lowered and the resonant properties of the probe and z position are recorded.

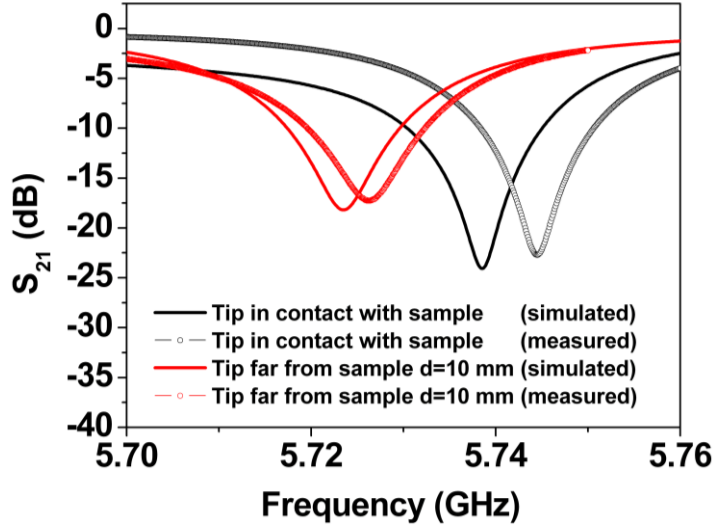


Figure 3-9 Measured and simulated S_{21} parameters of the DR-based probe when the tip is far from and in contact with a conductive sample.

3.5 Conclusion

This chapter has presented the design of a DR-based NFMM operating at 5.72 GHz. The NFMM employs a DR-based microwave probe that exhibits high Q ($Q=986$). The microwave probe has been simulated using a combination of circuit and electromagnetic simulation, and simulation results show good agreement with measurements. This is the first time that lumped-element circuit model of a DR-based probe is presented, and it was used to gain a better understanding of the influence of microwave probe parameters such as Q and coupling capacitance between the probe tip to the sample. It was found that the sensitivity of the DR-based probe improves by increasing Q and the coupling capacitance between the probe and the sample. This capacitance can be increased by increasing the tip apex size and reducing the tip-sample distance. In addition, a novel and low-cost tip-sample distance control mechanism that allows the NFMM to perform a xy scan at a constant height from the metallic sample's surface is also described.

CHAPTER 4 : COAXIAL TRANSMISSION LINE RESONATOR-BASED MICROWAVE MICROSCOPE

4.1 Introduction

This chapter presents the design, simulation and testing of a coaxial transmission line resonator-based NFMM that operates in non-contact mode. The experimental setup of this microscope is similar to that presented in Chapter 3 with the exception of the microwave probe and the distance-following feedback system employed. The microwave probe uses a half-wavelength coaxial transmission line resonator terminated in a parylene C-coated tungsten tip. The main advantage of this probe design over the DR-based probe is that it can be integrated with a quartz tuning fork-based height control system that enables non-contact operation and the extraction of material properties from surface topography artifacts. The influence of the contact between the probe tip and the quartz tuning fork on both the quartz tuning fork's operation and microwave probe response is discussed in this chapter. Finally, the electrochemical etching process and conditions employed to shape the tungsten tip used in the microwave probe are presented.

4.2 Experimental Setup

An illustration and photograph of the experimental setup using a coaxial-based microwave probe are presented in Figure 4-1(a) and (b), respectively. The microwave source and detection system is an 8753 vector network analyzer (VNA) and the positioning system is the same shown in Section 3.2. The

manual A-RH Line Tool micropositioner is used to adjust the coupling gap between the coaxial resonator and the feed line in order to achieve critical coupling between the resonant probe and the VNA.

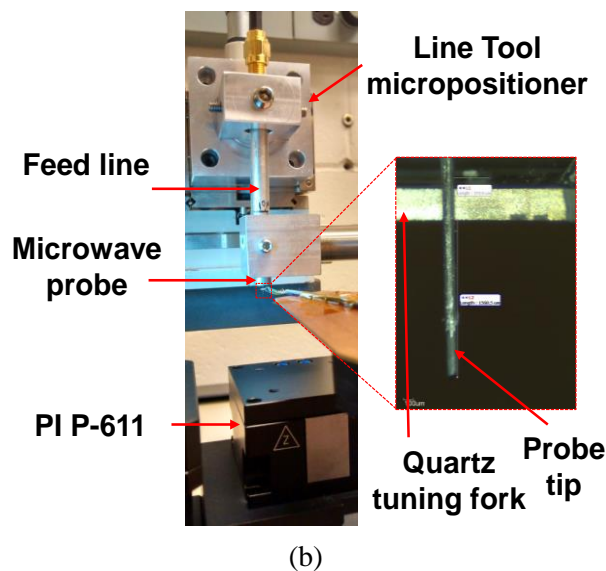
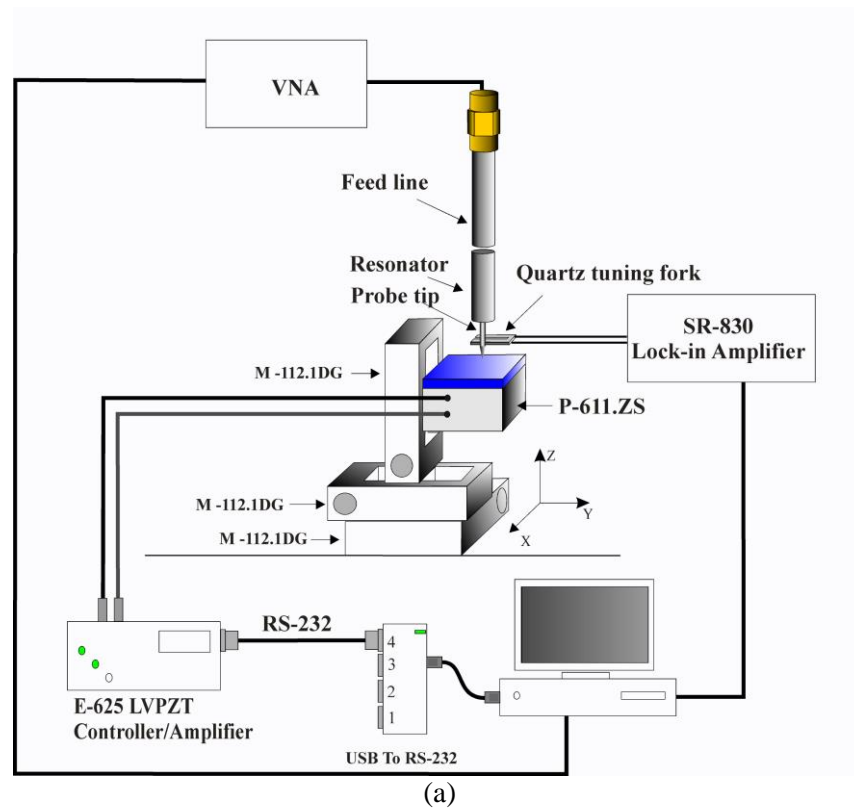


Figure 4-1 (a) Illustration of the coaxial transmission line resonator-based NFMM experimental setup. (b) Photograph of the coaxial resonator probe, feed line and the micropositioner. The inset shows the probe tip in contact with the quartz tuning fork.

4.3 Coaxial Transmission Line Resonator-Based Probe Design and Distance Following Feedback System

The resonant microwave probe is a half-wavelength coaxial transmission line resonator operating at 5 GHz that is critically coupled to the VNA through an adjustable gap and a feed line as shown in Figure 4-2. The resonator and feed line are fabricated using semi rigid coaxial cable. From the inset, it can be seen that a short section of the copper inner conductor of the resonator is removed and replaced with a stainless steel tube with length $L_s = 3$ mm, in which a tungsten wire with length of 4.5 mm and radius of 100 μm is inserted. The end of the wire is sharpened down to a few microns using electrochemical etching prior to inserting it in the stainless steel tube. The electrochemical etching process and conditions are described in Section 4.4. The copper inner conductor and the stainless steel tube are glued together using H20E silver epoxy. During scanning, the probe tip remains fixed while the sample is positioned using a system that employs a combination of PI M112-1DG xyz micro-translations stages and a PI P-611 z piezo-stage for coarse and fine displacement, respectively.

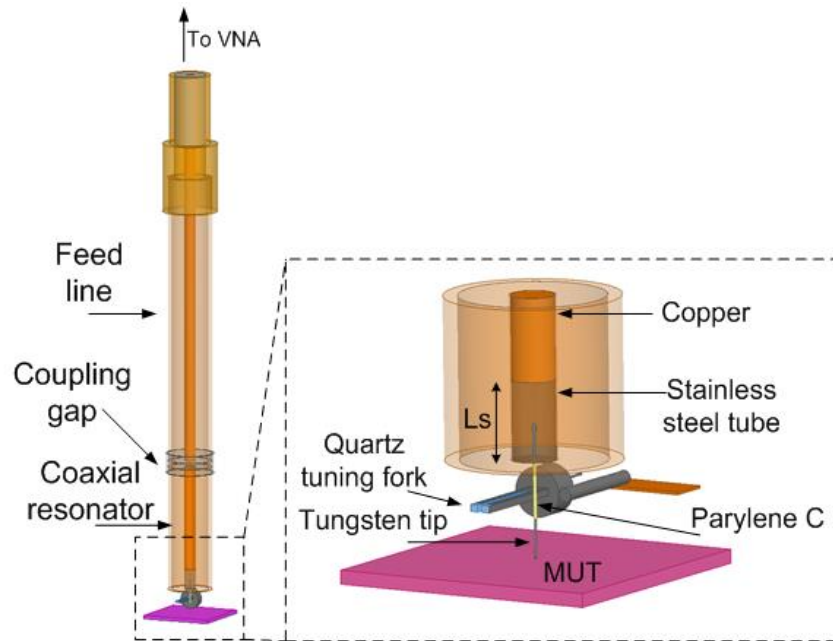
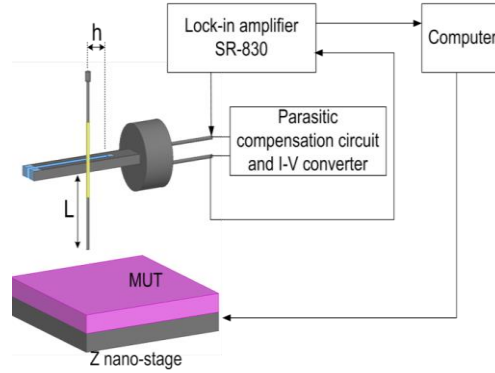


Figure 4-2 Schematic of the coaxial-based probe. The inset shows a close-up view of the probe tip and the quartz tuning fork used as a distance sensor in the distance following feedback system.

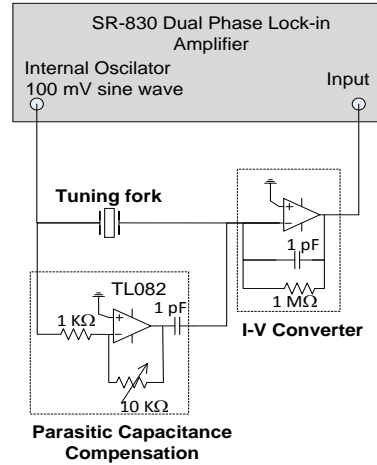
The distance-following feedback system employs a commercially available Mad City Labs medium size quartz tuning fork as a distance sensor. This type of sensor is frequently used in scanning microscopes because of its mechanical stability, high quality factor, high stiffness and ability to operate without illumination. A quartz tuning fork can be driven either mechanically by shaking the fork at its mechanical resonance or electrically by applying an AC voltage to its electrodes [77, 78]. When electrically driven, the piezoelectric material bends and the amount of mechanical bending is proportional to the voltage applied. In this work, the quartz tuning fork is electrically driven by a sinusoidal signal with voltage amplitude V_{rms} of 100 mV which is obtained from the internal function generator of an SR-830 lock-in amplifier as shown in the experimental setup in Figure 4-3(a). The lock-in amplifier also measures the current generated at the terminals of the tuning fork. The parasitic capacitance compensation circuit shown in Figure 4-3(b) is used for removing the capacitance created by the fork's terminals, which is typically of the order of a few picofarads and produces an undesired resonance that breaks the symmetry of the fork's resonance as presented in Figure 4-4 [79]. A 10 K Ω potentiometer was adjusted until the tuning fork's resonance response is symmetrical with frequency. The symmetry was achieved for $R=1450 \Omega$. An I-V converter is used to convert the electrical current generated at the terminals of the fork to voltage.

In order to integrate the distance-following feedback system with the NFMM, the quartz tuning fork is placed in contact with the tungsten tip without using glue or epoxy as illustrated in Figure 4-3(a). This approach facilitates the replacement of the tip and/or tuning fork in the system [80]. The tungsten tip is coated with a 10 μm thick layer of parylene-C to avoid an electrical short when in contact with the tuning fork electrodes. Parylene-C was deposited using a 2010 PDS Labcoater. The contact between the probe tip and tuning fork/holder has significant implications on both the tuning fork resonance response and the microwave probe performance. As a result of the contact with the tip, the tuning fork experiences degradation in the amplitude of vibration at resonance and a shift of the resonance frequency. The degradation of the Q factor of the tuning fork can limit its use as a distance sensor and this fact is usually

overlooked in NFMM designs. In the NFMM in [33], a tuning fork Q of $\sim 1,000$ is maintained when in contact with the probe tip in order for the phased-locked loop of the feedback controller to operate. In [81], it is shown that the resonance of a quartz tuning fork in a near-field optical microscope vanishes if the fiber optic is glued to the extremities of the tuning fork. Herein, we study the frequency response of the quartz tuning fork in contact with the parylene-C coated tungsten tip for different h and L values (see Figure 4-3 (a). Figure 4-5 shows that the shift in the resonance peak and the voltage attenuation at resonance can be reduced by decreasing h and increasing L . For the rest of this work, h and L are $400\text{ }\mu\text{m}$ and $1760\text{ }\mu\text{m}$, respectively.



(a)



(b)

Figure 4-3 (a) Schematic of the distance following feedback system. (b) Parasitic capacitance compensation circuit.

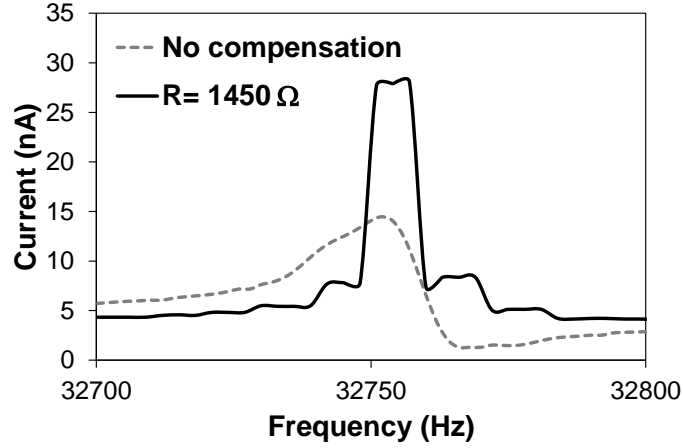


Figure 4-4 Measured output electrical current of the quartz tuning fork vs. frequency with and without a parasitic compensation circuit.

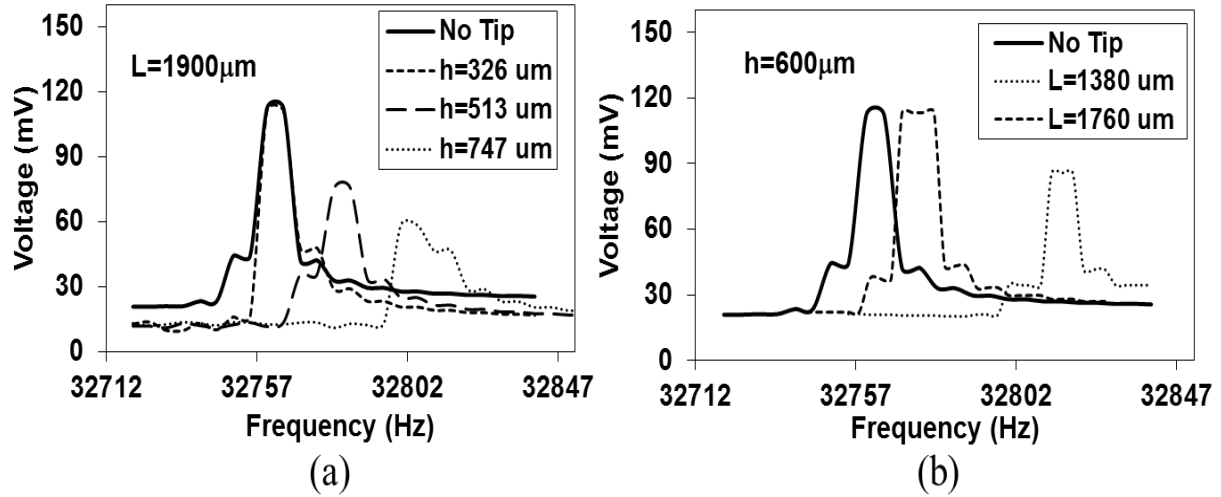


Figure 4-5 (a) Frequency spectra of the tuning fork for $L=1900 \mu\text{m}$ and different values of h distance. (b) Frequency spectra of the tuning fork for $h=600 \mu\text{m}$ and different values of L distance. For comparison purposes, the response for the bare tuning fork (No Tip) is included in the spectra.

To verify the functionality of the quartz tuning fork-based distance following feedback system, voltage oscillation amplitude of the tip-fork system is measured as a function of the tip-sample distance. Figure 4-6 indicates that the voltage remains undisturbed for $d > 35 \text{ nm}$ but it drops to 50% of its unperturbed value for $d \approx 16 \text{ nm}$ and it gets completely damped at the contact point with the sample

(alumina). Thus, it is evident that distance control can be achieved by monitoring and controlling the voltage at the fork terminals. This approach was tested during a scanning across a $\text{Ba}_{0.5}\text{Sr}_{0.5}\text{TiO}_3$ thin film 53 μm wide and 450 nm thick on an alumina substrate as illustrated in the profile shown in Figure 4-7(a). The tip-sample distance was kept constant to an average value of 22 nm by controlling the voltage within the range of 70 mV and 110 mV. From the profiles shown in Figure 4-7(b) it can be seen that the NFMM measurement is able to resolve the $\text{Ba}_{0.5}\text{Sr}_{0.5}\text{TiO}_3$ thin film from the substrate and that the NFMM profile agrees very well with the profile obtained using a Veeco Dektak 150 surface profilometer whose stylus has a radius of 5 μm . The percentage difference in the average height and width of the BST layer between NFMM and profilometer are 10.5% and 11%, respectively. The reason for the difference is because the NFMM tip radius is double that of the stylus which results in a degradation of the NFMM spatial resolution. Advantages of using NFMM for topography measurements are that it is non-contact, non-destructive and images of surface topography can be easily obtained by scanning over a surface.

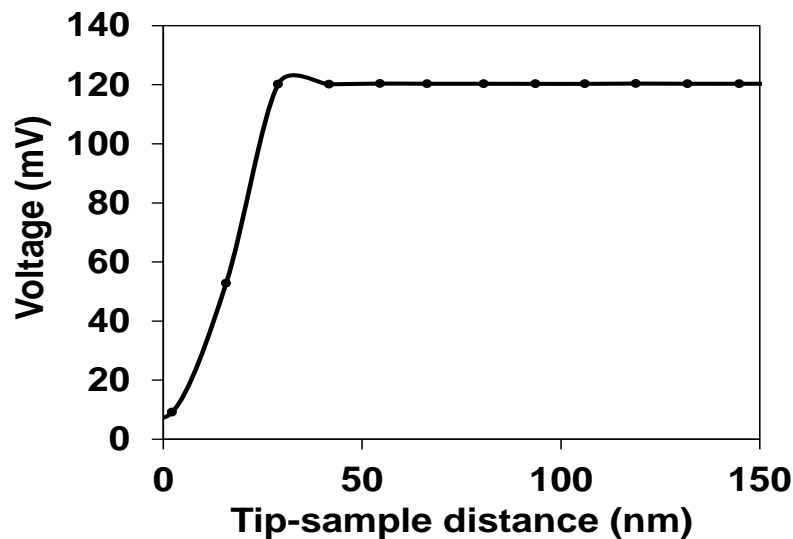


Figure 4-6 Output voltage of the quartz tuning fork vs. tip-sample distance.

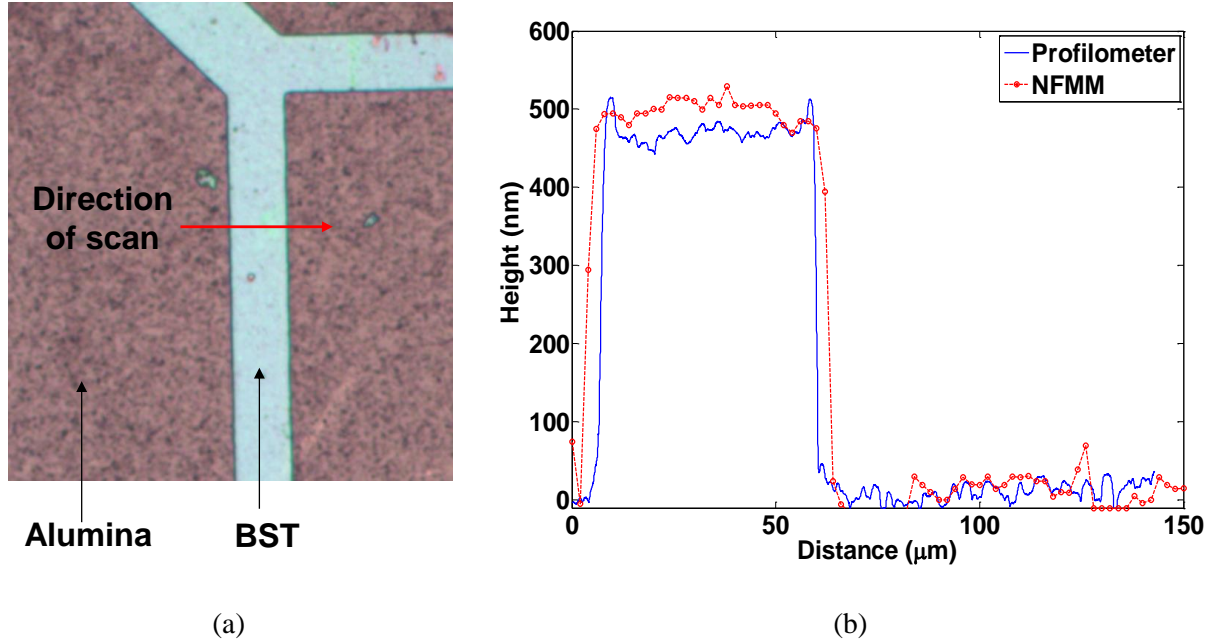


Figure 4-7 (a) Micrograph showing the direction of scan for profile measurement of a $\text{Ba}_{0.5}\text{Sr}_{0.5}\text{TiO}_3$ trace on alumina substrate. (b) Line profile across the $\text{Ba}_{0.5}\text{Sr}_{0.5}\text{TiO}_3$ using NFMM and a commercial profiler (Veeco Dektak 150).

The NFMM system can be effectively modeled using a combination of circuit and numerical electromagnetic simulation (referred to as co-simulation) in order to reduce the simulation time and computational resources required to model parts of the system that have different length scales and complexity. Circuit simulation using Keysight Technologies Advanced Design System (ADS) is used to simulate the connector, feed-line and coaxial transmission line resonator whereas Ansys High Frequency Structure Simulator (HFSS) is used to simulate the interaction between the probe tip, fork and sample as shown in Figure 4-8. The capacitor C_g models the coupling gap between the half-wavelength coaxial resonator and the feed line. The S1P block contains the imported Touchstone S-parameter file from the HFSS simulation. Typically, a coupling capacitor in series with a parallel RC circuit is used to model the tip-insulating sample coupling and material properties [16, 51], but in this case the complexity of the tuning fork configuration requires the HFSS finite element analysis. The schematic of the tip, fork and

sample used in HFSS is shown in the inset of Figure 4-8; de-embedding of the length L_s is carried out in HFSS in order to move the reference plane to the end of the open-ended coaxial resonator.

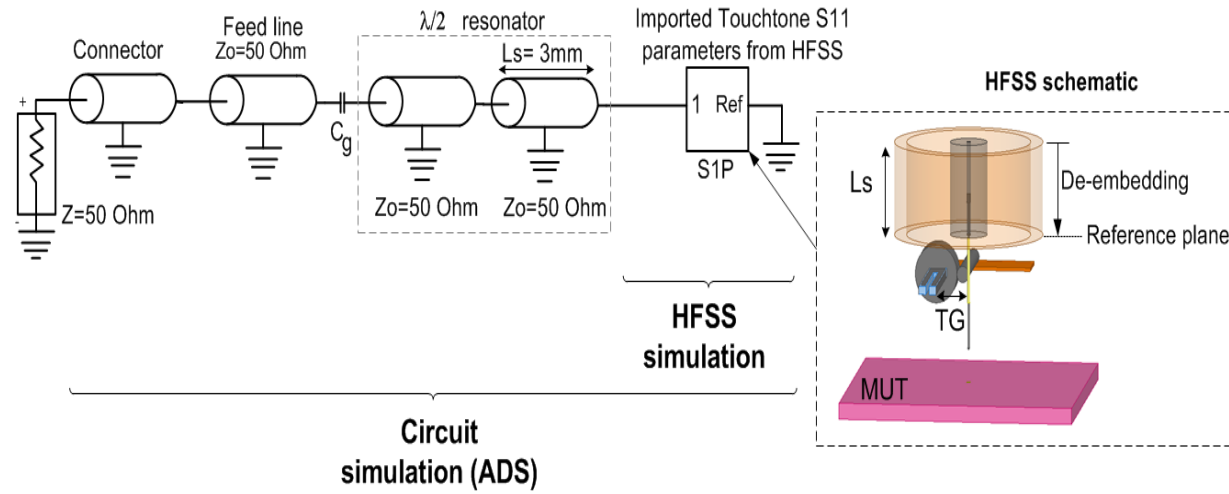


Figure 4-8 Schematic of the co-simulation of the microwave probe. The circuit combines circuit components such as coaxial lines and a capacitor along with the full-wave simulation of the tip-fork-sample interaction.

The coupling of the resonator to the source (VNA) is changed when the tuning fork comes into proximity with the probe tip, requiring proper tuning of the coupling gap (see inset in Figure 4) between the feed line and resonator. As shown in Figure 4-9(a), the resonant frequency and Q are both reduced as the gap between the fork and probe tip (TG) is reduced. This behavior can be explained by the fact that capacitance and losses are added to the system by the fork and holder. Figure 4-9(b) shows the measured and simulated S_{11} of the microwave probe when the tip is in physical contact with the tuning fork, which is the operating mode of the NFMM, after the coupling gap is adjusted for critical coupling. The adjustment of this gap is done by reducing it from $1120\ \mu\text{m}$ to $700\ \mu\text{m}$. A phase shifter can also be used as a tuning mechanism for a coaxial-based probe as explained in [33].

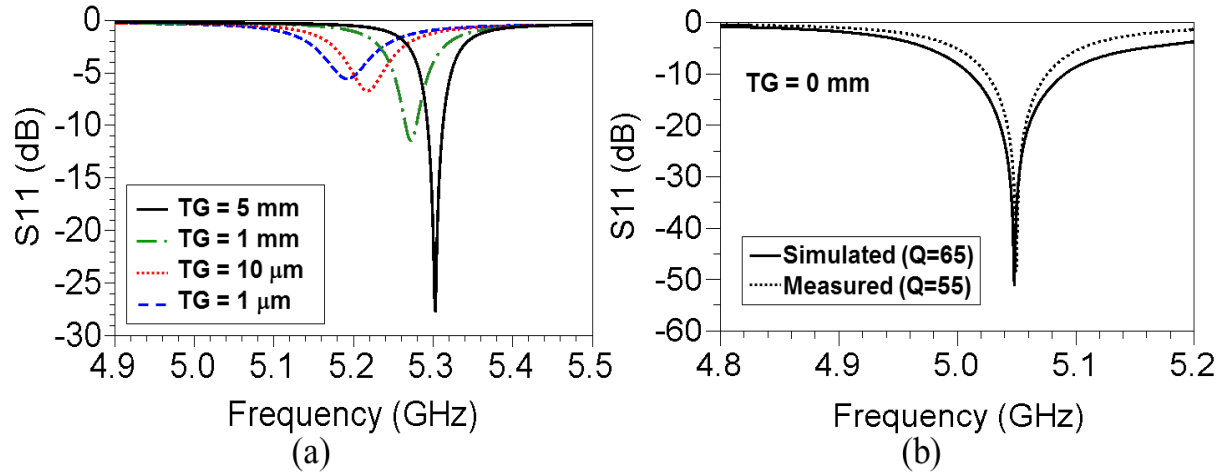


Figure 4-9 (a) Simulated S_{11} parameter vs. frequency for different TG values. (b) Measured and simulated S_{11} parameter vs. frequency for the tip in contact with the quartz tuning fork; the coupling gap between the feed line and the coaxial resonator is adjusted after contact so that the probe is critically coupled to the source.

4.4 Electrochemical Etching of the Tungsten Tip

The tungsten wire (Thermoshield -Tungsten 99.95 %) used as a probe tip has a shaft radius of 100 μm which can be sharpened using electrochemical etching [82-84], ion milling [85] or oxidation processing [86]. Among these techniques, electrochemical etching is very popular because it is low-cost, simple and apex with apex radius as small as 10 nm can be achieved [84] The electrochemical etching process is illustrated in Figure 4-10.

The tungsten wire is immersed in an alkaline solution such as NaOH or KOH and a meniscus around the wire is created because of the surface tension of the solution. The electrochemical etching starts once the tungsten wire (anode) is connected to the positive terminal of a DC power supply and an electrode such as a stainless steel wire (cathode) is connected to the negative terminal, thereby closing the circuit. During the etching process, ions responsible for the necking shape of the wire (OH^- and WO_4^{2-}) are produced. Low concentration of OH^- ions near the top of the meniscus and the WO_4^{2-} anodic flow present on the lower part of the immersed wire result in higher etching rate at the bottom of the meniscus explaining the necking shape [83, 84]. Thus, a sharp tip is created when the etching around the meniscus

reaches a point where the necking part is so thin that is not able to sustain the lower part of the immersed wire and this wire section drop off. At this point, the electrical current drops and the electrochemical etching stops.

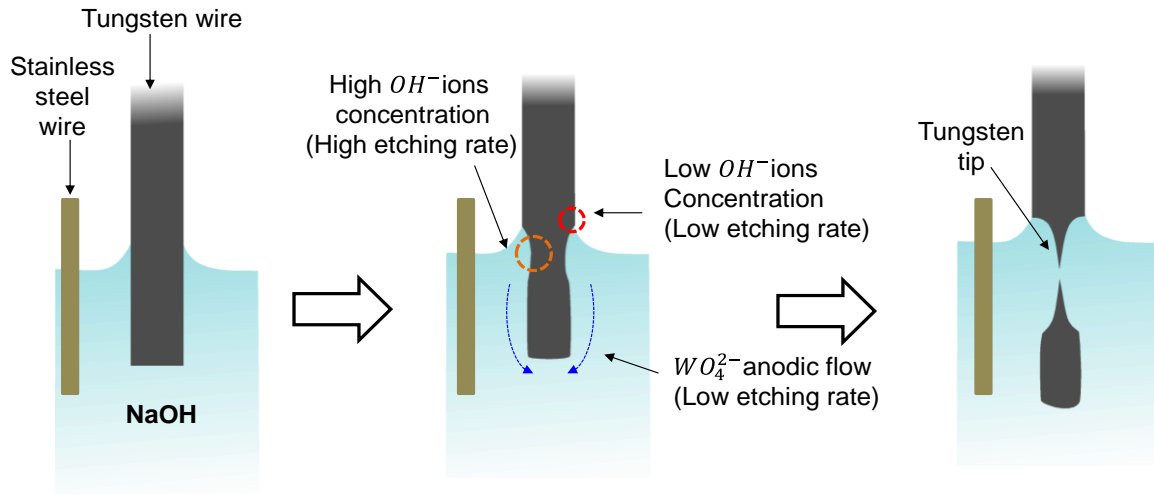
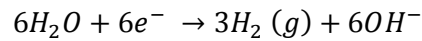


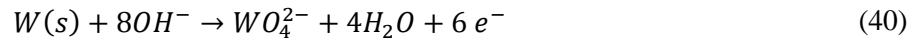
Figure 4-10 Illustration of the electrochemical etching of a tungsten tip.

The reaction that occurs during the electrochemical etching is [87]:

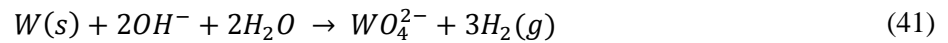
Cathode: (39)



Anode:



Overall:



Electrochemical etching can be static, dynamic or a combination of both. Static electrochemical etching means that the tungsten wire remains static during the etching process whereas in dynamic

etching, the tungsten is continuously lifted up and parameters such as lifting up distance and speed control the final shape of the probe tip [83]. Static etching controls the apex size and produces tips with exponential shape and dynamic etching produces conical-shape probe tips. It has been found that the aspect ratio can be reduced by increasing the applied voltage [88] and by increasing electrolyte concentration [83].

In this work static electrochemical etching is used and the electrolyte concentration is not varied. The positive terminal of a dc power supply is connected to the tungsten wire immersed in NaOH (2M) and the negative terminal is connected to a stainless steel ring electrode as shown in Figure 4-11. The ring-shaped terminal is positioned just below the surface of the solution using a Line Tool micropositioner in order to reduce the H_2 bubbles that reach the immersed wire which disturb the process and produce undesired effects on the tip shape [89].

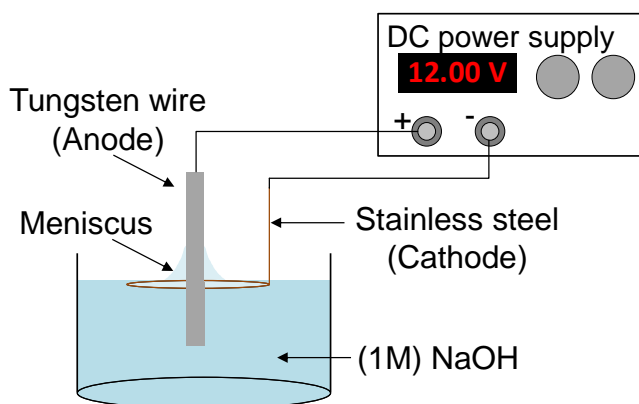


Figure 4-11 Illustration of the experimental setup used for electrochemical etching of tungsten tips.

Voltage conditions used to create tungsten tips with different aspect ratios and apex sizes are summarized in Table 4-1. Figure 4-12 shows SEM micrographs for tips 1-4. As expected, tips 1 and 2 have higher aspect ratios than those of tips 3 and 4 because lower voltage is used. The influence of the voltage on the apex size is not evident.

Table 4-1. Voltage used during electrochemical etching of tungsten tips

Tip No.	Voltage (V)	Aspect ratio	Apex radius (μm)
1	12	0.5	10
2	12	0.65	4
3	14	0.37	25
4	14	0.45	8

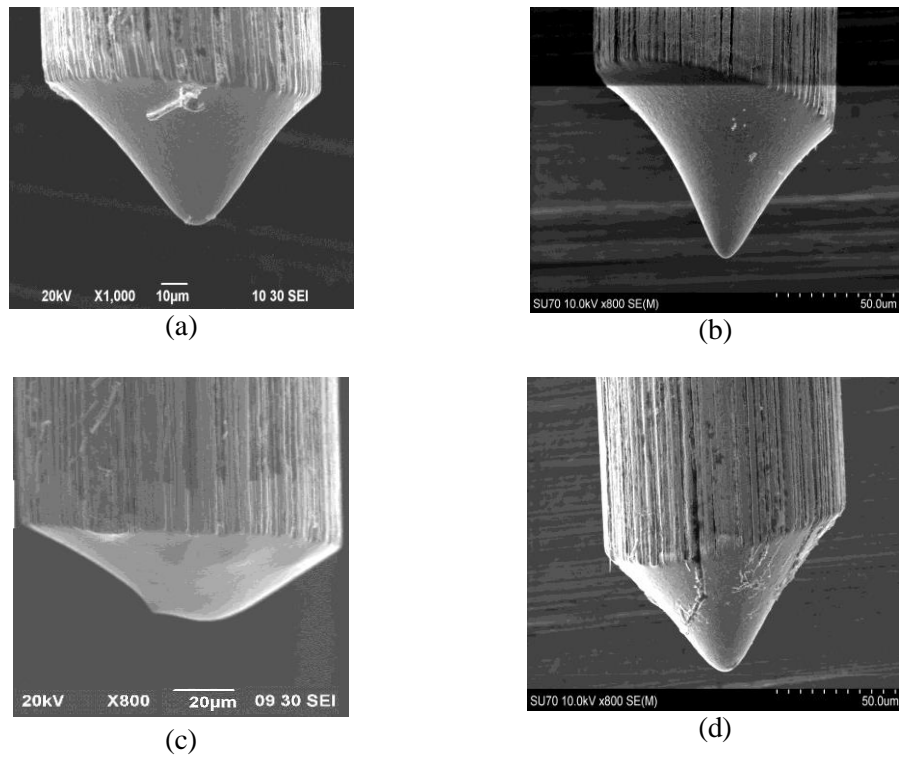


Figure 4-12 SEM micrographs of fabricated tips (a) 1, (b) 2, (c) 3 and (d) 4.

4.5 Conclusion

This chapter has presented the design of a coaxial resonator transmission line-based NFMM that operates in non-contact mode by using a quartz tuning fork-based distance following feedback system. The microwave probe and quartz tuning fork have been simulated using a combination of circuit and

electromagnetic simulation and simulation results show good agreement with measurements. It has been found that the contact between the probe tip and quartz tuning fork has significant implications on both the microwave probe response and the height control system performance. For instance, at contact, the quality factor of the microwave probe is degraded by approximately 30% and the coupling of the microwave resonator to the source is changed. Critical coupling between the resonator and source can be adjusted by reducing the gap between the resonator and feed line. Effects of the tip-fork contact on the quartz tuning fork's response include the degradation in the amplitude of vibration at resonance and a shift of the resonance frequency. It has been found that the shift in the resonance peak and the voltage attenuation at resonance can be reduced by proper adjustment of the relative position between the probe tip and tuning fork.

Additionally, the quartz tuning fork-based height control system successfully mapped the surface topography of a testing sample consisting of a $\text{Ba}_{0.5}\text{Sr}_{0.5}\text{TiO}_3$ trace on alumina substrate. Measured topography is in very good agreement with a commercial profiler. It is worth noting that this quartz tuning fork-based height control system is low-cost compared to a similar commercial system such as the MadPLL (Mad City Labs) whose current price is on the order of fifteen thousand dollars [90]. Furthermore, advantages of this system over a commercial profiler are that it is non-contact, non-destructive and not only line profiles but also images of the surface topography can be obtained.

CHAPTER 5 : CAPABILITIES OF THE DR-BASED NFMM AND THE COAXIAL TRANSMISSION LINE RESONATOR-BASED NFMM

5.1 Note to Reader

Portions of this chapter, including figures have been previously published in [91], and have been reproduced with permission from the European Microwave Association. See Appendix A-4 for permission.

5.2 Introduction

So far, two NFMM with different Q , tip size and one of them operating in conjunction with a tuning-fork distance following feedback system have been presented in the previous chapters. However, the influence of these parameters on the performance of these NFMM designs has not been discussed yet. In this chapter, the imaging capability and the ability to differentiate materials with different electromagnetic properties of the DR-based NFMM and coaxial transmission line resonator-based NFMM are studied. Material differentiation is influenced by the Q of the resonant probe and the strength of the evanescent fields interacting with the MUT [6, 71]. The higher the Q and the stronger the fields in the sample, the higher the material differentiation capability or sensitivity of the NFMM. The strength of these fields can be enhanced by increasing the tip apex size and reducing the tip-sample distance [71]. In this chapter, material differentiation capability of the NFMM designs is investigated under conditions that affect the strength of the fields in the MUT, such as the probe tip being immersed in the MUT (liquid) and

the MUT being coated by insulating films. Additionally, the imaging capability and spatial resolution of the NFMM designs is verified under the same conditions using a set of known patterns.

5.3 Material Differentiation

5.3.1 Differentiation of Bulk Dielectric Materials

The ability of the microwave microscope to differentiate materials with different properties is studied using the DR-based NFMM and the transmission line coaxial transmission line resonator-based NFMM. The sensitivity analysis is carried out by measuring the resonance properties of the microwave probe F_r and Q as a function of d for a set of standard insulating bulk samples (fused silica, alumina, sapphire, and LaAlO_3) [91]. Measured F_r and Q plots for the DR-based resonator using tip with apex radius of 25 μm are shown in Figure 5-1 (a) and (b), respectively. These plots reveal that both F_r and Q are affected by the presence of the bulk samples and that the drop in these properties increases with the permittivity of the sample and decreases with the tip-sample distance d . This behavior is explained by the fact that the coupling capacitance between the tip and the sample C_c increases as d decreases which results in the reduction of F_r . Also, it can be noted that variations as small as $\Delta\epsilon'_r = 1.75$ are successfully resolved with the probe in the range $9.8 \leq \epsilon'_r \leq 11.58$.

Measured F_r and Q vs. d plots for the coaxial transmission line resonator-based probe using a tip with apex radius of 10 μm are shown in Figure 5-2 (a) and (b), respectively. It is observed that this probe is also sensitive to the standard insulating bulk samples. However, the probe is not able to resolve alumina from sapphire ($\Delta\epsilon'_r = 1.75$) which can be explained by the low Q of the probe ($Q=55$ for $\text{MUT}=\text{air}$). In order to improve the Q of the probe, and therefore the sensitivity, the quartz tuning fork can be removed from contact with the probe tip (see sub-section 4.3). It is worth noting that a consequence of removing the quartz tuning fork from the probe will result in an NFMM that is unable to perform an xy scanning at

a constant tip-sample distance since the contact with the sample cannot be established. Table 5-1 summarizes the minimum resolvable difference in dielectric constant obtained with the DR-based and coaxial transmission line resonator-based NFMM designs.

Table 5-1. $\Delta\epsilon'_r$ of the DR-based and coaxial transmission line resonator-based NFMM designs

NFMM design ($0\ \mu\text{m} < d < 14\ \mu\text{m}$) ($9.8 \leq \epsilon'_r \leq 11.58$)	$\Delta\epsilon'_r$	Tip apex radius (μm)	Q
DR-based NFMM	1.75	25	982
Coaxial transmission lines-based NFMM	<1.75	10	55

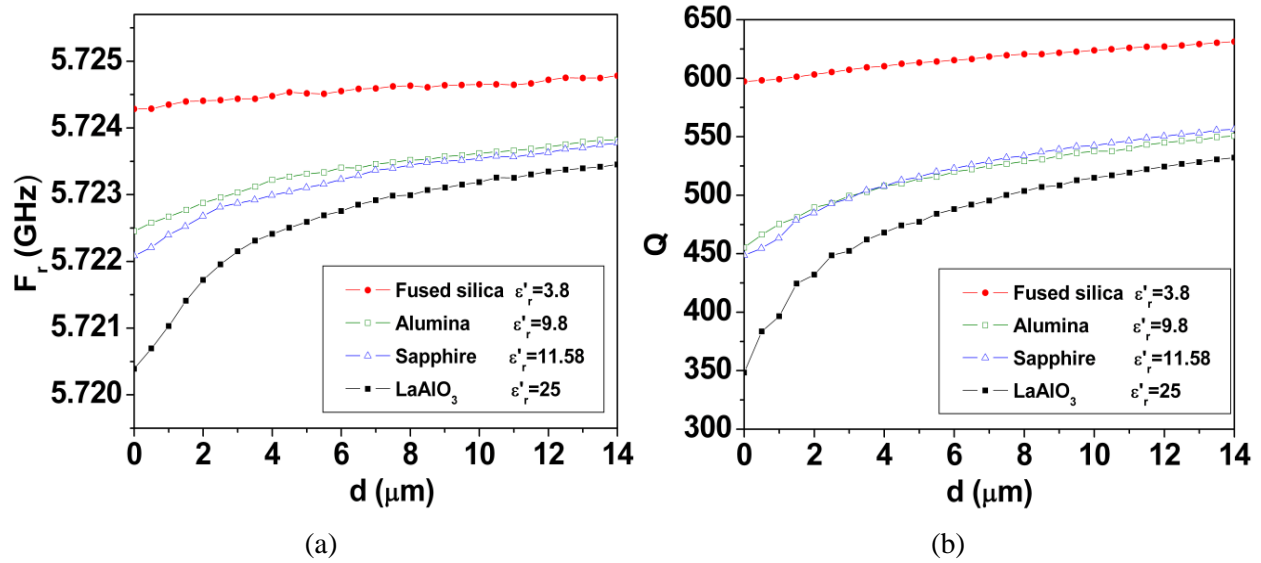


Figure 5-1 (a) F_r and (b) Q of the DR-based microwave probe using tip of apex radius of $25\ \mu\text{m}$ for different insulating bulk samples.

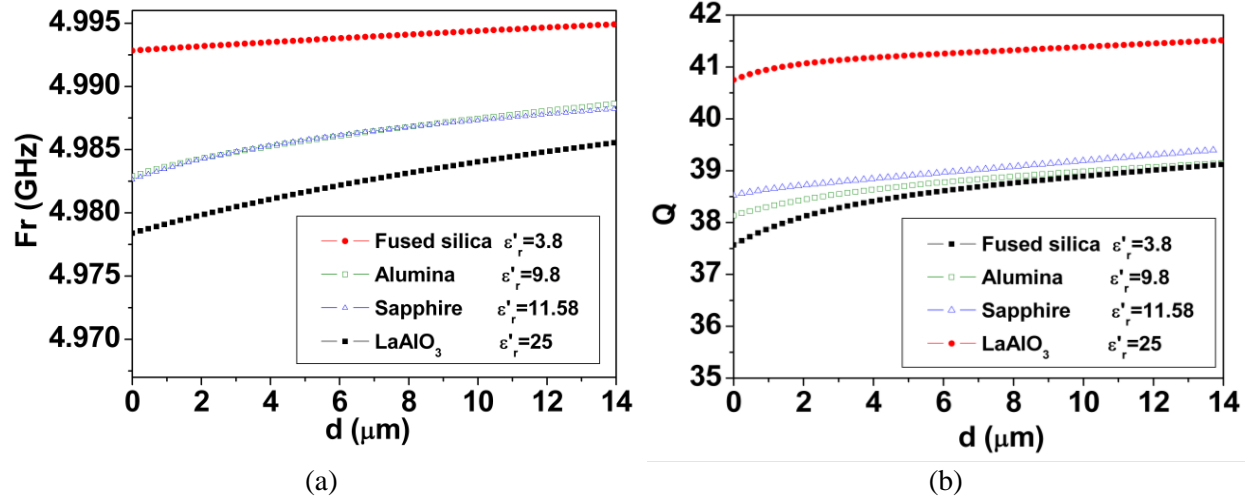


Figure 5-2 (a) F_r and (b) Q of the coaxial transmission line resonator--based microwave probe using tip of apex radius of 10 μm for different insulating bulk samples.

5.3.2 Differentiation of Liquids

It is of interest to study the performance of the DR-based NFMM (design with better Q and $\Delta\epsilon'_r$) using liquids with a wide range of permittivity for two reasons. Firstly, liquids facilitate the study of the differentiation capability of the NFMM operating under in-situ conditions (tip is immersed in the liquid). Secondly, so far, characterization of liquids using NFMM has been concentrated only on the study of the resonant properties of the microwave probe for different NaCl concentrations (high permittivity and high loss) [62, 65]; however capabilities of NFMM to differentiate liquids with low-loss and low-dielectric constant and modeling of the tip-liquid interaction have not been explored yet. The sensitivity analysis is also carried out by measuring the resonance properties of the microwave probe F_r and Q as a function of d for liquids with a wide range of permittivity. The liquids used in this work along with their permittivities are listed in Table 5-2. The permittivity of each liquid was measured using an Agilent 85070B dielectric probe at 5.72 GHz and at room temperature. Materials with loss tangent greater than approximately 0.49 will be categorized as lossy materials. Thus, mineral, olive, corn and castor oil will be referred as low loss liquids while acetone and the isopropyl alcohols are considered to be lossy liquids.

In order to measure the resonant properties of the probe for the different liquids, each liquid was deposited onto an aluminum sample holder designed with an orifice 6 mm wide and 1 mm deep, which preserves the volume of the liquid and prevents it from spreading on the holder. A micropipette was used to deposit a consistent amount of liquid onto the sample holder. All of the measurements were performed at 16 °C in a temperature-controlled room. The aluminum plate containing the liquid was placed at a distance **d** from the tungsten tip, which is varied during measurements through the computer controlled stages combination. For the measurements, Q and F_r were recorded as the distance **d** was varied from 0.4 mm to -0.2 mm. The probe tip makes contact with the liquid at **d** = 0mm, therefore the probe tip is submerged in liquid for negative values of **d**.

Table 5.2. Permittivity and loss tangent of liquids used (measured a 5.72 GHz using the 8570B Agilent Probe)

Liquid	Dielectric constant		Tan δ	
	ϵ'_r	ϵ''_r		
Mineral Oil	2.34	0.01	0.004	<i>Low-loss</i>
Olive Oil	2.68	0.17	0.06	<i>Low-loss</i>
Corn Oil	2.72	0.18	0.06	<i>Low-loss</i>
Castor Oil	2.93	0.24	0.08	<i>Low-loss</i>
Acetone	32.25	15.92	0.49	<i>Lossy</i>
Isopropyl Alcohol 50%	22.95	20.60	0.89	<i>Lossy</i>
Isopropyl Alcohol 70%	12.16	11.71	0.96	<i>Lossy</i>

To analyze the experimental data, the lumped-element circuit model of the probe and sample in the vicinity of resonance presented in Figure 3-4(a) is used. The tip-liquid interaction for the non-contact and immersed case is shown in Figure 5-3. In the non-contact case, the coupling between the tip and the sample is represented by C_c , which increases as the tip approaches the liquid. The properties of the MUT are modeled by C_s and R_s which are related to ϵ'_r and ϵ''_r , respectively. When the tip is submerged in the liquid, C_s and R_s not only depend on the permittivity but also on the proximity of the tip to the bottom of the metal sample holder.

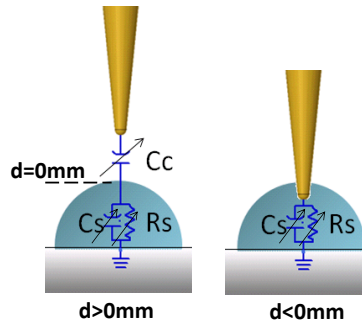


Figure 5-3 Lumped-element circuit model of the tip-liquid interaction for $d > 0$ mm (non-contact), and for $d < 0$ mm (probe tip submerged in the liquid).

Figure 5-4 (a) and (b) show the measurements of F_r and Q as a function of distance d for the low loss liquids, respectively. It can be observed that as the probe tip approaches the liquid, both F_r and Q decrease and the variation is proportional to the value of the liquid permittivity. Additionally, it can be seen that once the probe tip is immersed into the liquid, Q and F_r can be more clearly distinguished between the four samples compared to the non-contact condition; and that variations as small as $\Delta\epsilon'_r = 0.04$ are successfully resolved in the range $2.34 \leq \epsilon'_r \leq 2.72$. The Q and F_r behavior might be explained through the lumped-element circuit models of Figure 3-4(a) and Figure 5-3. For low-loss liquids, R_s can be assumed to be high since low values in ϵ''_r result in low values of dielectric conductivity $\sigma = \omega\epsilon''_r$. In the non-contact case, F_r and Q decrease with d as C_c increases. The presence of C_c masks variations in C_s and R_s and thus results in relatively small variations in the resonance frequency and Q among the four materials. When the tip is immersed into the liquid, there is no C_c capacitance and the decrement in Q and

F_r is only determined by the C_s , R_s and d , which explains the enhancement in the sensitivity of the probe when it is fully immersed in the liquid. Table 5-3 summarizes the minimum resolvable difference of the DR-based NFMM for non-contact measurement of bulk samples with the sensitivity of the DR-based NFMM for the tip immersed in low-loss liquids.

Table 5-3. $\Delta\epsilon'_r$ of the DR-based NFMM

NFMM design	$\Delta\epsilon'_r$	Tip apex radius (μm)	Q
$0 \mu\text{m} < d < 14 \mu\text{m}$ $9.8 \leq \epsilon'_r \leq 11.58$ (Bulk)	1.75	25	982
$d < 0 \mu\text{m}$ $2.34 \leq \epsilon'_r \leq 2.72$ (Liquids)	0.04	25	982

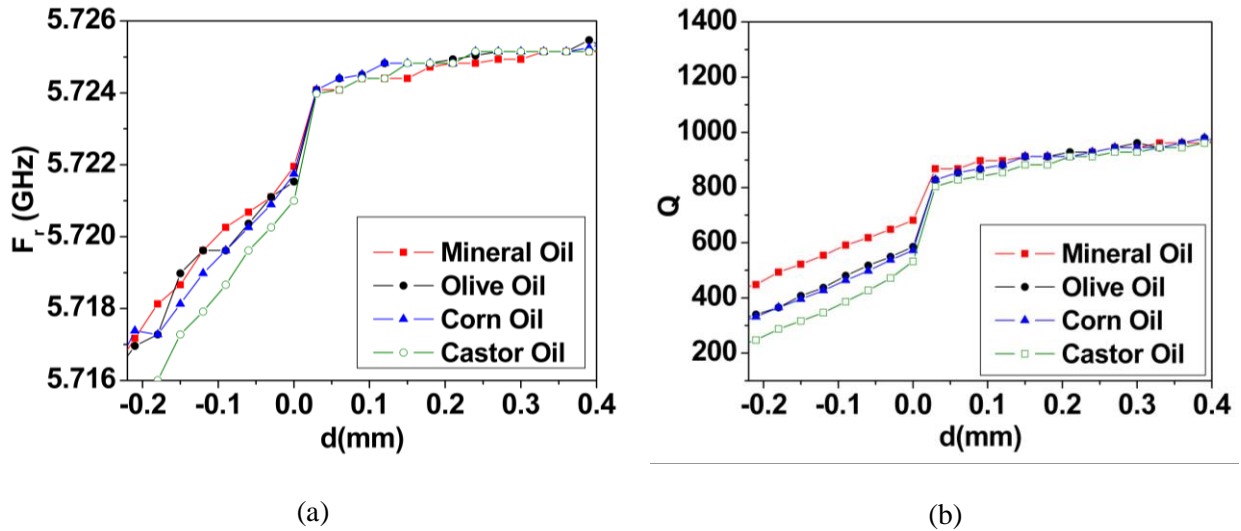


Figure 5-4 (a) Measured F_r vs. d plot for different low loss liquids. (b) Measured Q vs. d plot for different low loss liquids.

Figure 5-5 (a) and (b) present the measurements of F_r and Q as a function of the distance d for lossy liquids. The lumped-element circuit models shown in Figure 3-4(a) and Figure 5-3 are also used to describe these results. From Table 5-2, it can be seen that the permittivity of the lossy liquids is higher

than that of the low loss liquids; therefore, compared to the previous section, lower values for R_s and higher values of C_s need to be considered. For $d > 0$ mm, the resonant frequency and quality factor decrease as C_s increases and R_s decreases, respectively. For $d < 0$ mm, F_r remains almost constant with d because of the low values of R_s . The quality factor increases as C_s increases and R_s decreases as a consequence of the increment in the permittivity and/or reduction of d . It can be observed that differences in Q between the samples are more clearly resolved when the tip is immersed in the liquid than in non-contact case. This enhancement in the sensitivity in Q for $d < 0$ mm was also observed for low loss liquids and it can be caused by the absence of C_c .

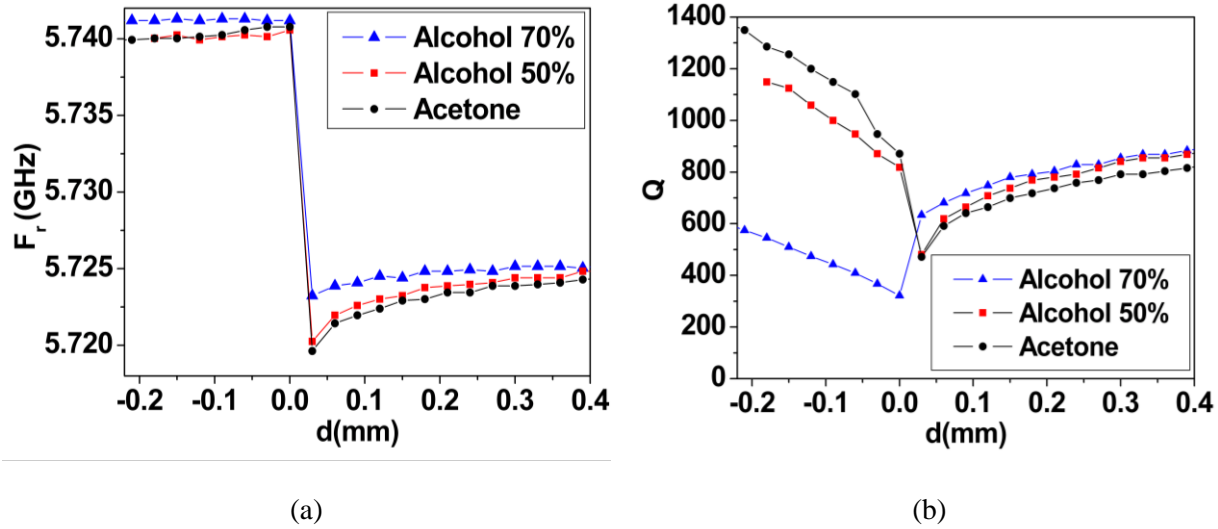


Figure 5-5 (a) Measured F_r vs. d plot for different lossy liquids. (b) Measured Q vs. d plot for different lossy liquids.

Simulations of the lumped-element circuit model of the probe and liquid shown in Figure 3-4(a) and Figure 5-3 were carried out in ADS and confirm the measurements for low-loss and lossy liquids. Figure 5-6 (a) and (b) show the simulated F_r and Q of the probe as a function of C_s (ϵ'_r) for the tip interacting with a low-loss liquid in non-contact and in-contact operation, respectively. Since ϵ'_r and ϵ''_r are low for low-loss liquids C_s is assumed to be low ($30 \text{ fF} < C_s < 60 \text{ fF}$) and R_s high ($R_s = 3 \text{ K}\Omega$). It is

observed that in contact and non-contact operation both F_r and Q decrease as C_s increases. Figure 5-6 (c) and (d) shows that for the tip interacting in non-contact operation with lossy liquids, F_r and Q decrease as C_s increases. However, when the tip is immersed in the lossy liquid, F_r no longer changes with C_s and Q increases as C_s increases. For lossy liquids ϵ_r' and ϵ_r'' are high; therefore, R_s is assumed to be low ($R_s = 15 \Omega$) and C_s high ($1000 \text{ fF} < C_s < 5000 \text{ fF}$).

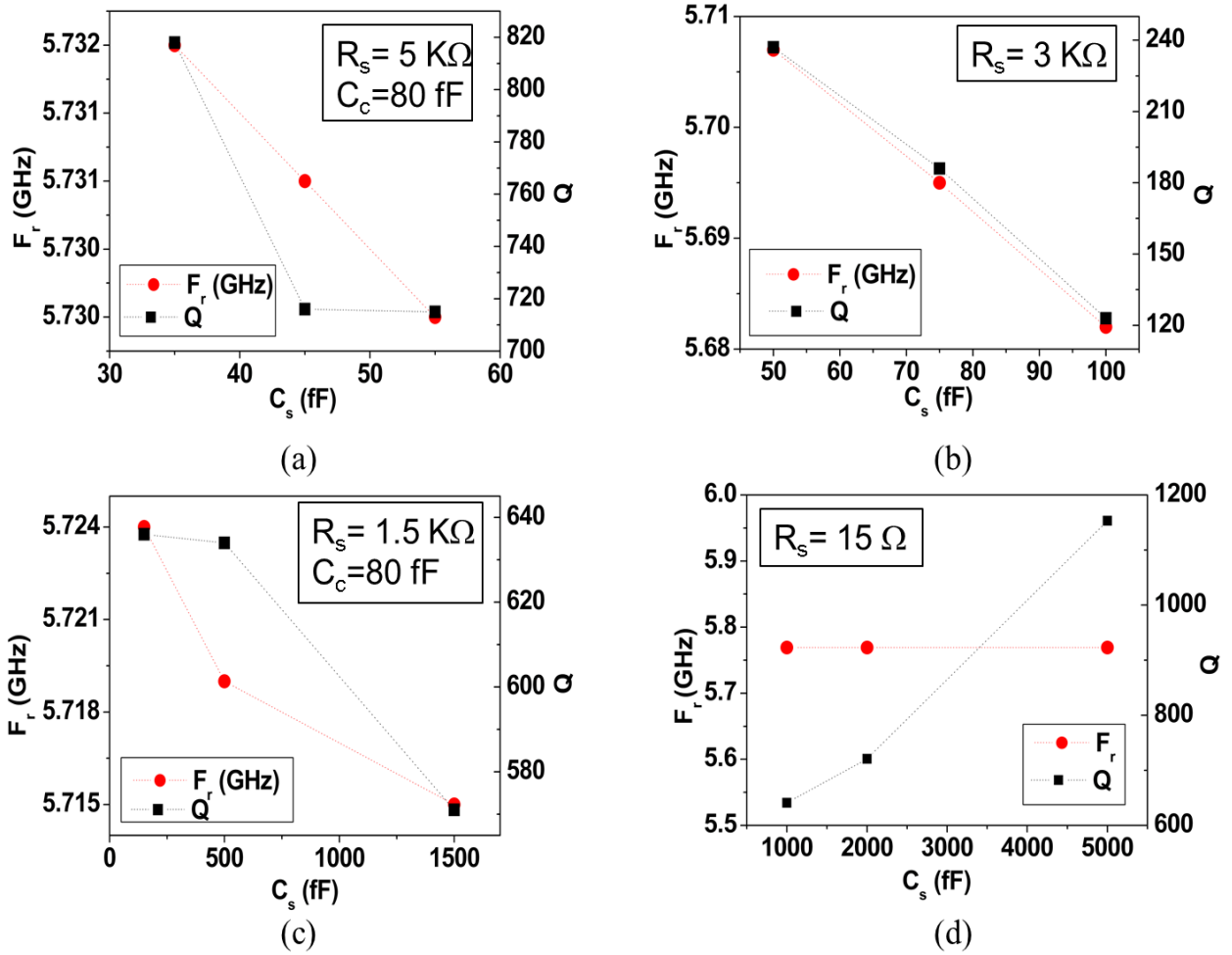


Figure 5-6 Simulated F_r (a) and Q (b) of the lumped-element circuit vs. C_s for low-loss liquids. Simulated F_r (c) and Q (d) of the lumped-element circuit vs. C_s for lossy liquids

5.3.3 Differentiation and Detection of Subsurface Materials

One of the objectives of this dissertation is the imaging and detection of subsurface materials and structures. The first step to accomplish this goal is to explore the subsurface imaging and material differentiation capabilities of NFMM. In this case, the coaxial transmission line resonator-based NFMM is used since it allows the scanning over the sample at a constant height regardless the conductivity of the sample. There are several sample parameters of interest that can be considered in this study such as the number and permittivity of the coating layers, thickness of each layer and permittivity of the material being coated, etc. This work considers the tip-sample distance to be constant and the number of coating layers to be one. Thus, in this section, the ability of the coaxial transmission line resonator-based NFMM to differentiate buried dielectrics using a tip with apex radius of 10 μm is presented.

Figure 5-7 (a) presents a schematic of an insulating substrate with permittivity ϵ_{rs} ($3.8 < \epsilon_{rs} < 25$) coated with a layer of thickness Z_f ($5\mu\text{m} < Z_f < 30\mu\text{m}$) and permittivity ϵ_{rf} ($2.95 < \epsilon_{rf} < 30$), along with the predicted NFMM probe resonant frequency (Figure 5-7 (b)-Figure 5-7(d)) obtained with the co-simulation approach described above. As illustrated in the plots it is possible to differentiate all of the substrates coated by insulating films whose thickness varies within 5 μm and 30 μm . Sensitivity of F_r to changes in ϵ_{st} decreases as the dielectric constant and thickness of the coating layer increase. For example, ΔF_r for substrates with permittivity of $\epsilon_{rs} = 9.8$ and $\epsilon_{rs} = 25$ is reduced from 2 MHz to 1.6 MHz when the permittivity of the 30 μm coating layer increases from $\epsilon_{rf} = 2.5$ to $\epsilon_{rf} = 30$. Another observation from the plots is that for any substrate, F_r decreases as ϵ_{rf} increases, which is explained through a lumped element circuit model of the interaction between the probe tip and sample. The tip is coupled to the substrate through two capacitors connected in series, C_1 and C_2 , as shown in Figure 5-7(a); the first capacitor couples the tip to the coating layer and the permittivity is that of air, and the second capacitor couples the coating layer to the substrate. The permittivity of the second capacitor is ϵ_{rf} . Thus, for a constant C_1 , an increase in ϵ_{rf} increases C_2 and decreases F_r .

In order to confirm experimentally that the NFMM is able to characterize and differentiate several buried bulk dielectrics, F_r vs. d measurements of bulk substrates of fused silica, alumina, sapphire and LaAlO_3 are carried out with a 5 μm thick parylene-C coating layer. F_r vs. d measurements for the samples without a coating layer were presented and discussed in Section 5.1 (see Figure 5-2 (a)). Figure 5-8 (a) shows measured F_r for the samples coated with a 5 μm thick parylene layer.

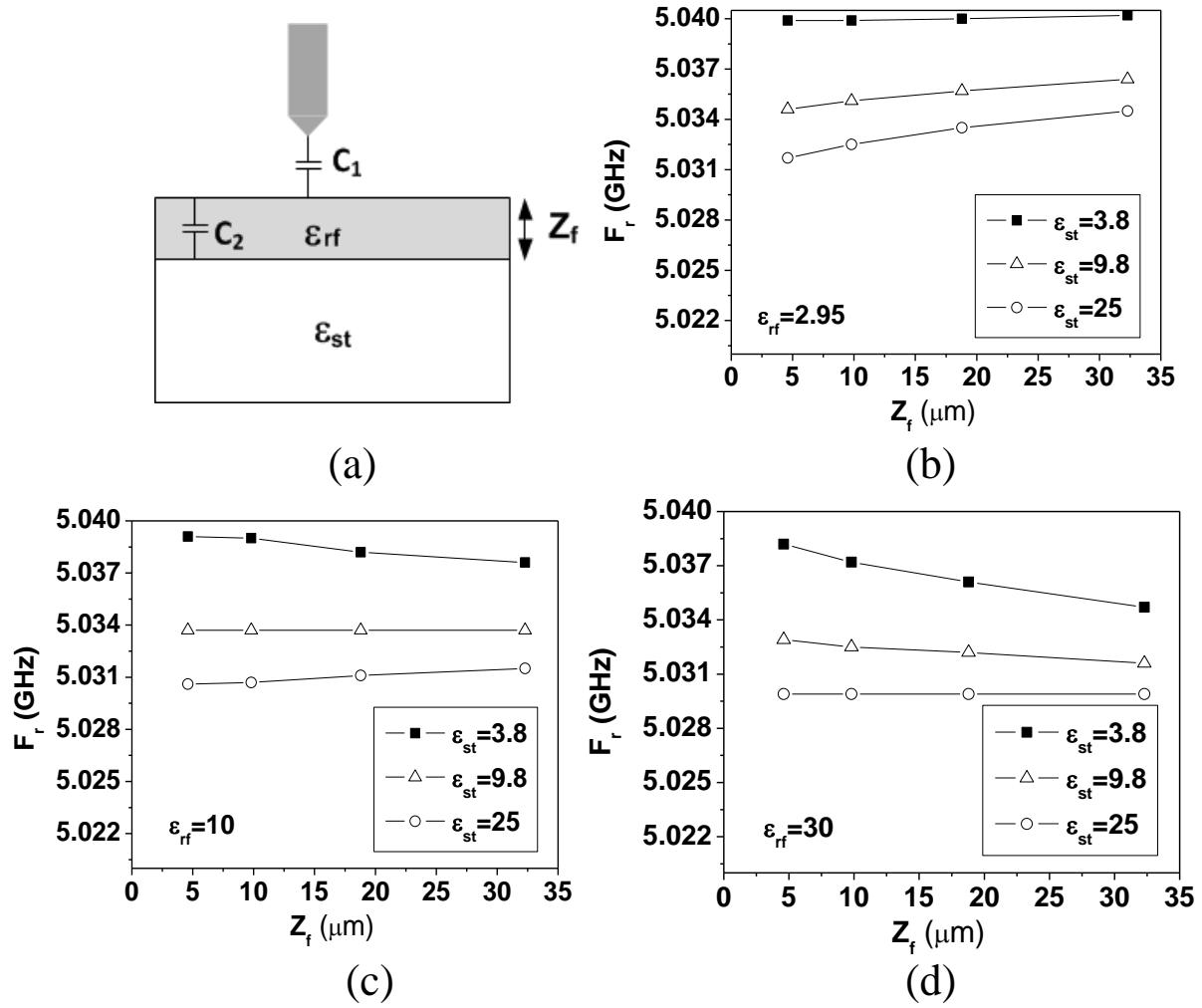


Figure 5-7 (a) Schematic of the simulated sample. Simulated resonance frequency plots for coating layer with permittivity of (b) $\epsilon_{rf}=2.95$ (c) $\epsilon_{rf}=10$ and (d) $\epsilon_{rf}=30$.

It can be observed that the NFMM is able to resolve differences between the buried substrates and that there is an increase in F_r due to the presence of the coating layer compared to values for bare

substrates. F_r for sapphire resulted in a larger shift in frequency than that for LaAlO_3 which is explained by the fact that the parylene-C layer thickness on different samples varies somewhat depending on the location of the sample in the PDS chamber. Particularly, the parylene-C layer thickness on sapphire is about 200 nm thicker than that on LaAlO_3 . The frequency shift (ΔF_r) as a function of the substrate permittivity can be clearly seen in the inset in Figure 5-8(b).

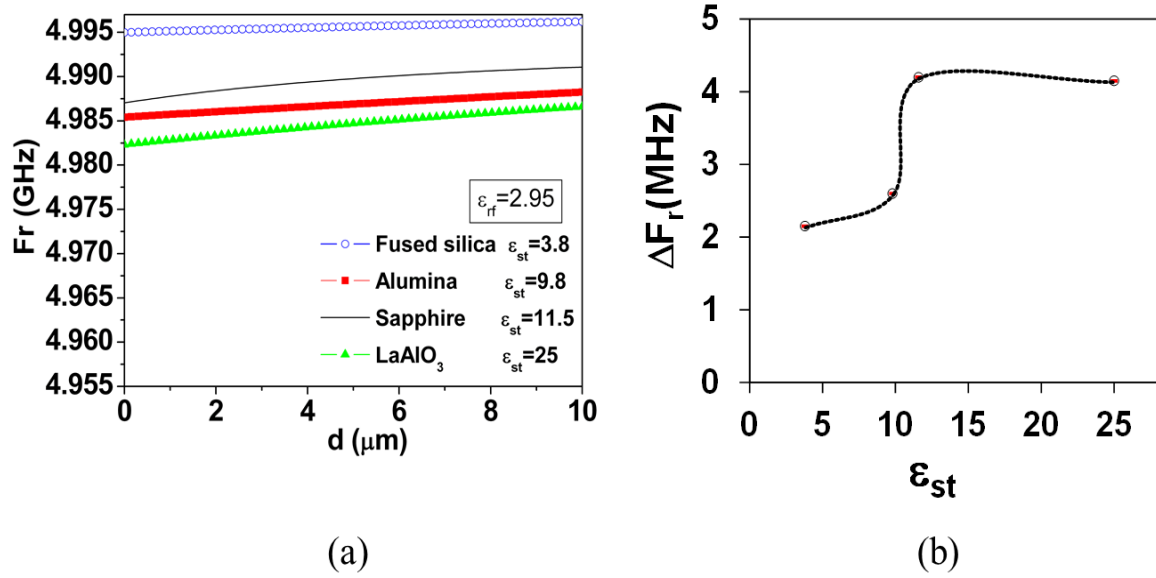


Figure 5-8 Measured F_r vs. tip-sample distance for different bulk substrates coated with a 5 μm thick parylene-C layer. (b) Measured frequency shift (ΔF_r) between coated and bare substrates as a function of the substrate permittivity ϵ_{st} .

5.4 Imaging Capability

Imaging capability refers to the ability of the NFMM to image materials features and is can be quantified by the spatial resolution. As discussed in Chapter 2, spatial resolution in an NFMM is influenced by the tip geometry and the tip-sample distance rather than the wavelength at the operation frequency. An approach used to verify the spatial resolution of the NFMM is to scan a set of patterns with known lateral dimensions (smaller than the tip size). The resulting full width at half maximum (FWHM) of the narrowest trace will determine the spatial resolution [92].

The spatial resolution of the DR-based NFMM (tip with apex radius of 25 μm) is verified by scanning the GaAs MMIC phase shifter shown in Figure 5-9(a). At every point of the 500 μm x 500 μm scan, Q is recorded and subtracted from the Q for the probe at $d = 10$ mm. The phase shifter was fabricated by Qorvo (formerly TriQuint Semiconductor) using the TQPED process. The layout shown in Figure 5-9(a) contains ground-signal-ground pads, microstrip lines, an MIM capacitor and a section of a spiral inductor. The microstrip line is constructed using 4 μm thick Metal 2 layer, the pads are created using Metal 2 and passivation via, the MIM capacitor is constructed using 0.5 μm thick Metal 0 layer and MIM layer. The spiral inductor is constructed using stacked 2 μm thick Metal 1 and Metal 2 structures. The MMIC phase shifter, excepting the pads, is coated with a 0.8 μm thick SiN_x passivation layer. From this layout, the narrowest trace is a 10 μm wide microstrip line which is used to verify the spatial resolution of the microscope. In order to perform the xy scan, the contact point with the gold pads is established by monitoring the shift in frequency that occurs at soft contact (see chapter 3); then the sample is lowered by 5 μm to start the scan.

Figure 5-9 shows the top view (b) and 3D view (c) of the measured ΔQ plot for the 500 μm x 500 μm scan of the MMIC phase shifter. It can be seen that the metallic features coated by the 0.8 μm thick passivation layer can be distinguished from the GaAs substrate and that the 68 μm wide microstrip line as well as the ground pads are clearly distinguishable in the plot. Moreover, the 10 μm wide ($\approx \lambda/5000$) microstrip line section is clearly resolved. The spatial resolution is verified by determining the FWHM of the 10 μm wide microstrip line. Figure 5-10 shows a line profile along the 10 μm microstrip line from which it can be seen that the half maximum occurs at $\Delta Q = 700$ and that the spatial resolution is 50 μm . As expected, the spatial resolution is set by the tip apex diameter (50 μm).

It is of interest to verify the imaging capability and spatial resolution of the DR-based probe when it is operated under in-situ conditions. In the previous section, it was shown that once the probe tip is in the liquid, the sensitivity of the probe is improved. The spatial resolution of the probe was verified by scanning the MMIC detector shown in Figure 5-11. On top of the detector, a mineral oil layer 30 μm thick

was deposited. The scan area is $300\text{ }\mu\text{m} \times 300\text{ }\mu\text{m}$ and consists of gold microstrip lines and a ground pad on a 0.1 mm thick GaAs substrate. The smallest feature size is a microstrip line that is $10\text{ }\mu\text{m}$ wide.

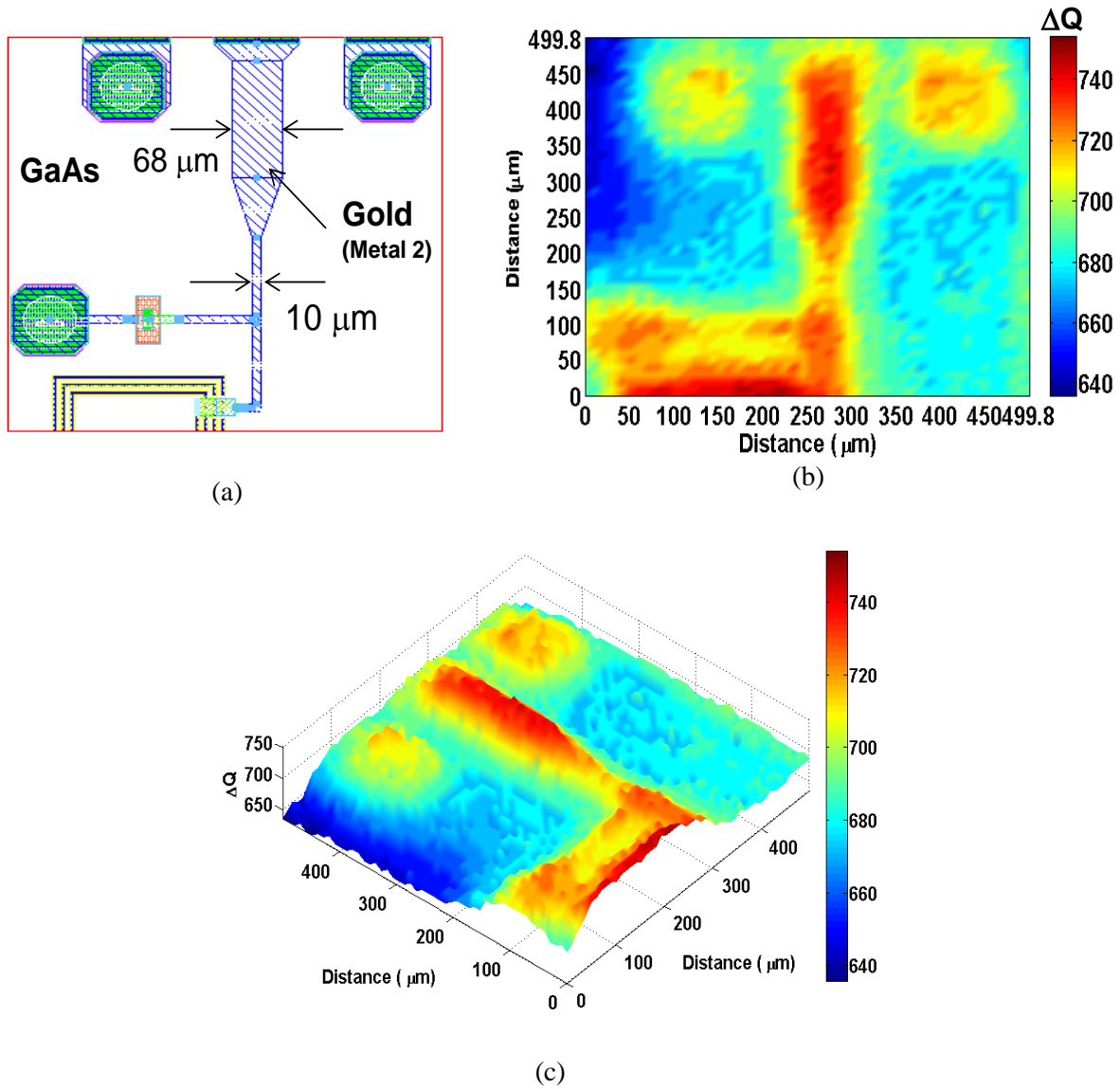


Figure 5-9 (a) MMIC phase shifter scan area. ΔQ measured data for the $500\text{ }\mu\text{m} \times 500\text{ }\mu\text{m}$ scan of the MMIC phase shifter (b) top view and (c) 3D view.

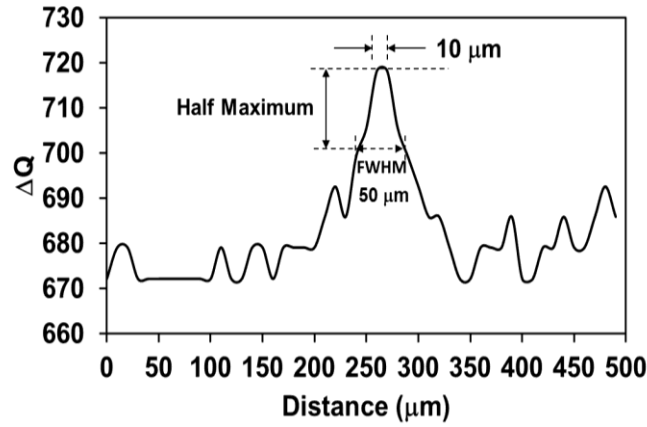


Figure 5-10 Line profile along the 10 μm wide microstrip line.

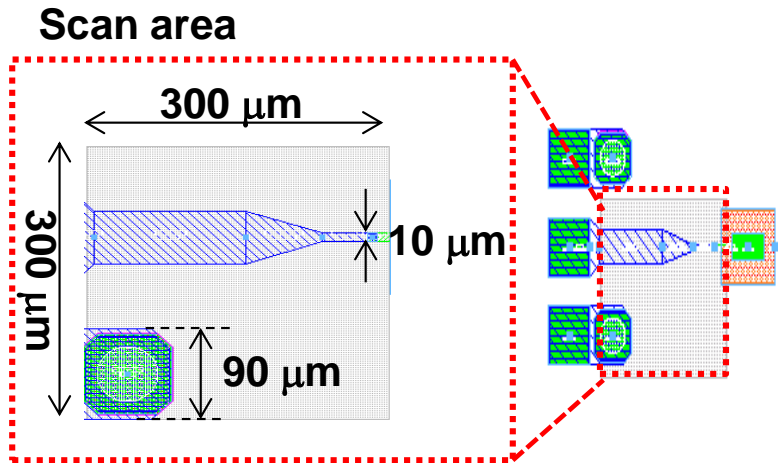


Figure 5-11 MMIC detector and scan area.

Figure 5-12 (b) shows the measured ΔQ plot for the 300 μm x 300 μm scan of the MMIC detector. The reference value in ΔQ is the quality factor of the probe in air at $d = 1$ mm. In order to perform non-destructive imaging of ΔQ , the contact point with the gold pads is established by monitoring the shift in frequency that occurs at soft contact (see Section 3.4); then the sample is lowered by 10 μm to start the scan. The microstrip lines as well as the ground pad are distinguishable in the plot, including the 10 μm microstrip line. For comparison purposes, the MMIC detector without the mineral oil layer was also scanned. As can be seen in Figure 5-13 (b), all the features are also distinguishable; however the

sensitivity of the probe is diminished. The spatial resolution of the NFMM for non-contact and under in-situ conditions determined from the FWHM of the 10 μm wide microstrip line are found to be 70 μm and 80 μm , respectively. This result demonstrates that although the sensitivity improves under in-situ conditions, the spatial resolution is not significantly degraded. Figure 5-14 shows the line profiles along the 10 μm microstrip line obtained with the tip in air and immersed in mineral oil.

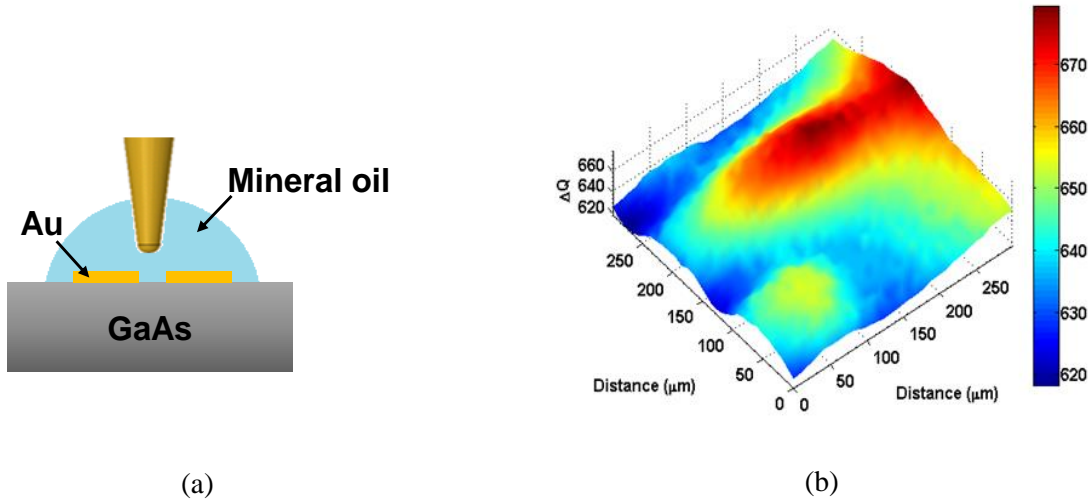


Figure 5-12 (a) Illustration of the tip, MMIC detector and mineral oil seen from the side. (b) ΔQ measured data of the MMIC detector when the tip is in the presence of mineral oil.

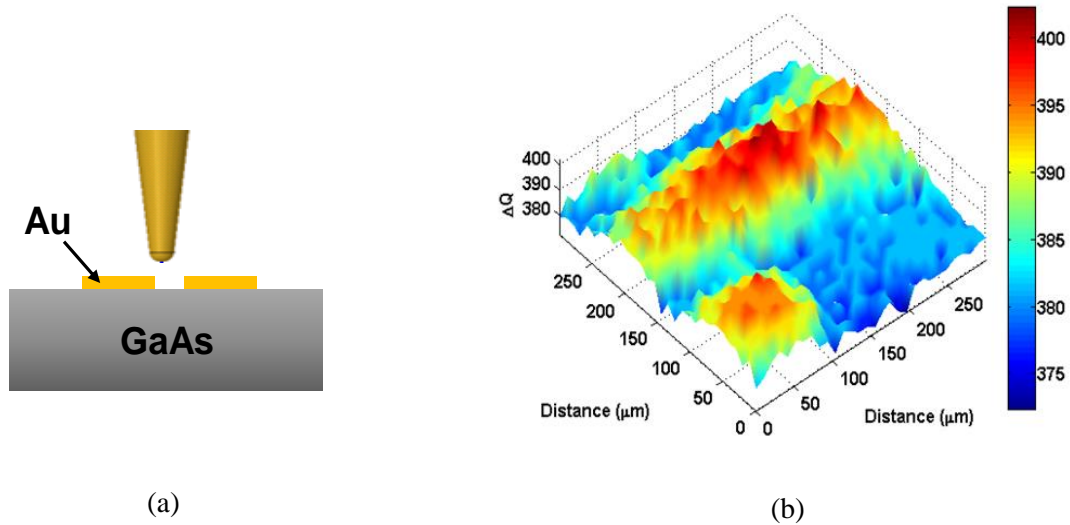


Figure 5-13 (a) Illustration of the tip and MMIC detector seen from the side. (b) ΔQ measured data of the MMIC detector when the tip is in air (no mineral oil on the MMIC detector).

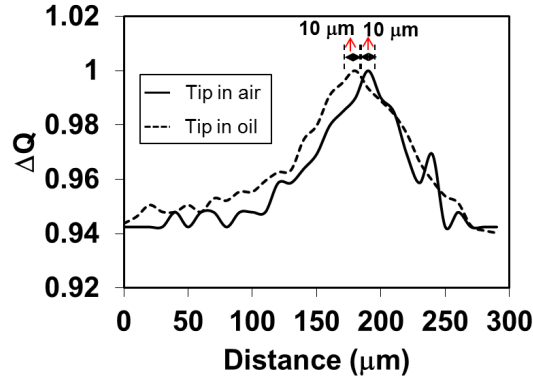


Figure 5-14 Line profile along the 10 μm wide microstrip line for the tip in air and oil.

The enhancement of the sensitivity of the probe tip under in-situ conditions can also be understood by looking at the simulated electric fields of the tip and liquid interaction shown in Figure 5-15. Since the fields exerted from the tip are evanescent in nature, the simulation of the tip-sample interaction can be carried out in an electrostatic simulator such as Ansys Maxwell or Comsol Multiphysics. In this work the simulation is performed in Ansys Maxwell; the tip has an apex radius of 25 μm and the liquid is mineral oil. From the plots, it can be seen that the magnitude of the electric fields is greater and extends wider and deeper in the liquid when the tip is immersed in the liquid than in the non-contact case, which results in an improvement of the sensitivity but a degradation of the resolution.

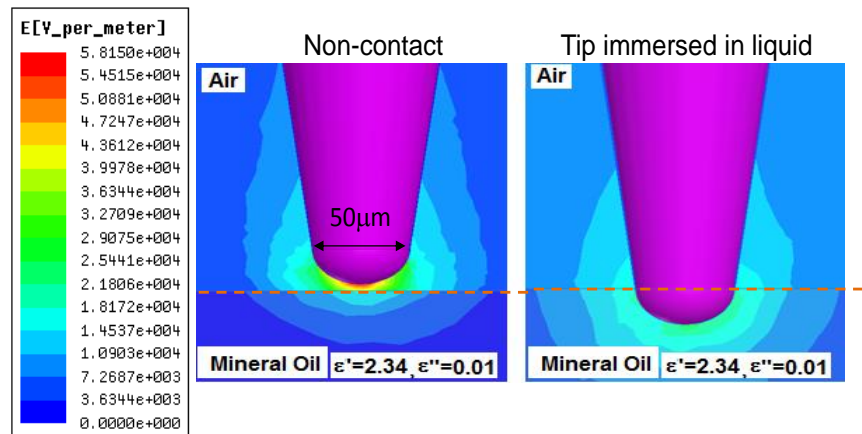


Figure 5-15 Electric field distribution of the tip-mineral oil interaction for non-contact operation (left) and tip immersed in mineral oil (right).

- Imaging of Metallic Subsurface Features

In order to verify the spatial resolution and the ability of the NFMM to distinguish sub-surface metallic and dielectric features, a test sample consisting of a 500 nm thick gold trace coated with a 10 μm thick parylene-C layer is fabricated. The gold trace has a width of 50 μm and was deposited onto a glass substrate using E-beam evaporation. The sample is scanned using tips with apex radii of 4 μm and 10 μm , which were shaped by the electrochemical process described in section 4.4. SEM micrographs of the tips are shown in Figure 4.14 (a) and (b).

The scan across the gold on the test sample was carried out over an area of 175 μm x 175 μm in steps of 2 μm at a constant tip-sample distance of 100 nm. The 50 μm wide gold trace can be clearly distinguished from the glass in the F_r and Q images presented in Figure 5-16. Both F_r and Q decrease for the gold region as a result of the increase in the capacitance and losses; this result is consistent with data presented in [6] which is explained by a redistribution of charges around the tip due to the presence of the metal and a resulting degradation of Q .

The measurements acquired using the tip with an apex radius of 10 μm exhibit more sensitivity than those using the tip of 4 μm . This is explained by the fact that the electric fields extend deeper and wider into the coating layer as the tip apex radius increases, resulting in an increase in the sensitivity of the NFMM. However, wider extension of electric fields in the sample is translated into a degradation of the lateral spatial resolution. This effect can be better seen through the line profiles across the sample shown in Figure 5-17. These line profiles are the average of the profiles acquired along the x direction during the xy scan. Since the maximum values of F_r and Q using the 10 μm and 4 μm tips are different, F_r and Q are normalized to each local maximum. It is noted that the increase in the sensitivity when using the larger tip is about 2 times higher in Q and 1.6 times in F_r measurement. The tilting in the sample is about 1.5 μm along x and it was corrected during post processing.

The electric field distributions obtained from HFSS simulations of the parylene-C/gold/glass sample support the experimental results presented above. In these simulations the parylene-C layer is 30

μm thick and the tip-sample distance is 100 nm. Figure 5-18 shows the electric field distribution for apex radii of (a) 10 μm and (b) 25 μm . In each case the fields decay symmetrically below the tip and extend through the parylene-C layer reaching the gold trace. However, stronger field interaction zones are concentrated within a region approximately equal to the tip size which means that higher spatial resolution can be achieved using the tip with a smaller apex.

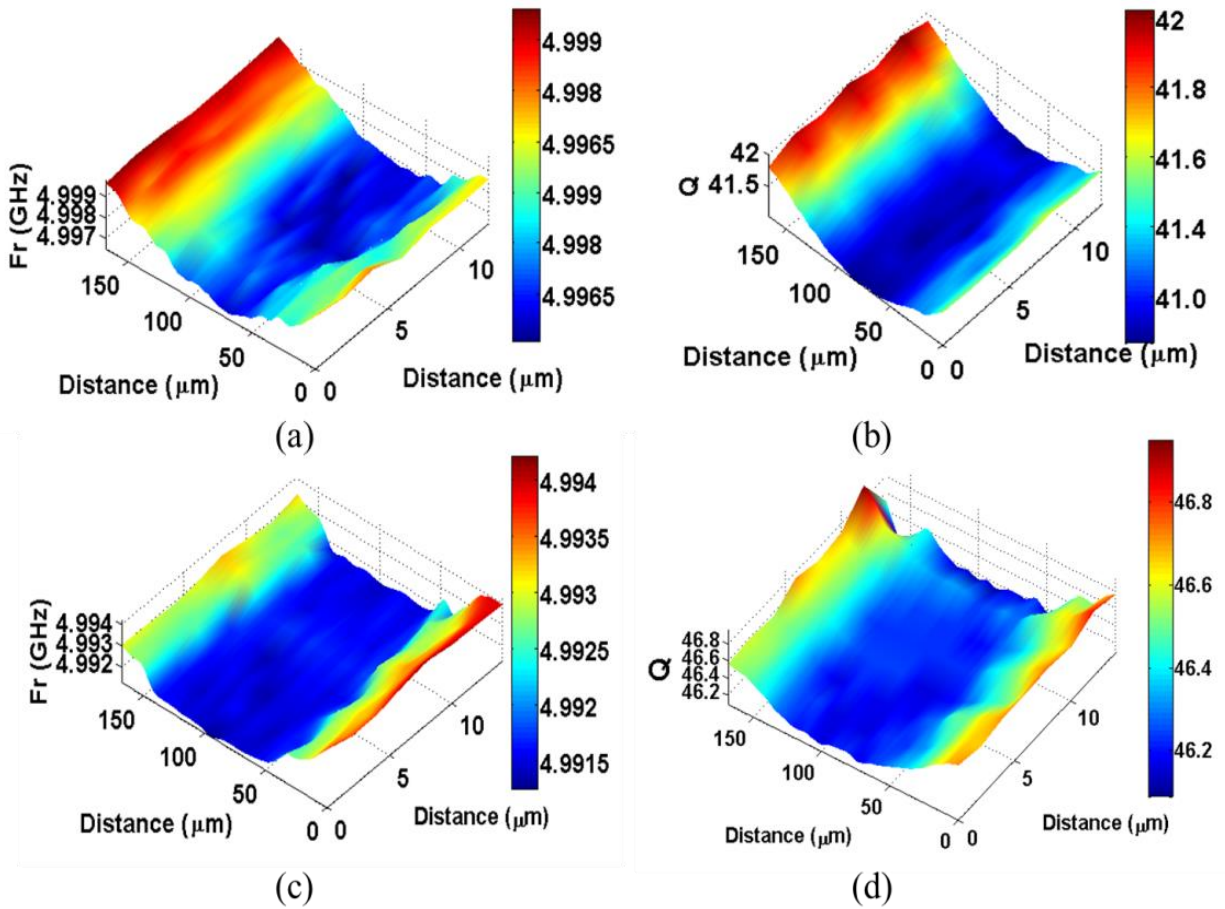


Figure 5-16 Resonance frequency and quality factor plots for parylene-C/Au/glass sample obtained using tips with apex radius of (a)-(b) 10 μm and (c)-(d) 4 μm . Thickness of the parylene-C layer is 10 μm . Tip-sample distance is 100 nm.

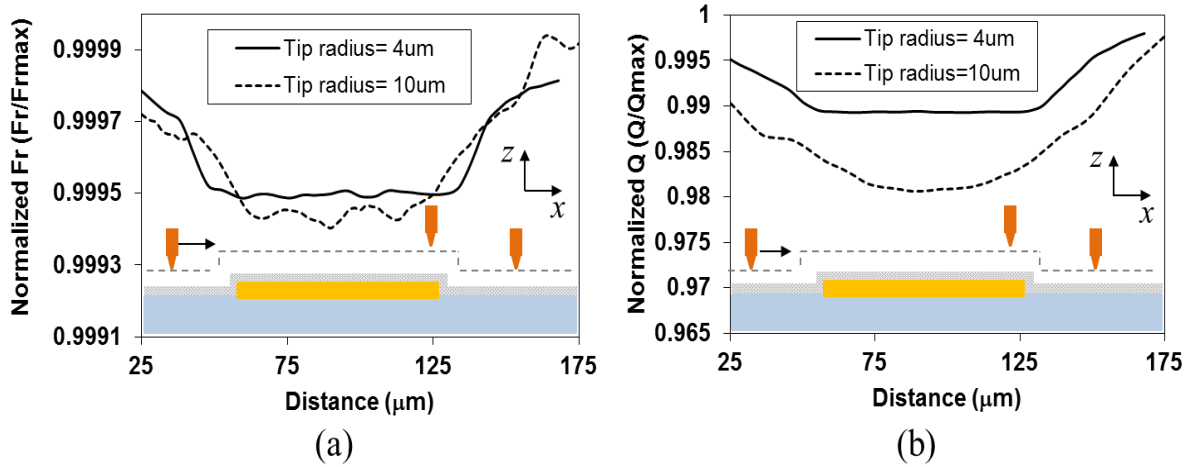


Figure 5-17 Normalized F_r (a) and (b) profile scans along x using tip with apex radius of 10 μm and 4 μm . The illustration of the test sample in the plots is shown for clarification and it is not to scale.

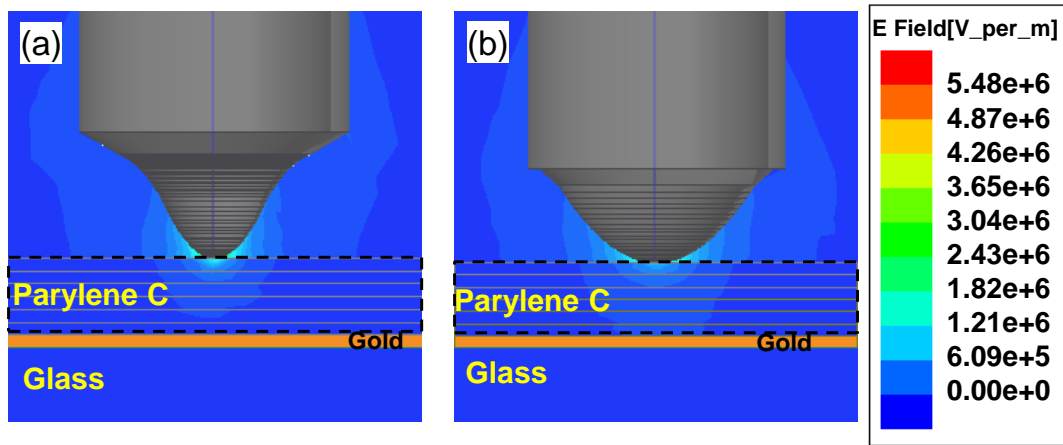


Figure 5-18 Electric field distribution of the tip-sample interaction. (a) Apex radius=10 μm . (b) Apex radius=4 μm . Tip-sample distance is 100 nm for (a) and (b).

The subsurface spatial resolution of the coaxial transmission line resonator-based NFMM is verified using the profiles presented in Figure 5-17. Since the measured profiles correspond to a trace wider (50 μm) than the tips sizes used (4 μm and 10 μm), the spatial resolution is considered to be $2A_w$, where A_w is the apparent width of the measurement as illustrated in Figure 5-19. Thus, from Figure 5-17 (a), the spatial resolution of the NFMM that uses the tip of 4 μm radius is 46 μm , whereas for the NFMM using the 10 μm radius tip, the spatial resolution is degraded by 14 μm . If the Q profiles in Figure 5-17 (b)

are used, the spatial resolution of the NFMM using the tip of 4 μm radius is found to be 72 μm and it is also degraded by 14 μm if the tip is replaced for the one of 10 μm radius.

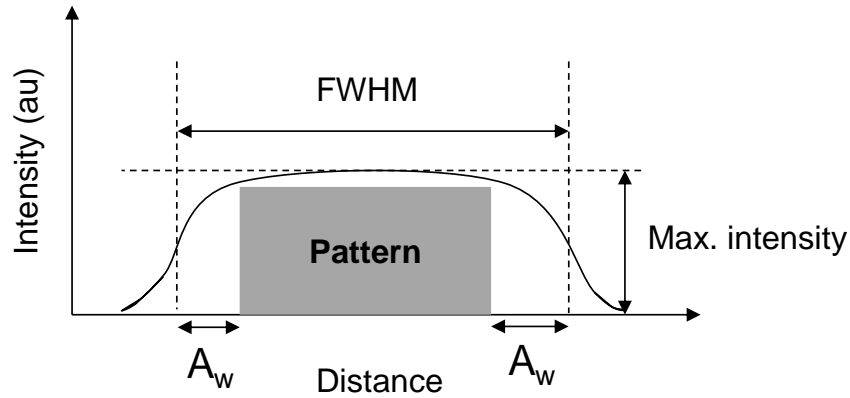


Figure 5-19 Illustration of the determination of the A_w using a measured profile.

5.5 Conclusion

It was found that the DR-based NFMM is able to distinguish different insulating bulk samples ($3.8 < \epsilon_r' < 25$). Particularly, differences in ϵ_r' as small as 1.78 can be resolved using a probe tip with apex radius of 25 μm . The spatial resolution of the microscope was found to be 50 μm and it was determined by scanning a GaAs MMIC phase shifter whose minimum feature size was 10 μm . The scanning was performed at a tip-sample distance of 10 μm .

Additionally, the DR-based NFMM is able to differentiate low-loss and lossy liquids in contact and under in-situ conditions. When the probe is operated under in-situ conditions, improvement of the probe sensitivity to variations in the permittivity of the liquid was observed. Measurements of the quality factor of the resonator reveal that the probe is able to resolve variations around 0.04 in ϵ_r' for low loss liquids. It was found that the spatial resolution of the probe when immersed in mineral oil reduces only by 10 μm , which means that although the sensitivity improves under in-situ conditions, the spatial resolution is not significantly degraded. This was experimentally verified by scanning a MMIC detector covered

with a 30 μm thick layer of mineral oil at a standoff distance of 10 μm . Simulated data using a lumped-element circuit model of the probe and sample support the measured results.

Finally, it was demonstrated that non-contact and non-destructive localized characterization of insulators and conductors coated by insulating polymer films is possible using the coaxial transmission line resonator-based NFMM. It was found that the NFMM is able to distinguish between different bulk dielectrics which are buried in an insulating layer whose thickness is on the order of the tip apex size. Investigation of the influence of the dielectric constant and thickness of the coating film on the sensitivity of the NFMM reveals that even for a high permittivity ($\epsilon'_r = 30$) coating layer, the NFMM is able to differentiate the buried insulating substrates using a tip with an apex radius of 10 μm .

CHAPTER 6 : CHARACTERIZATION OF PRINTED MATERIALS AND DEVICES, AND FLEXIBLE CERAMIC COMPOSITES USING NFMM

6.1 Note to Reader

Portions of this chapter, including figures have been previously published in [20] and [97], and have been reproduced with permission from IEEE. See Appendix A-5 for permission.

6.2 Introduction

NFMM have been mainly used to characterize bulk materials and thin films. However, there is a lack of information regarding characterization of materials with complex structures such as multilayered or additive manufactured microwave devices. Challenges, relevance, summary of previous works, and an overview of the contributions of this work related to NFMM characterization additive manufactured devices, and subsurface characterization of materials are discussed in the next paragraphs.

Realization of novel microwave structures fabricated by additive manufacturing process requires an understanding of both the physical and electrical properties of the materials employed, particularly for high frequency applications where the size of devices is reduced to a point where processing tolerances play a significant role in the performance and reliability achieved. So far, electrical characterization of printed electronics in the microwave frequency regime has been mainly focused on the study of the propagation parameters of ground-signal (G-S) and ground-signal-ground (G-S-G) inkjet printed interconnects [93], and also on the estimation of the bulk dielectric constant and loss tangent of the material employed as the substrate [93]-[94]. However, to the best of the author's knowledge there are no

previous works on localized characterization of electrical properties of printed structures, as presented herein. In this chapter, non-contact measurement of electrical resistance of a printed resistor using the DR-based NFMM is discussed, as well as the simultaneous mapping of surface topography and electrical conductivity of CB028 conductive silver paste with a wide range of electrical conductivity ($2.3 \times 10^6 \text{ S/m} < \sigma < 1.4 \times 10^7 \text{ S/m}$) without the need of a distance sensor. NFMM makes possible the characterization of materials at the surface and in the subsurface which is of importance not only in the characterization of multilayer structures and subsurface defects detection, but also in biomedical applications such as imaging of tumor cells. In [27-29], detection of metallic features embedded in metallic and insulating films using NFMM has been discussed. However, there is a lack of information on the study of the dielectric constant of coated insulating samples which can be of interest for the characterization of ceramic composites. Polydimethylsiloxane (PDMS) can be loaded with ceramic powders such as BaTiO_3 , NdTiO_3 , SrTiO_3 , $\text{Ba}_{0.55}\text{Sr}_{0.45}\text{TiO}_3$ and MgCaTiO_2 in order to develop high- k and low-loss flexible polymer-ceramic substrates suitable for microwave applications such as antennas, filters [95] and baluns [26]. Particularly, $\text{CaTiO}_3\text{-MgTiO}_3\text{-MgTiO}_4$ [49] and $\text{BaTiO}_3\text{-CoFe}_2\text{O}_4$ [50] systems have been characterized using NFMM operating in contact mode. However, to the best of the author's knowledge, this is the first work reporting the non-contact imaging of flexible composites through NFMM. This application presents a major challenge since the contact point with the sample cannot be clearly determined, due to the lack of a well-defined boundary on the region where the quartz tuning fork interacts with the surface; the absence of a well-defined boundary subsequently reduces the effectiveness of distance following feedback system of the NFMM [96]. In contrast, it is shown that a parylene-C layer deposited on the flexible composite allows the distance-following feedback system to determine the contact point with the sample within a distance of 100 nm. This chapter presents the characterization of several insulating crystalline bulk substrates coated with an insulating layer as well as the imaging of PDMS- $\text{Ba}_{0.55}\text{Sr}_{0.45}\text{TiO}_3$ 49% coated with a 10 μm thick parylene-C layer using the coaxial resonator

transmission line-based NFMM. Finally, sub-surface spatial resolution and sensitivity of the NFMM is discussed by imaging a parylene-C coated gold trace using tips of different radii.

6.3 Characterization of Direct Digital Additive Manufactured Conductive Materials and Thick Film Resistor

This section is divided into two parts. In the first part, non-contact measurement of electrical resistance of a polymer thick film printed resistor using the DR-based NFMM is presented. In the second part, simultaneous RF electrical conductivity and topography mapping of direct digital manufactured conductive inks using the DR-based NFMM is discussed.

6.3.1 Non-contact Characterization of Polymer Thick Film Printed Resistors

The characterization of the printed resistor was carried out using the DR-based NFMM which employs a probe tip with an apex radius of 200 μm . The printed resistor was fabricated by Daniel Silva (nScript) through direct print additive manufacturing using an nScript Tabletop 3D printer and a 50 μm /100 μm inner/outer diameter pen tip. The materials employed were DuPont CB028 silver conductor, DuPont 7082 carbon conductor and FR-4 as the substrate. The silver pads were printed first with a curing temperature of 120°C for 90 minutes. Then, the carbon conductor was printed and the entire sample was cured at 120°C for 20 minutes. The schematic and photograph of the fabricated resistor are shown in Figure 6-1 [97]. Due to the printing process, there are two regions where the carbon conductor overlaps the silver pads.

The method proposed in this work to characterize the printed resistor is based on the measurement of the quality factor Q of the microwave probe as a function of the tip-sample distance d . The printed resistor is scanned at a fixed z -height; thus any change in the surface topography will produce

a change in \mathbf{d} . Furthermore, it is assumed that the conductivity of the carbon conductor is constant across the resistor (sheet resistivity = $400 \text{ } \Omega/\text{sq}/\text{mil}$ [98]). With this approach changes in Q can be correlated with film thickness and therefore resistance.

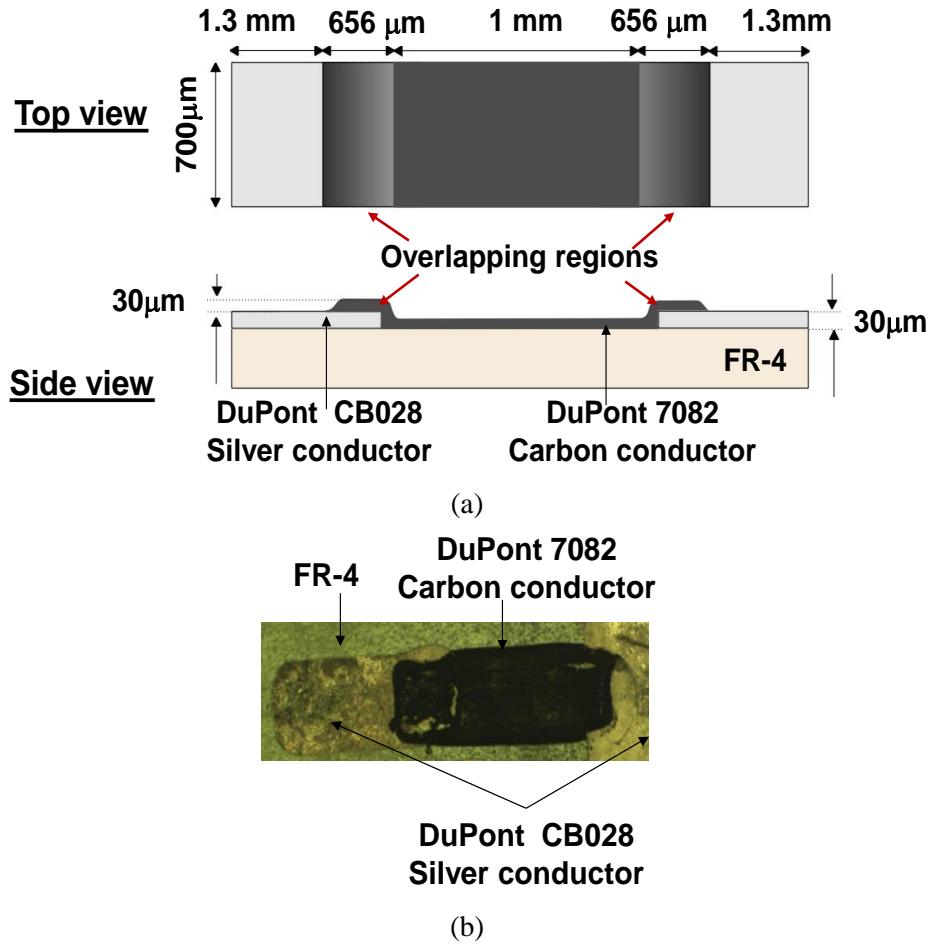


Figure 6-1 Printed resistor illustration (a) and micrograph (b). Dimensions shown in the illustration were obtained using a Dektak 150 profilometer.

From Figure 6-2 (a) it can be seen that both F_r and Q are sensitive to the proximity of the carbon conductor and decreases with \mathbf{d} . In NFMM, a reduction in Q is associated with the losses in the sample and so Q seems a more logical choice than F_r to quantitatively estimate the electrical resistance. As shown in Figure 6-2 (a) the Q response can be approximated by a polynomial equation described by

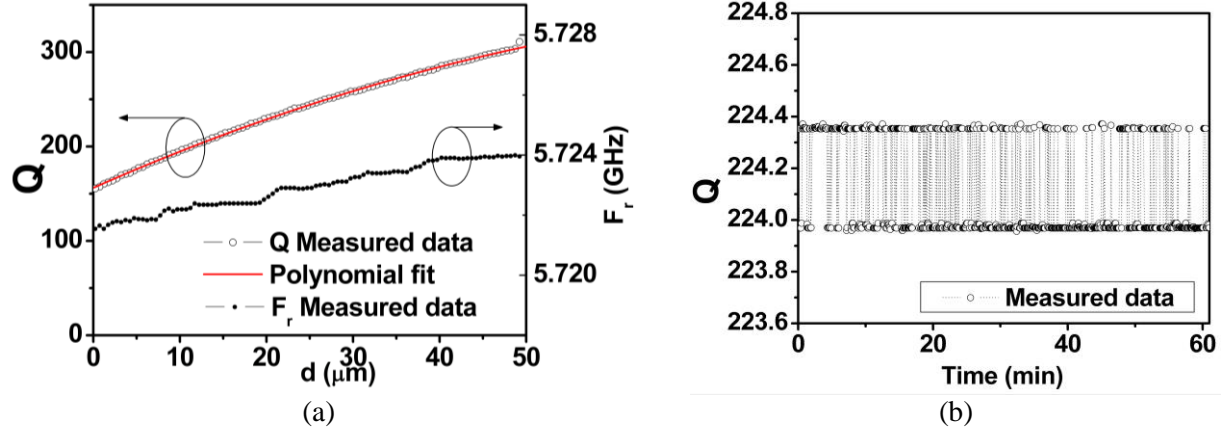


Figure 6-2 (a) Q and F_r plot versus d for DuPont 7082. The solid line represents the polynomial fit for Q vs. d . (b) System noise measured at $d=18 \mu\text{m}$.

$$d = A + B_1 \cdot Q + B_2 \cdot Q^2 \quad (42)$$

where $A = -14.436$, $B_1 = -0.022$ and $B_2 = 7.532 \times 10^{-4}$. During a scan over the resistor, Q data is acquired at each scan step ($20 \mu\text{m}$) and then it is transformed to d using interpolation. Hence, measured Q images can be transformed to topographical changes. Fitting of experimental data to a polynomial equation has been successfully employed to image material properties from measured data. In [16], sheet resistance images of YBCO thin films were obtained from measured Q data using a least-squares equation.

In order to confirm that variations in Q are not associated with system noise but with topography variations, the microwave probe-tip was positioned at a distance $d = 18 \mu\text{m}$ above the carbon conductor and Q was acquired for 60 minutes as shown in Figure 6-2 (b). From Figure 6-2 (b), the mean value of Q and its standard deviation were found to be 224.1 and 0.18, respectively. Moreover, from this measurement the signal-to-noise ratio (SNR) can be determined according to [99].

$$\text{SNR} = \frac{\mu^2}{\sigma^2} = \frac{P_S}{P_N} \quad (43)$$

where μ^2 and σ^2 are the square values of the signal mean and standard deviation of the noise, respectively; and P_S and P_N are the average signal and noise power, respectively. From data in Figure 6-2 (b) and (43), the SNR is found to be $10 \cdot \log(\text{SNR}) = 61.90$ dB. In order to determine the influence of the tip-sample proximity on the SNR, the resistor was positioned at different distances **d** below the tip and Q was acquired for 60 minutes. Using the procedure mentioned previously, the SNR at each **d** was calculated and is shown in Table 6-1. From this table it can be seen that the SNR does not vary significantly with **d**. The mean value of the SNR is 59.4 dB with a standard deviation of 2.40 dB.

Table 6-1. Signal-to-noise ratio at different tip-sample distances

d (μm)	SNR (dB)
5	58.00
15	58.46
18	61.90
25	62.98
35	58.16
45	57.07

The resistance is computed using the expression $R = \rho \cdot L / (W \cdot h)$ where ρ is the material resistivity which has to be known, L is the resistor length, W is the resistor width, and h is the resistor thickness. To demonstrate the method proposed, the resistor shown in Figure 6-1 (b) was scanned in steps of 20 μm. After the contact point was established, the sample was lowered by 80 μm and an *xy* scan was performed. The acquired Q data is converted to height variation using the polynomial equation presented above. The topography of the printed resistor is shown in Figure 6-3(a). From Figure 6-3(a) and (b), the

overlapping regions (DuPont 7082/DuPont CB028), substrate (FR-4) and carbon conductor (DuPont 7082) can be identified.

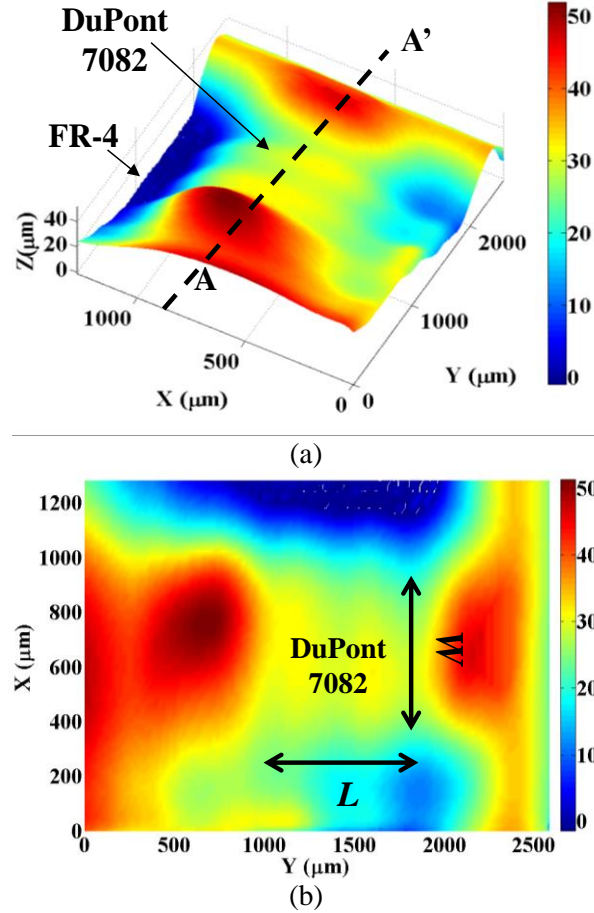


Figure 6-3 Topography of the printed resistor obtained through NFMM. (a) 3D plot. (b) Top view.

Ten profiles along the length and ten profiles along width of the resistor were obtained using NFMM, and they were used to determine the average values and standard deviations of W and L . Examples of these profiles are shown in Figure 6-4(a) and (b). W is considered to be the full width at half maximum ($Z/2$). The mean value of W was found to be $\mu = 717.26 \mu\text{m}$ with a standard deviation of $\sigma = 75.26 \mu\text{m}$. L is considered to be the full width at the half maximum ($P/2$), where the maximum (P) is determined by the difference between the maximum of the overlapping peaks and the average of the carbon film height h . The mean value and standard deviation of L are found to be $\mu = 1088.44 \mu\text{m}$ and σ

= 17.48 μm , respectively. Significant values of standard deviation obtained for W and L are explained by the non-uniformity achieved by the printing process, which is influenced by printing conditions such as curing temperature, curing time and printing speed. Error on the estimation of h , is determined by the repeatability of the Z-axis M112.1DG positioning stage, and is reported to be 100 nm [100]. A profile along the length of the resistor was obtained using a Dektak 150 commercial profilometer. Results presented in Figure 6-4 (b) and (c) show that the profiles agree very well. However, the measurement obtained with the profilometer provides greater spatial resolution. This difference is due to the tip size employed in each case. For the NFMM measurements the tungsten tip radius is 200 μm whereas the profilometer stylus diameter is 12.5 μm .

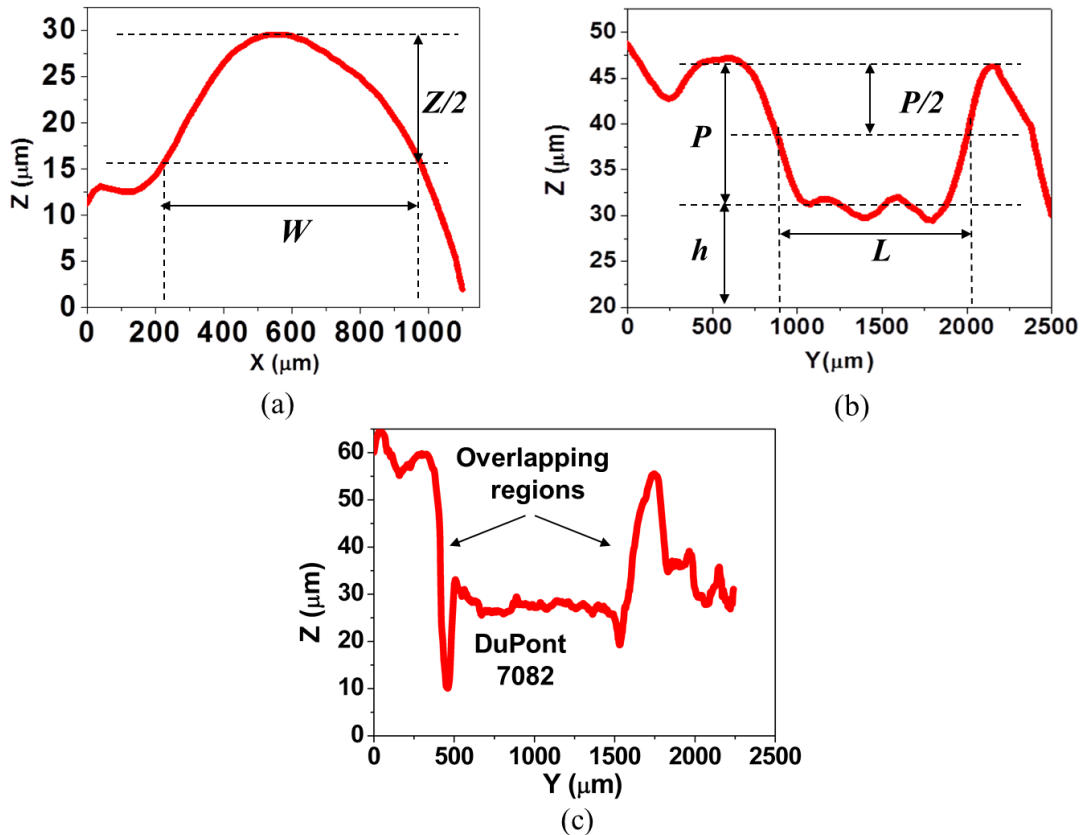


Figure 6-4 Profiles along the width (a) and length (b) of the resistor using NFMM. (c) Profile along the length of the resistor (A-A' line) using a Dektak 150 commercial profilometer.

A 3-D plot showing the electrical resistance calculated using the average values of W and L , and the carbon conductor resistivity is presented in Figure 6-5. Each point in this plot acts as a small resistor and contributes to the total resistance as illustrated in the lumped element model. The resistors that are following the current flow (I) such as A_{11} through A_{1n} are added in series whereas the resistors that are perpendicular to the current path are added in parallel. Thus, the total electrical resistance of the printed resistor is expressed by $R = \left((R_{1n} || R_{2n} || R_{3n}) \dots || R_{mn} \right)$ and it is computed to be 1.289 k Ω .

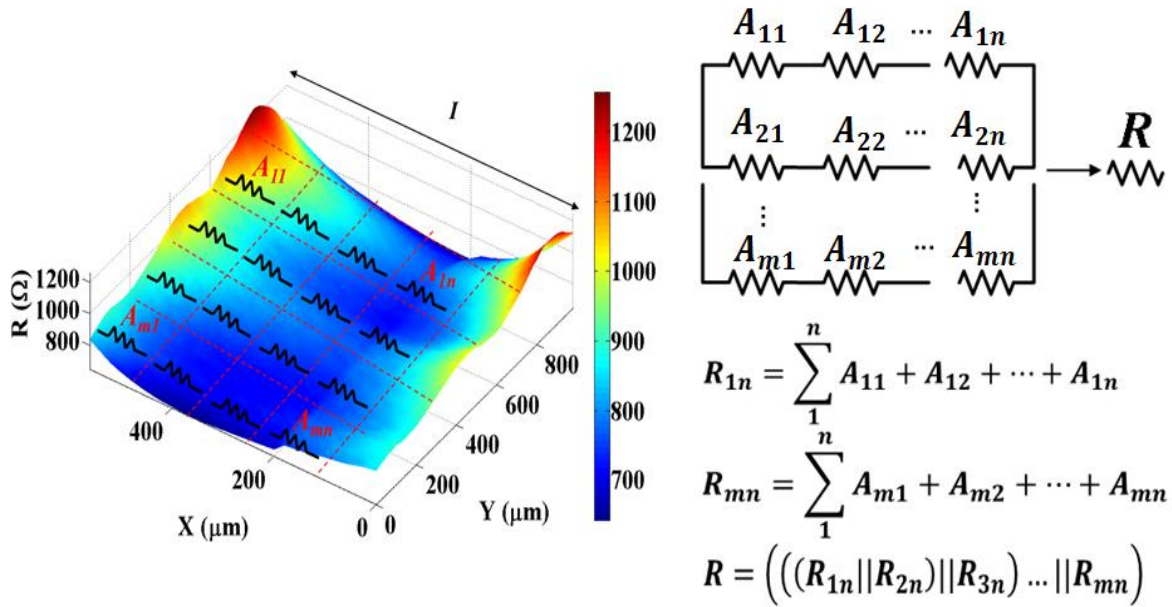


Figure 6-5 Electrical resistance image and equivalent lumped-element circuit model.

It is of interest to study the influence of the standard deviation of the resistor dimensions W and L on the computed electrical resistance. To accomplish this task, the electrical resistance is calculated using the expression $R = \rho \cdot L / (W \cdot h)$, and the equivalent lumped-element circuit model shown in Figure 6-5, and the dimensions in Table 6-2. Dimensions in this table provide an average (1289 Ω), maximum (1462 Ω) and minimum (1148 Ω) electrical resistance.

Table 6-2. Resistor dimensions and computed electrical resistance

Width (μm)	Length (μm)	R (Ω)
$W+\sigma$	$L-\sigma$	1148
$W-\sigma$	$L+\sigma$	1462
W (mean)	L (mean)	1289

- Electromagnetic Simulation of the Resistor

The printed resistor was simulated in ANSYS Maxwell 3D. The geometry used for simulations was that measured with the Dektak 150 surface profiler. The DC conduction solver was employed and a voltage difference of 1V was applied to the silver contact pads as shown in Figure 6-6. The current density J (A/m^2) is observed to vary with the surface topography, decreasing around 12% over the center of the carbon conductor section where the thickness is increased by 6 μm . The maximum current density of $3.6 \times 10^5 \text{ A}/\text{m}^2$ is achieved near the inner edge of the silver pad on the left hand side, as shown in Figure 6-4(c), where the carbon thickness is significantly reduced to less than 10 μm . The simulated electrical resistance of the resistor is calculated through $R = V/I$, where V is the voltage difference applied (1V) and I is the electrical current flowing through the resistor. The computed result is 1.424 k Ω , in good agreement with the NFMM measurements. The electrical current is computed through the expression $\int \vec{J} \cdot d\vec{S}$ and is found to be 0.702 mA.

- Four-Point Probe Measurement

The electrical resistance of the printed resistor was also measured using the four-point probe method. An Agilent E3631A current source was connected to two T-4-10 tungsten needles and a current of 3.35 mA was applied. The voltage across the resistor was measured with a Keithley 2000 multimeter that was connected to another pair of T-4-10 tungsten needles. The measured voltage was 5.008 V and the calculated resistance was 1.494 k Ω in good agreement with the NFSMM and EM simulation results.

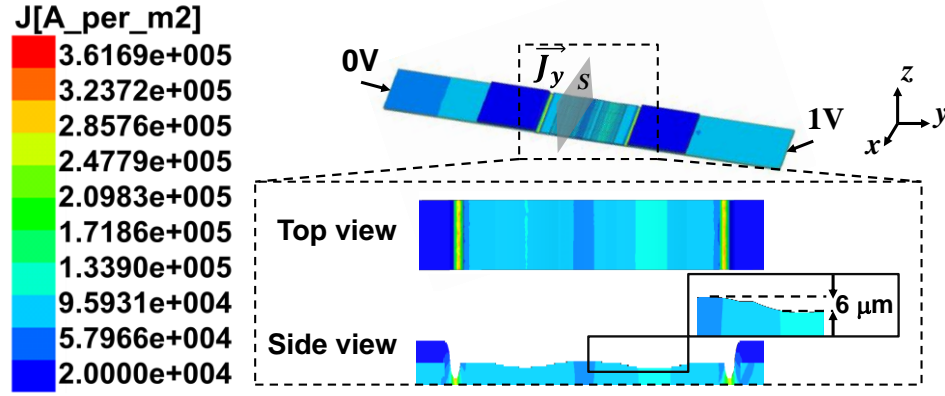


Figure 6-6 Simulated electrical current density plot on the resistor.

6.3.2 Non-Contact Characterization of Conductive Inks

The conductivity and profile of layers fabricated with micro-dispensing systems are affected by several process factors, including: partial clogging of the pen tip, conductive ink inhomogeneity, valve opening and closing speed, air pressure, printing path size, curing time and temperature, etc. Figure 6-7 shows SEM micrographs of cross sections of a trace made with DuPont CB028 silver paste around its middle (a) and close to one edge (b). As seen in Figure 6-7 (a) and (b), there is a non-uniform distribution of ink particles and higher particle density is observed at the bottom portion of the trace compared to the top surface region. Additionally, the thickness on the edge of the trace is tapered.

Typical techniques used to measure electrical conductivity (e.g. the DC 4-point probe) provide an averaged value across the entire sample cross-section; however, it is important to identify localized variation in conductor properties for high frequency applications as the current is strongly concentrated near the edges. In this section, simultaneous mapping of the RF electrical conductivity and the surface topography of the printed inks using the DR-based NFMM and a tip with apex radius of 25 μm is presented.

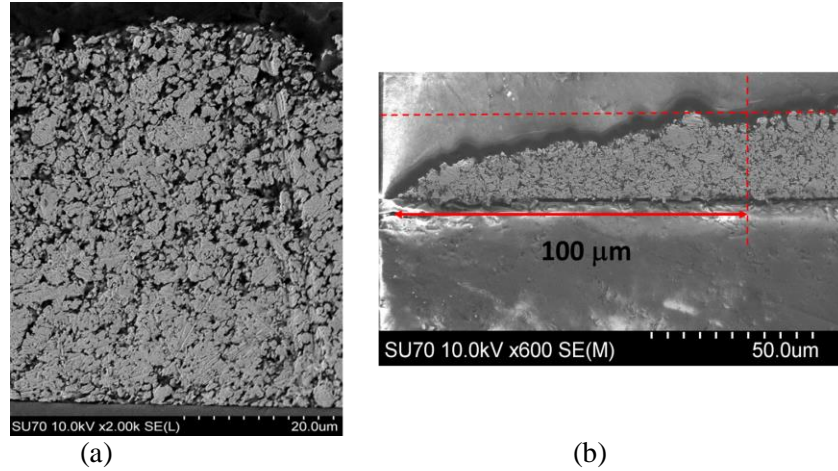


Figure 6-7 SEM micrographs of the cross section of CB028 around the middle of the trace (a) and close to the side edge of the trace (b).

The material under study is the CB028 conductive ink used in the slot ring resonator printed on a Rogers RO570 substrate shown in Figure 6-8. The printing was performed by Eduardo Rojas (University of South Florida) using an nScript Tabletop microdispensing system and Ag microparticle DuPont CB028 paste for the realization of the conductive layer. The pressure of the system was constant at 15 psi, and the inner diameter of the pump tip is 125 μm [20].

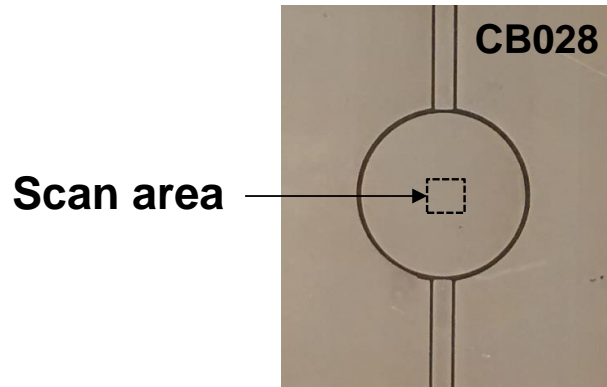


Figure 6-8 Photograph of the additive manufactured CB028 slot ring resonator.

In order to extract the electrical conductivity of the conductive ink, the DR-based NFMM is calibrated by recording Q at $d = 3 \mu\text{m}$ for three standard metallic samples: nickel, vanadium and titanium.

Then the conductivity an unknown sample can be obtained from measured Q using interpolation .This tip-sample distance was chosen for calibration as it will be the distance at which the xy scanning will be performed. Conductivity of the calibration samples is listed in Table 6-3 and is calculated through $\sigma=1/(R_s \cdot t)$, where R_s is the sheet resistance and t is the sample thickness. R_s is measured using a Jandel RM3000 four point probe. Figure 6-9 shows Q vs. σ for $d = 3 \mu\text{m}$. From this figure, it can be seen that Q degrades as the conductivity of the sample decreases. This behavior is explained by the fact that more energy is dissipated in samples with lower conductivities. The relationship between Q and σ can be approximated by an exponential equation defined by

$$\sigma = 5.36e - 21 \cdot \exp(Q/16.85) + 0.36 \text{ (MS/m)} \quad (44)$$

Table 6-3. Electrical conductivity of standard conductive samples measured using a Jandel RM3000 four point probe

	Nickel	Vanadium	Titanium
Electrical conductivity (S/m)	1.4e7	4.6e6	2.3e6

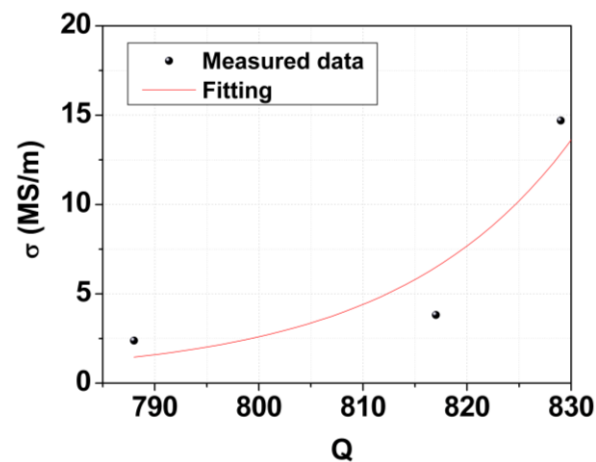


Figure 6-9 Calibration plot.

In addition to electrical conductivity, surface topography is also measured during a xy scan. For this purpose, the DR based NFMM employs the distance following mechanism discussed in Section 3.4, which monitors the frequency shift that occurs at the contact point between the probe tip and the conductive ink. The scan was performed for over an area of $50\ \mu\text{m} \times 50\ \mu\text{m}$ around the center of the sample in X/Y steps of $2\ \mu\text{m}$. At each point of the scan, Q and topography are simultaneously acquired. Then Q is correlated with σ using the exponential equation (44). Figure 6-10 show topography and conductivity images of the CB028 film. From these images, it can be seen that there is a correlation between conductivity and surface topography. The correlation coefficient between these images is computed to be $\rho=-0.45$, which indicates that the conductivity and topography plots are negative linearly correlated. Higher surface areas show higher conductivity ($1.1\text{e}7\ \text{S/m}$) whereas lower surface areas exhibit much lower conductivity values ($0.4\text{e}6\ \text{S/m}$). A lower electrical conductivity on the surface may be explained by the fact that the micro-particle density is lower here, as shown in the SEM micrograph in Figure 6-7 (a). This variation could significantly impact the performance of microwave printed devices, especially as the operating frequency increases.

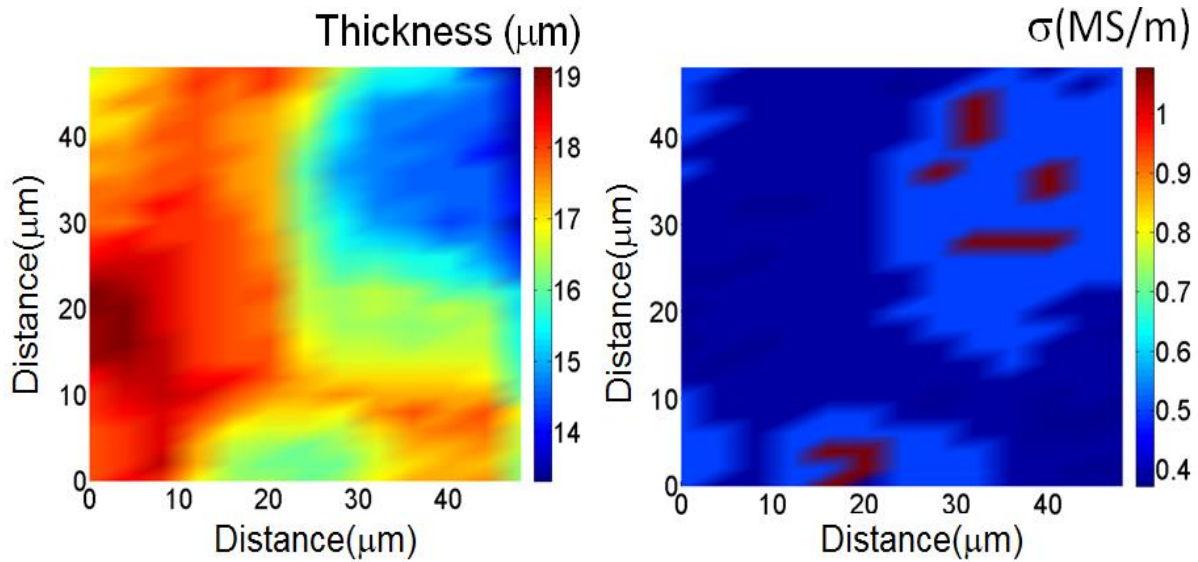


Figure 6-10 Topography (left) and conductivity (right) images of CB028.

With the aim of validating the NFMM measurements, measured arithmetic average roughness (R_a) and electrical conductivity are compared with the values provided by a commercial profiler and a four-point probe, respectively. R_a is calculated using (45) and Z_i represents the height value for the i^{th} data point of the sample, n is the total number of elements of the dataset, and μ_Z is the mean value of the height. The dataset from the NFMM image and profilometer covered a $50\text{ }\mu\text{m} \times 50\text{ }\mu\text{m}$ area.

$$R_a = \frac{1}{n} \sum_{i=1}^n |Z_i - \mu_Z| \quad (45)$$

Although these calculations are comparing the height values of different regions of the same sample, there is a close agreement between the surface roughness parameters obtained from the two measurement methods, as shown in Table 6-4. Table 6-5 shows the measured electrical conductivity of CB028 using the four-point probe technique and the average electrical conductivity computed from the image in Figure 6-10 (right). The NFMM conductivity is about an order of magnitude lower than the one measured using the four-point probe method. Possible reasons for this discrepancy are that the NFMM provides a localized measurement of conductivity over the sample's surface rather than an averaged conductivity value across the entire bulk sample as the four-point probe method does. As can be observed from the SEM micrograph in Figure 6-7 (a), the CB028 trace is not homogenous and there is a lower silver particle density on the surface layers than at the bottom layers. The effect of this non-uniform particle distribution across the trace may not be observed in the dc four-point probe measurement, which assumes the material under study is uniform and homogenous. However, in NFMM, the volume under study in the sample is determined by the material properties, tip-size and tip-sample distance. In order to determine this volume under study, a simulation of the electric fields around the tip and sample is carried out using the electrostatic simulator ANSYS Maxwell. The cross section of the CB028 in that was recreated using the SEM image shown in Figure 6-11 (a). Figure 6-11 (b) shows the tip-sample geometry used in simulations. The tip-sample distance is $d = 3\text{ }\mu\text{m}$. Figure 6-11 (c), the simulated electric fields around the tip and

sample can be seen. In the sample, the fields decay by about half of the intensity in about 3 μm below the surface and vanish in about 6 μm . The fields extend laterally in the sample in a region about the diameter of the probe tip. Fields extension of about 6 μm in depth in this type of conductive sample is explained by fact that the material is composed of silver particles and air voids.

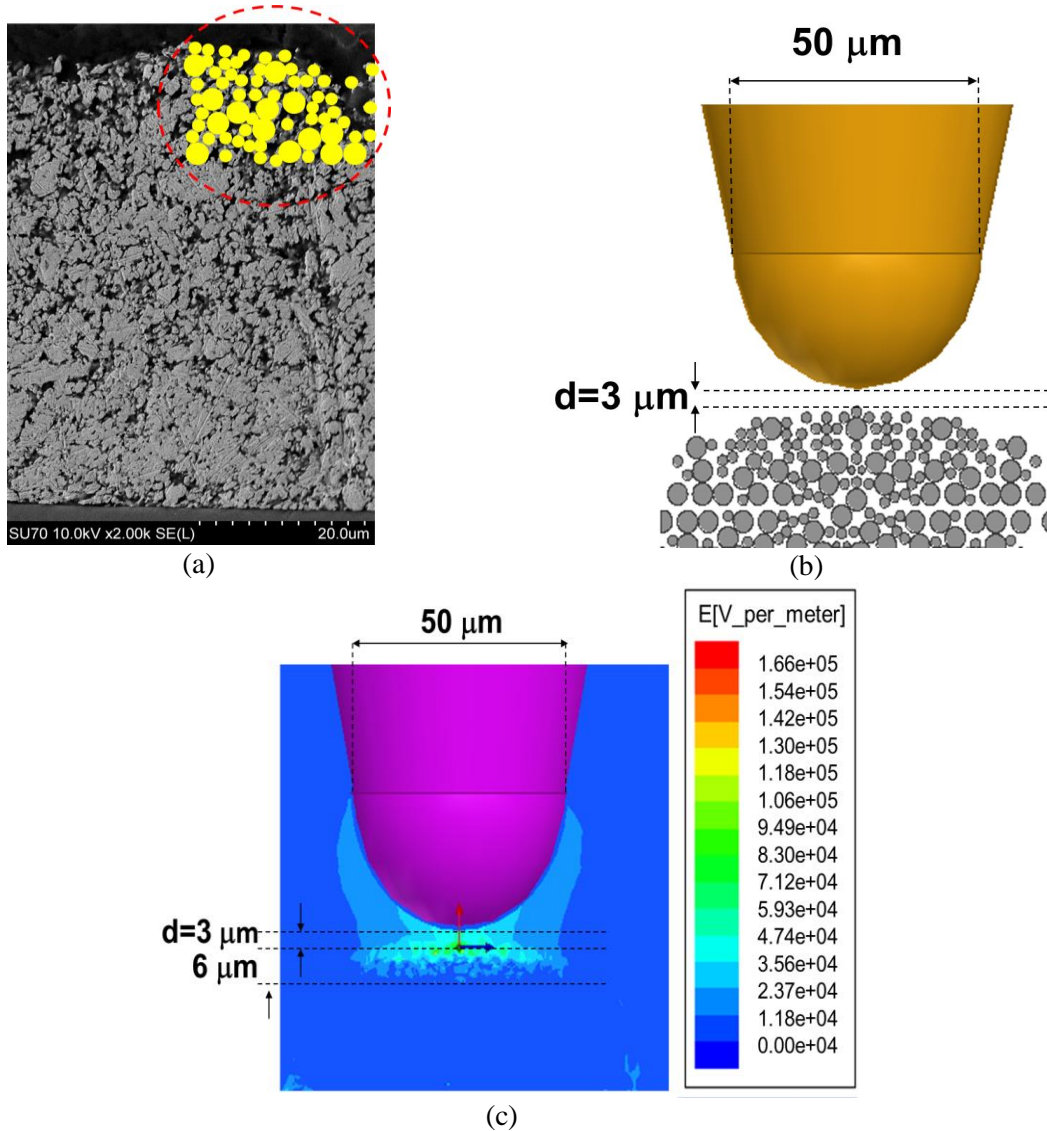


Figure 6-11 (a) SEM of the cross section of a CB028 sample. In the region enclosed by the red circle, silver particles are represented by spheres with radius of 1 μm and 2 μm . This region was used as reference to recreate the sample in the electrostatic simulator. (b) Tip-sample geometry in ANSYS Maxwell. (c) Simulated E-field plots of the tip-sample interaction.

Table 6-4. Roughness measurement method comparison

Material	Roughness(Ra) Measurement Method	
	NFMM	Veeko Dektak 150
CB028	1.15 μm	3.68 μm

Table 6-5. Electrical conductivity measurement method comparison

Material	Conductivity Measurement Method	
	NFMM	Four-point probe
CB028	0.7e6 S/m	4.8e6 S/m

It is clear that the uneven distribution of silver particles impacts the RF electrical conductivity of the CB028 traces which could have significant consequences on the performance of microwave devices and systems. To model the effect of the particle distribution on the performance of a single trace, a CB028 microstrip line on Rogers3003 has been simulated at 2 GHz in HFSS considering the CB028 trace as a composite material comprised of three layers, with the lower one the more conductive and the higher one the less conductive. In this model, it is assumed that lower concentration of particles at the top layer results in a layer with lower electrical conductivity (0.7 MS/m) compared to the medium (1 MS/m) and bottom layers (4 MS/m). Figure 6-12(a) shows the schematic of the trace made of composite material and Figure 6-12(b) shows the surface current density of the cross section of the trace. As can be observed the current is mainly concentrated around the bottom at the edge, where less particle density is achieved and where the thickness is considerably reduced. For comparison purposes, the attenuation constant of a trace whose conductive material is uniform with an electrical conductivity of 4e6 S/m is 0.033 Np/m whereas that of the non-uniform trace is 0.66 Np/m. The length of the trace is 5 mm for both cases. This result shows that the attenuation constant of the microstrip line with uneven current distribution is 20 times higher than that of the same trace with uniform conductivity of 4 MS/m. Consequences of this result could be observed for example in filters with high insertion loss in the pass-band or resonators with low quality factor.

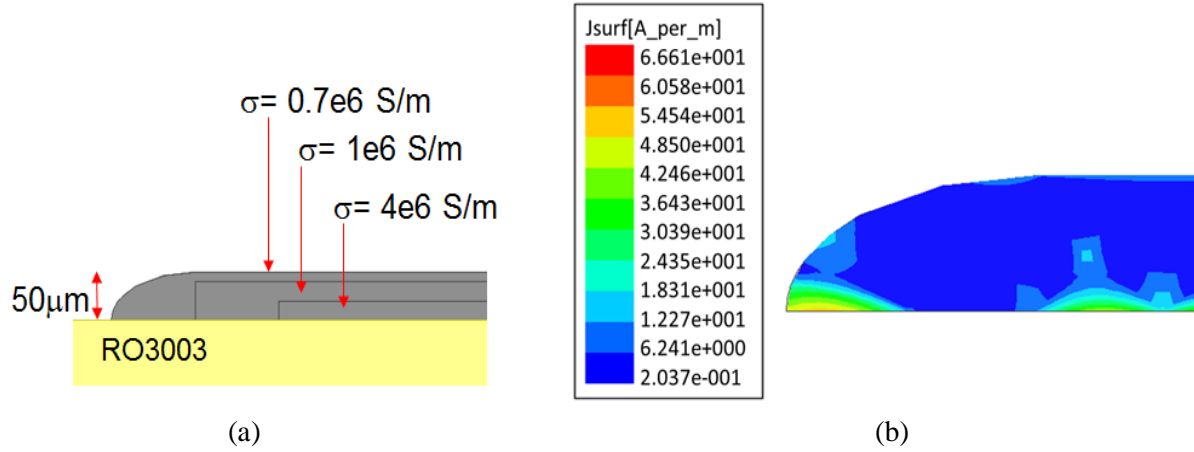


Figure 6-12 (a) Schematic of the microstrip line using a composite conductive material. (b) Surface current density plot of the cross section of the composite conductive material.

6.4 Characterization of Flexible Ceramic Composites

The mapping of dielectric properties is of special interest for the characterization of high- k polymer-ceramic composites such as PDMS-MgCaTiO₂ and PDMS-Ba_{0.5}Sr_{0.5}TiO₃. One challenge faced in the non-contact imaging of these flexible substrates using the distance-following feedback system of the NFMM is that there is no certainty in the contact point determination, as the amplitude of oscillation of the quartz tuning fork decreases slowly as the sample approaches the probe tip. This behavior is illustrated in Figure 6-13, in which a shallow slope in the output voltage of the fork as a function \mathbf{d} is observed for the PDMS-Composite (No coating) curve. For clarification, in the figure, the slope change is shown to occur at a tip-sample distance of zero however there is no certainty that this point corresponds to the actual contact point. This uncertainty in \mathbf{d} could not only result in damages to the sample and tip but also in uncertainties in the NFMM measurements. It has been determined, however, that depositing a parylene-C layer on the flexible composite material can overcome this issue. To demonstrate, the PDMS-Composite (Coated) curve shown in Figure 6-13 exhibits a rapid reduction of the output voltage of the fork as the tip comes within 100 nm of the sample. Thus, for the coated material, height control can be achieved by monitoring the fork voltage. The measured behavior of these two samples can be explained

by the difference in the Young's modulus of the top layer with which the fork interacts. The PDMS-based polymer composites have a flexible structure and PDMS has a lower Young's modulus (~ 750 KPa [101]) than that of parylene-C (~ 3.2 GPa [102]). This dependence of the fork output on the rigidity of the sample is discussed in [96] where it is observed that for alumina, the Q of the fork drops abruptly as the tip comes within 200 nm of the sample, whereas for polyethylene, the drop in Q is slower and occurs within 900 nm of the sample.

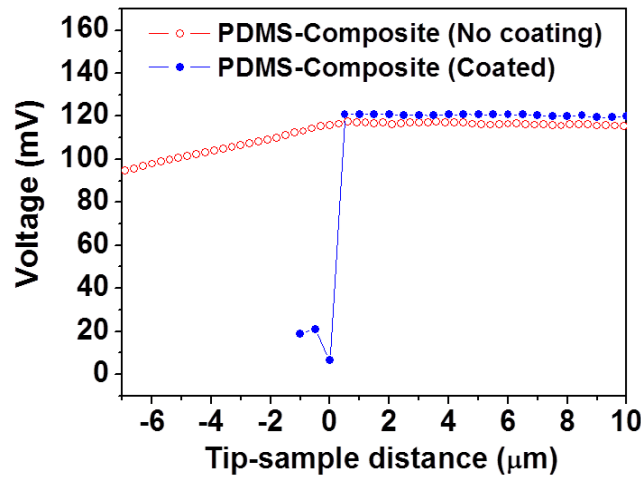


Figure 6-13 Fork output voltage versus d for PDMS-Ba_{0.5}Sr_{0.5}TiO₃ 49% with and without parylene-C coating.

- Imaging of Dielectric Subsurface Features

NFMM imaging of the polymer-ceramic composite made of PDMS-Ba_{0.55}Sr_{0.45}TiO₃ 49% coated with a 10 μm thick parylene-C layer was carried out over an area of 50 μm x 50 μm in steps of 2 μm at a constant tip-sample distance of 100 nm. The PDMS-Ba_{0.55}Sr_{0.45}TiO₃ 49% sample was prepared by Juan De Dios Castro (USF) following the methodology presented in [24]. The dielectric constant and loss tangent of the composite were separately measured using a cavity resonator and found to be 22.7 and 0.032 at 4.26 GHz, respectively. During the scan, F_r and surface topography images of the sample were acquired simultaneously. From Figure 6-14(a) and Figure 6-14(b), it can be observed that there is no direct correlation between topography (surface height) and F_r which indicates that measured variations in

F_r are a consequence of localized changes in the permittivity of the composite. The correlation coefficient between these images is computed to be $\rho = -0.11$, which indicates that the surface topography and F_r are linearly negative and have negligible correlation. Surface topography image Figure 6-14(a) reveals patterns of parallel lines which are marks from the mold used for sample preparation. Microscope images of the sample and mold confirm this observation as shown in Figure 6-14(c). From Figure 6-14(b) it is clear that F_r , and therefore the permittivity distribution is not constant over the scan area and that a concentration of lower permittivity (higher F_r) is observed on the left side of the sample. This region could represent PDMS ($\epsilon_r = 2.77$ at frequencies up to 40 GHz [103]) that was not effectively mixed with the $\text{Ba}_{0.55}\text{Sr}_{0.45}\text{TiO}_3$ ceramic particles ($\epsilon_r = 2367$ at 1KHz [19, 104]) as can be observed in the SEM micrograph shown in Figure 6-14(d). It can be noted that a $\sim 50 \mu\text{m}$ thick PDMS region is formed on top of the sample and that PDMS-ceramic agglomerates are distributed across the sample. It is worth noting that NFMM and SEM imaging were carried out around the center of the sample over similar areas. The average, minimum and maximum frequency observed in Figure 6-14(b) are 4.9889 GHz, 4.9867 GHz and 4.9904 GHz respectively. These values translated to permittivity are $\epsilon_{st} = 8.37$, $\epsilon_{st} = 11.78$ and $\epsilon_{st} = 6.63$, respectively. Permittivity is obtained from interpolation of the data shown in Figure 5-7(b) and Figure 5-8 (a), from which a calibration data set can be obtained in the form (F_r vs. ϵ_{st}) for tip-sample distance of 100 nm and 10 μm thick parylene layer.

The average permittivity of the PDMS- $\text{Ba}_{0.55}\text{Sr}_{0.45}\text{TiO}_3$ 49% sample obtained using NFMM is about half of the measured value using the cavity resonator technique. The discrepancy can be explained by the fact that the cavity resonator technique extracts an effective permittivity over a volume of about 5 cm x 5 cm x 0.5 mm whereas the NFMM study volume is determined by the scan area 50 μm x 50 μm and the estimated penetration depth 30 μm . Within this small volume near the surface, localized composition differences such as the low permittivity PDMS layer formed on top of the sample (see Figure 6-14(d)) and the presence of PDMS- $\text{Ba}_{0.55}\text{Sr}_{0.45}\text{TiO}_3$ agglomerates strongly influence the extracted NFMM permittivity. Furthermore, well-known theoretical models such as the Maxwell-Wagner's model

and the Bruggeman's model [105, 106] predict effective dielectric constants of polymer composites that are significantly lower than the average of the permittivity of the polymer and ceramic themselves. Thus, a much lower permittivity of PDMS-Ba_{0.55}Sr_{0.45}TiO₃ 49% would be expected for the NFMM interaction volume, where more PDMS is present in the volume than ceramic particles (see Figure 6-14(d)), compared to the content in the larger volume considered in the cavity resonator measurements.

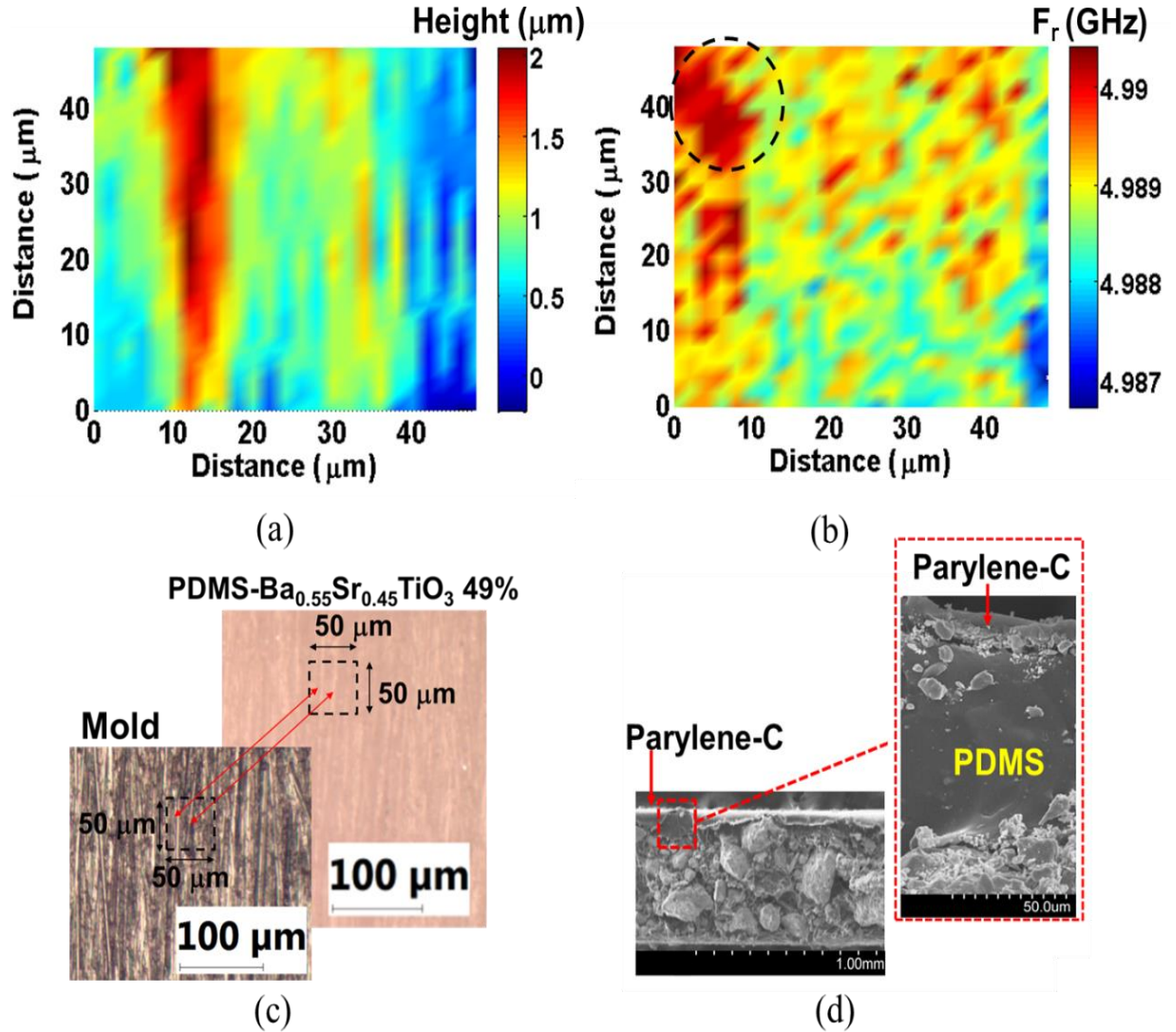


Figure 6-14 (a) Surface topography and (b) F_r image of PDMS-Ba_{0.55}Sr_{0.45}TiO₃ 49% coated with a 10 μm thick parylene-C layer. (c) Microscope image of PDMS-Ba_{0.55}Sr_{0.45}TiO₃ 49% and stainless steel mold. (d) SEM micrograph of the cross section of PDMS-Ba_{0.55}Sr_{0.45}TiO₃ 49% coated with a 10 μm thick parylene-C layer. Tip-sample distance is 100 nm for (a) and (b).

In order to confirm that measured variations in F_r are not associated with system noise, the microwave probe tip was positioned at a $d= 100$ nm and F_r was acquired for 240 minutes as shown in Figure 6-15. It can be seen that the peak-to-peak frequency variation is 350 KHz and that the mean value of F_r and its standard deviation are found to be 5.03791 GHz and 9.17932×10^{-5} GHz, respectively. The SNR obtained from (43) [99] is found to be 94.78 dB

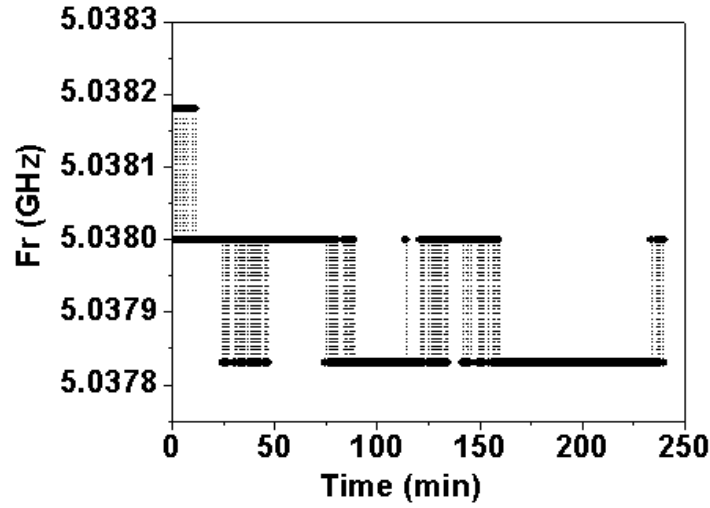


Figure 6-15 System noise measured at $d= 100$ nm.

6.5 Conclusion

In this chapter, it was shown that the DR-based NFMM can be used for localized characterization of passive printed electronics and for simultaneous measurement of electrical conductivity and surface topography of rough conductive printed materials such as CB028 silver paste. Particularly, non-contact measurement of electrical resistance of a printed resistor using the DR-based NFMM was discussed. The resistance computation employs the surface profile information obtained through non-contact Q measurements of the printed resistor over an average area of $1088 \mu\text{m} \times 717 \mu\text{m}$, and the conductivity of the conductor material, which is assumed to be uniform across the sample. The relative percent difference

in electrical resistance obtained between NFMM and four-point probe measurements is 14.7 % whereas the difference relative to simulations is 9.6 %. Noise measurements performed by recording Q for 60 min revealed that the signal to noise ratio on the Q measurement is 59.4 dB.

Additionally, simultaneous non-contact imaging of electrical conductivity (σ) and topography of a CB028 conductive trace is also presented in this chapter. The NFMM monitors the resonant frequency of the DR-based probe to acquire the surface topography, and the quality factor to determine the electrical conductivity. Conductivity and topography images of printed CB028 silver paste reveal an average roughness and conductivity of $1.1\mu\text{m}$ and 0.7e6 S/m , respectively. The NFMM data reveal significant and correlated variation in surface features and conductivity across the surface of the printed CB028 films. The topography and conductivity images obtained demonstrate that the NFMM can be employed for localized characterization of rough conductive materials used in microwave devices.

Finally, it was demonstrated that non-contact and non-destructive localized characterization of insulators and conductors coated by insulating polymer films is possible using the coaxial-resonator transmission line based NFMM. It was found that the NFMM is able to distinguish between different bulk dielectrics which are buried in an insulating layer whose thickness is on the order of the tip apex size. Investigation of the influence of the dielectric constant and thickness of the coating film on the sensitivity of the NFMM reveals that even for a high permittivity ($\epsilon'_r = 30$) coating layer, the NFMM is able to differentiate the buried insulating substrates using a tip with an apex radius of $10\mu\text{m}$. In addition, NFMM imaging of a flexible PDMS- $\text{Ba}_{0.55}\text{Sr}_{0.45}\text{TiO}_3$ composite coated with a $10\mu\text{m}$ thick parylene-C layer reveals concentration of low permittivity regions on one side of the sample. Signal-to-noise ratio of the F_r measurements using the coaxial resonator transmission line-based NFMM was measured using the same method employed by the DR-based NFMM and it was found to be 94.78 dB. Finally, subsurface imaging of a metallic gold trace coated with a $5\mu\text{m}$ thick parylene-C layer using tips of different radius shows that tips with larger size exhibit better sensitivity but reduced spatial resolution.

CHAPTER 7 : SUMMARY AND RECOMMENDATIONS

7.1 Summary

This work demonstrated that NFMM is a suitable technique that can be employed to characterize the surface and subsurface of materials. Two NFMM designs are developed and their materials differentiation and imaging capabilities are examined using bulk samples, liquids, additive manufactured materials and devices, and flexible polymer-ceramics. Each design offers advantages and disadvantages. The first design uses a DR-based probe resonating at 5.7 GHz as microwave probe. Advantages of this design are that it has high Q ($Q=986$) which enhances its materials differentiation capability, the probe tips can be easily replaced, and it is able to operate in non-contact form while characterizing conductive samples without the need of an additional distance sensor. The minimum resolvable difference in permittivity of bulk materials of the DR-based NFMM is $\Delta\epsilon'_r = 1.75$. It was found that $\Delta\epsilon'_r$ is enhanced to 0.04 if the probe tip is immersed in low-loss liquids. Additionally, it was found that the imaging capabilities of the NFMM are not degraded significantly when the tip immersed in a low-loss liquid. Additionally, the DR-based NFMM successfully imaged the topography and electrical conductivity of very rough CB028 thick films (average roughness= 3.8 μm). It was found that the electrical conductivity of CB028 varies between 0.4 MS/m to 1 MS/m. This measurement is of significance because it is performed in the microwave frequency regime and it is localized over a region close to the sample surface where less silver particles are observed and most of the surface current density is concentrated. The main disadvantage of this design is that imaging at constant height is only possible for conductive samples since the height control mechanism monitors the shift in the resonance frequency of the probe that occurs when the probe tip makes soft contact with a conductive sample.

The second NFMM employs a coaxial transmission line resonator-based microwave probe terminated in a chemically etched tungsten tip. An advantage of this design is that it is integrated with a quartz-tuning fork distance-following feedback system, which ensures non-contact imaging capability regardless of the sample's conductivity. Major challenges associated with contact between the tungsten tip and the quartz tuning fork are addressed and discussed. The coaxial transmission line resonator-based NFMM is able to differentiate between insulating bulk samples that are coated with insulating films whose thickness is about the size of the probe tip. Additionally, the microscope revealed permittivity variations of flexible PDMS-Ba_{0.55}Sr_{0.45}TiO₃ composite that is coated with a 10 µm thick parylene-C. A disadvantage of the coaxial transmission line resonator-based NFMM is its low Q (Q=55), however, higher Q can be achieved (Q= 196) if the quartz tuning fork is removed.

7.2 Recommendations

Suggestions for future work are:

- In NFMM, the extension of the evanescent fields in the material is controlled by the probe tip-sample distance and the probe-tip size. In Chapter 6, it was demonstrated that the coaxial resonator transmission line-based NFMM positioned at a distance of about 100 nm from the sample's surface is able to differentiate several insulating samples ($3.8 < \epsilon'_r < 25$) that are coated with an insulating layer ($2.95 < \epsilon'_r < 30$) as long as the thickness of the coating layer does not exceed the tip diameter. Thus, the depth of study of the NFMM can be controlled by actively controlling the probe tip size, which could be of interest for the characterization of multilayered devices.
- Develop a model of the electric field distribution between the NFMM probe tip and multilayered structures that can be used to extract the surface and subsurface material properties.

- The microwave probe along with the proximity sensor could be integrated with the printing tool in order to perform in-process characterization and quality control of additive manufactured devices.
- Examine the broadband operation of the coaxial transmission line resonator based-NFMM by studying the frequency response of additional resonances for different materials.
- Investigate mechanisms that enhance the quality factor of the coaxial transmission line resonator based-NFMM in order to improve its sensitivity, which can be done by depositing a film of gold onto the tungsten tip. This also will allow the tungsten tip be directly soldered to the copper inner conductor of the semi-rigid coaxial cable. Thus, the stainless steel tube used to hold the tungsten tip becomes unnecessary.

REFERENCES

- [1] M. D. Janezic and J. A. Jargon, "Complex permittivity determination from propagation constant measurements," *Microwave and Guided Wave Letters, IEEE*, vol. 9, pp. 76-78, 1999.
- [2] J. Hinojosa, "S-parameter broadband measurements on-coplanar and fast extraction of the substrate intrinsic properties," *Microwave and Wireless Components Letters, IEEE*, vol. 11, pp. 80-82, 2001.
- [3] A. Parkash, J. K. Vaid, and A. Mansingh, "Measurement of Dielectric Parameters at Microwave Frequencies by Cavity-Perturbation Technique," *Microwave Theory and Techniques, IEEE Transactions on*, vol. 27, pp. 791-795, 1979.
- [4] B. Meng, J. Booske, and R. Cooper, "Extended cavity perturbation technique to determine the complex permittivity of dielectric materials," *Microwave Theory and Techniques, IEEE Transactions on*, vol. 43, pp. 2633-2636, 1995.
- [5] D. Misra, "On the measurement of the complex permittivity of materials by an open-ended coaxial probe," *Microwave and Guided Wave Letters, IEEE*, vol. 5, pp. 161-163, 1995.
- [6] S. Anlage, V. Talanov, and A. Schwartz, "Principles of Near-Field Microwave Microscopy," in *Scanning Probe Microscopy*, S. Kalinin and A. Gruverman, Eds., ed: Springer New York, 2007, pp. 215-253.
- [7] C. Gao and X. D. Xiang, "Quantitative microwave near-field microscopy of dielectric properties," *Review of Scientific Instruments*, vol. 69, pp. 3846-3851, 1998.
- [8] A. Imtiaz, T. Baldwin, H. T. Nembach, T. M. Wallis, and P. Kabos, "Near-field microwave microscope measurements to characterize bulk material properties," *Applied Physics Letters*, vol. 90, pp. 243105-243105-3, 2007.
- [9] D. E. Steinhauer, C. P. Vlahacos, S. K. Dutta, F. C. Wellstood, and S. M. Anlage, "Surface resistance imaging with a scanning near-field microwave microscope," *Applied Physics Letters*, vol. 71, pp. 1736-1738, 1997.
- [10] L. Liu, Y. J. Feng, L. Y. Wu, Q. G. Liu, E. H. Zhao, Z. L. Fu, *et al.*, "Local microwave characterization of metal films using a scanning microwave near-field microscope," *Solid State Communications*, vol. 119, pp. 133-135, 7/17/ 2001.
- [11] S. Yun, S. Na, A. Babajayan, H. Kim, B. Friedman, and K. Lee, "Noncontact characterization of sheet resistance of indium–tin-oxide thin films by using a near-field microwave microprobe," *Thin Solid Films*, vol. 515, p. 4, 2006.
- [12] V. V. Talanov, A. Scherz, R. L. Moreland, and A. R. Schwartz, "Noncontact dielectric constant metrology of low-k interconnect films using a near-field scanned microwave probe," *Applied Physics Letters*, vol. 88, pp. 192906-192906-3, 2006.
- [13] V. V. Talanov, R. L. Moreland, A. Scherz, and A. R. Schwartz, "Novel Non-contact Dielectric Constant Metrology for Low-k Films," *AIP Conference Proceedings*, vol. 788, pp. 512-516, 2005.
- [14] J. H. Lee, S. Hyun, and K. Char, "Quantitative analysis of scanning microwave microscopy on dielectric thin film by finite element calculation," *Review of Scientific Instruments*, vol. 72, pp. 1425-1434, 2001.
- [15] D. E. Steinhauer, C. P. Vlahacos, F. C. Wellstood, S. M. Anlage, C. Canedy, R. Ramesh, *et al.*, "Quantitative imaging of dielectric permittivity and tunability with a near-field scanning microwave microscope," *Review of Scientific Instruments*, vol. 71, pp. 2751-2758, 2000.

- [16] D. E. Steinhauer, C. P. Vlahacos, S. K. Dutta, B. J. Feenstra, F. C. Wellstood, and S. M. Anlage, "Quantitative imaging of sheet resistance with a scanning near-field microwave microscope," *Applied Physics Letters*, vol. 72, pp. 861-863, 1998.
- [17] C. Gao, B. Hu, P. Zhang, M. Huang, W. Liu, and I. Takeuchi, "Quantitative microwave evanescent microscopy of dielectric thin films using a recursive image charge approach," *Applied Physics Letters*, vol. 84, pp. 4647-4649, 2004.
- [18] Y.-C. Chen, Y.-S. Hsieh, H.-F. Cheng, and I. N. Lin, "Study of Microwave Dielectric Properties of Perovskite Thin Films by Near-Field Microscopy," *J Electroceram*, vol. 13, pp. 261-265, 2004/07/01 2004.
- [19] D. E. Steinhauer, C. P. Vlahacos, F. C. Wellstood, S. M. Anlage, C. Canedy, R. Ramesh, *et al.*, "Imaging of microwave permittivity, tunability, and damage recovery in (Ba,Sr)TiO₃ thin films," *Applied Physics Letters*, vol. 75, pp. 3180-3182, 1999.
- [20] M. F. Cordoba-Erazo, E. A. Rojas-Nastrucci, and T. Weller, "Simultaneous RF electrical conductivity and topography mapping of smooth and rough conductive traces using microwave microscopy to identify localized variations," in *Wireless and Microwave Technology Conference (WAMICON), 2015 IEEE 16th Annual*, 2015, pp. 1-4.
- [21] J. O'Brien, M. F. Cordoba-Erazo, E. Rojas, J. Castro, M. Abdin, G. Mumcu, *et al.*, "Miniaturization of microwave components and antennas using 3D manufacturing," in *Antennas and Propagation (EuCAP), 2015 9th European Conference on*, 2015, pp. 1-4.
- [22] N. Arnal, T. Ketterl, Y. Vega, J. Stratton, C. Perkowski, P. Deffenbaugh, *et al.*, "3D multi-layer additive manufacturing of a 2.45 GHz RF front end," in *Microwave Symposium (IMS), 2015 IEEE MTT-S International*, 2015, pp. 1-4.
- [23] G. J. Vancso and H. Schoneherr, *Scanning force microscopy of polymers*. New York: Springer, 2010.
- [24] J. Castro, T. Weller, and J. Wang, "An improved fabrication method of high-k and low-loss polymer composites with sintered ceramic fillers for microwave applications," in *Microwave Symposium (IMS), 2015 IEEE MTT-S International*, 2015, pp. 1-4.
- [25] J. Castro, E. Rojas, T. Weller, and W. Jing, "High-k and low-loss polymer composites with co-fired Nd and Mg-Ca titanates for 3D RF and microwave printed devices: Fabrication and characterization," in *Wireless and Microwave Technology Conference (WAMICON), 2015 IEEE 16th Annual*, 2015, pp. 1-5.
- [26] M. M. Abdin, J. Castro, W. Jing, and T. Weller, "Miniaturized 3D printed balun using high-k composites," in *Wireless and Microwave Technology Conference (WAMICON), 2015 IEEE 16th Annual*, 2015, pp. 1-3.
- [27] C. Plassard, E. Bourillot, J. Rossignol, Y. Lacroute, E. Lepleux, L. Pacheco, *et al.*, "Detection of defects buried in metallic samples by scanning microwave microscopy," *Physical Review B*, vol. 83, p. 4, 2011.
- [28] J. D. Chisum and Z. Popovic, "Performance Limitations and Measurement Analysis of a Near-Field Microwave Microscope for Nondestructive and Subsurface Detection," *Microwave Theory and Techniques, IEEE Transactions on*, vol. 60, pp. 2605-2615, 2012.
- [29] L. You, C. A. Okoro, J. Ahn, J. Kopanski, R. R. Franklin, and O. Y. S., "Broadband Microwave-Based Metrology Platform Development: Demonstration of In-Situ Failure Mode Diagnostic Capabilities for Integrated Circuit Reliability Analyses," *ECS Journal of Solid State Science and Technology*, vol. 4, p. 5, 2015 2015.
- [30] A. Imtiaz, T. M. Wallis, S. H. Lim, H. Tanbakuchi, H. Huber, A. Hornung, *et al.*, "Frequency-selective contrast on variably doped p-type silicon with a scanning microwave microscope," *Journal of Applied Physics*, vol. 111, pp. 093727-093727-6, 2012.
- [31] A. Imtiaz and S. M. Anlage, "Effect of tip geometry on contrast and spatial resolution of the near-field microwave microscope," *Journal of Applied Physics*, vol. 100, pp. 044304-044304-8, 2006.

- [32] A. Imtiaz, S. M. Anlage, J. D. Barry, and J. Melngailis, "Nanometer-scale material contrast imaging with a near-field microwave microscope," *Applied Physics Letters*, vol. 90, pp. 143106-143106-3, 2007.
- [33] J. C. Weber, J. B. Schlager, N. A. Sanford, A. Imtiaz, T. M. Wallis, L. M. Mansfield, *et al.*, "A near-field scanning microwave microscope for characterization of inhomogeneous photovoltaics," *Review of Scientific Instruments*, vol. 83, p. 083702, 2012.
- [34] M. S. Kim, S. Kim, J. Kim, K. Lee, B. Friedman, J.-T. Kim, *et al.*, "Tip-sample distance control for near-field scanning microwave microscopes," *Review of Scientific Instruments*, vol. 74, pp. 3675-3678, 2003.
- [35] L. F. Chen, C. K. Ong, C. P. Neo, V. V. Varadan, and V. K. Varadan, *Microwave Electronics: Measurement and Materials Characterization*, 1 Edition ed.: Wiley, 2004.
- [36] E. A. Ash and G. Nicholls, "Super-resolution Aperture Scanning Microscope," *Nature*, vol. 237, p. 3, 1972.
- [37] M. Tabib-Azar, D.-P. Su, A. Pohar, S. R. LeClair, and G. Ponchak, "0.4 μm spatial resolution with 1 GHz ($\lambda=30\text{cm}$) evanescent microwave probe," *Review of Scientific Instruments*, vol. 70, pp. 1725-1729, 1999.
- [38] V. V. Talanov, A. Scherz, and A. R. Schwartz, "A Microfabricated Near-Field Scanned Microwave Probe for Noncontact Dielectric Constant Metrology of Low-k Films," in *Microwave Symposium Digest, 2006. IEEE MTT-S International*, 2006, pp. 1618-1621.
- [39] M. Tabib-Azar and W. Yaqiang, "Design and fabrication of scanning near-field microwave probes compatible with atomic force microscopy to image embedded nanostructures," *Microwave Theory and Techniques, IEEE Transactions on*, vol. 52, pp. 971-979, 2004.
- [40] C. A. Balanis, *Advanced Engineering Electromagnetics*: John Wiley & Sons, 1989.
- [41] A. Imtiaz, "Quantitative Materials Contrast at High Spatial Resolution With a Novel Near-Field Scanning Microwave Microscope " Ph.D., Physics, University of Maryland, 2005.
- [42] E. Abbe, "Beiträge zur Theorie des Mikroskops und der mikroskopischen Wahrnehmung," *Archiv f. mikrosk. Anatomie*, vol. 9, pp. 413-418, 1873/12/01 1873.
- [43] M. Tabib-Azar, N. S. Shoemaker, and S. Harris, "Non-destructive characterization of materials by evanescent microwaves," *Measurement Science and Technology*, vol. 4, 1993.
- [44] A. Karbassi, D. Ruf, A. D. Bettermann, C. A. Paulson, D. W. van der Weide, H. Tanbakuchi, *et al.*, "Quantitative scanning near-field microwave microscopy for thin film dielectric constant measurement," *Review of Scientific Instruments*, vol. 79, pp. -, 2008.
- [45] A. O. Oladipo, A. Lucibello, M. Kasper, S. Lavdas, G. M. Sardi, E. Proietti, *et al.*, "Analysis of a transmission mode scanning microwave microscope for subsurface imaging at the nanoscale," *Applied Physics Letters*, vol. 105, p. 133112, 2014.
- [46] J. A. Weiss and D. A. Hawks, "Dielectric Constant Evaluation of Insulating Materials: An Accurate, Practical Measurement System," in *Microwave Symposium Digest, 1987 IEEE MTT-S International*, 1987, pp. 457-460.
- [47] M. Tabib-Azar, P. S. Pathak, G. Ponchak, and S. LeClair, "Nondestructive superresolution imaging of defects and nonuniformities in metals, semiconductors, dielectrics, composites, and plants using evanescent microwaves," *Review of Scientific Instruments*, vol. 70, pp. 2783-2792, 1999.
- [48] Q. Zhang and P. J. McGinn, "Imaging of oxide dielectrics by near-field microwave microscopy," *Journal of the European Ceramic Society*, vol. 25, pp. 407-416, 4// 2005.
- [49] Z. N. Wing, J. W. Halloran, Q. Zhang, and P. J. McGinn, "Variable Dielectrics in the Calcium Magnesium Titanate System Characterized with Scanning Microwave Microscopy," *Journal of the American Ceramic Society*, vol. 89, pp. 1610-1614, 2006.
- [50] D. M. Ornoff, Y. Wang, and N. L. Allbritton, "Characterization of freestanding photoresist films for biological and MEMS applications," *Journal of Micromechanics and Microengineering*, vol. 23, p. 025009, 2013.

- [51] M. Tabib-Azar, D. P. Su, A. Pohar, S. R. LeClair, and G. Ponchak, "0.4 μm spatial resolution with 1 GHz ($\lambda=30\text{cm}$) evanescent microwave probe," *Review of Scientific Instruments*, vol. 70, pp. 1725-1729, 1999.
- [52] C. P. Vlahacos, D. E. Steinhauer, S. M. Anlage, and F. C. Wellstood, "Non-Contact Imaging of Dielectric Constant with a Near-Field Microwave Microscope," *Microscopy and Analysis*, p. 3, 2000.
- [53] F. M. Serry, "Scanning microwave microscope mode," *Agilent Application Note*, 2008.
- [54] H. Tanbakuchi, F. Kienberger, M. Richter, M. Dieudonne, M. Kasper, and G. Gramse, "Semiconductor Material and Device Characterization via Scanning Microwave Microscopy," in *Compound Semiconductor Integrated Circuit Symposium (CSICS), 2013 IEEE*, 2013, pp. 1-5.
- [55] H. P. Huber, I. Humer, M. Hochleitner, M. Fenner, M. Moertelmaier, C. Rankl, *et al.*, "Calibrated nanoscale dopant profiling using a scanning microwave microscope," *Journal of Applied Physics*, vol. 111, p. 014301, 2012.
- [56] M. Kasper, G. Gramse, J. Hoffmann, C. Gaquiere, R. Feger, A. Stelzer, *et al.*, "Metal-oxide-semiconductor capacitors and Schottky diodes studied with scanning microwave microscopy at 18 GHz," *Journal of Applied Physics*, vol. 116, p. 184301, 2014.
- [57] A. N. Reznik and V. V. Talanov, "Quantitative model for near-field scanning microwave microscopy: Application to metrology of thin film dielectrics," *Review of Scientific Instruments*, vol. 79, pp. 113708-113708-8, 2008.
- [58] Y. Qi, S. M. Anlage, H. Zheng, and R. Ramesh, "Local dielectric measurements of BaTiO₃-CoFe₂O₄ nanocomposites through microwave microscopy," *Journal of Materials Research*, vol. 22, p. 7, 2007.
- [59] Z. Wu, A. D. Souza, B. Peng, W. Q. Sun, S. Y. Xu, and C. K. Ong, "Measurement of high frequency conductivity of oxide-doped anti-ferromagnetic thin film with a near-field scanning microwave microscope," *AIP Advances*, vol. 4, p. 047114, 2014.
- [60] Y. Qi, S. M. Anlage, H. Zheng, and R. Ramesh, "Local dielectric measurements of BaTiO₃-CoFe₂O₄ nanocomposites through microwave microscopy," *Journal of Materials Research*, vol. 22, pp. 1193-1199, 2007.
- [61] K. Haddadi, H. Bakli, and T. Lasri, "Microwave Liquid Sensing Based on Interferometry and Microscopy Techniques," *Microwave and Wireless Components Letters, IEEE*, vol. 22, pp. 542-544, 2012.
- [62] J. Park, S. Hyun, A. Kim, T. Kim, and K. Char, "Observation of biological samples using a scanning microwave microscope," *Ultramicroscopy*, vol. 102, p. 6, 2005.
- [63] M. Farina, A. Di Donato, D. Mencarelli, G. Venanzoni, and A. Morini, "High Resolution Scanning Microwave Microscopy for Applications in Liquid Environment," *Microwave and Wireless Components Letters, IEEE*, vol. 22, pp. 595-597, 2012.
- [64] K. Haddadi, D. Glay, and T. Lasri, "A 60 Ghz Scanning Near-Field Microscope With High Spatial Resolution Sub-Surface Imaging," *Microwave and Wireless Components Letters, IEEE*, vol. 21, pp. 625-627, 2011.
- [65] R. Zhao, M. S. Boybay, and O. M. Ramahi, "Metamaterial inspired probe for noninvasive near-field subsurface sensing," in *Antennas and Propagation Society International Symposium (APSURSI), 2010 IEEE*, 2010, pp. 1-4.
- [66] C. Gao, F. Duewer, and X. D. Xiang, "Quantitative microwave evanescent microscopy," *Applied Physics Letters*, vol. 75, pp. 3005-3007, 1999.
- [67] D. M. Pozar, *Microwave Engineering*: John Wiley & Sons, 2005.
- [68] P. J. Petersan and S. M. Anlage, "Measurement of resonant frequency and quality factor of microwave resonators: Comparison of methods," *Journal of Applied Physics*, vol. 84, pp. 3392-3402, 1998.
- [69] L. A. Trinogga, G. Kaizhou, and H. I. C, *Practical Microstrip Circuit Design*. England: Ellis Horwood Limited, 1991.
- [70] D. kajfez and P. Guillon, *Dielectric Resonators*, 1986.

- [71] M. Tabib-Azar, D. Akinwande, G. Ponchak, and S. R. LeClair, "Novel physical sensors using evanescent microwave probes," *Review of Scientific Instruments*, vol. 70, pp. 3381-3386, 1999.
- [72] J. Kim, K. Lee, B. Friedman, and D. Cha, "Near-field scanning microwave microscope using a dielectric resonator," *Applied Physics Letters*, vol. 83, pp. 1032-1034, 2003.
- [73] S. Kim, H. Yoo, K. Lee, B. Friedman, M. A. Gaspar, and R. Levicky, "Distance control for a near-field scanning microwave microscope in liquid using a quartz tuning fork," *Applied Physics Letters*, vol. 86, p. 153506, 2005.
- [74] A. Tselev, S. M. Anlage, Z. Ma, and J. Melngailis, "Broadband dielectric microwave microscopy on micron length scales," *Review of Scientific Instruments*, vol. 78, pp. 044701-044701-7, 2007.
- [75] R. A. Kleismit, M. K. Kazimierczuk, and G. Kozlowski, "Sensitivity and resolution of evanescent microwave microscope," *Microwave Theory and Techniques, IEEE Transactions on*, vol. 54, pp. 639-647, 2006.
- [76] A. Khanna and Y. Garault, "Determination of Loaded, Unloaded, and External Quality Factors of a Dielectric Resonator Coupled to a Microstrip Line," *Microwave Theory and Techniques, IEEE Transactions on*, vol. 31, pp. 261-264, 1983.
- [77] K. Karrai and R. D. Grober, "Piezoelectric tip-sample distance control for near field optical microscopes," *Applied Physics Letters*, vol. 66, pp. 1842-1844, 1995.
- [78] Y. Qin and R. Reifenberger, "Calibrating a tuning fork for use as a scanning probe microscope force sensor," *Review of Scientific Instruments*, vol. 78, p. 063704, 2007.
- [79] R. D. Grober, J. Acimovic, J. Schuck, D. Hessman, P. J. Kindlemann, J. Hespanha, *et al.*, "Fundamental limits to force detection using quartz tuning forks," *Review of Scientific Instruments*, vol. 71, pp. 2776-2780, 2000.
- [80] P. Mühlshlegel, J. Toquant, D. W. Pohl, and B. Hecht, "Glue-free tuning fork shear-force microscope," *Review of Scientific Instruments*, vol. 77, pp. -, 2006.
- [81] A. Crottini, J. L. Staehli, B. Deveaud, X. L. Wang, and M. Ogura, "Ultra stable tuning fork sensor for low-temperature near-field spectroscopy," *Ultramicroscopy*, vol. 90, pp. 97-101, Feb 2001.
- [82] D.-I. Kim and H.-S. Ahn, "Etching voltage control technique for electrochemical fabrication of scanning probe microscope tips," *Review of Scientific Instruments*, vol. 73, pp. 1337-1339, 2002.
- [83] B.-F. Ju, Y.-L. Chen, and Y. Ge, "The art of electrochemical etching for preparing tungsten probes with controllable tip profile and characteristic parameters," *Review of Scientific Instruments*, vol. 82, p. 013707, 2011.
- [84] W.-T. Chang, I.-S. Hwang, M.-T. Chang, C.-Y. Lin, W.-H. Hsu, and J.-L. Hou, "Method of electrochemical etching of tungsten tips with controllable profiles," *Review of Scientific Instruments*, vol. 83, p. 083704, 2012.
- [85] S. Morishita and F. Okuyama, "Sharpening of monocrystalline molybdenum tips by means of inert-gas ion sputtering," *Journal of Vacuum Science & Technology A*, vol. 9, pp. 167-169, 1991.
- [86] H. S. Kim, M. L. Yu, U. Staufer, L. P. Muray, D. P. Kern, and T. H. P. Chang, "Oxygen processed field emission tips for microcolumn applications," *Journal of Vacuum Science & Technology B*, vol. 11, pp. 2327-2331, 1993.
- [87] J. P. Ibe, P. P. Bey, S. L. Brandow, R. A. Brizzolara, N. A. Burnham, D. P. DiLella, *et al.*, "On the electrochemical etching of tips for scanning tunneling microscopy," *Journal of Vacuum Science & Technology A*, vol. 8, pp. 3570-3575, 1990.
- [88] Y.-G. Kim, E.-H. Choi, S.-O. Kang, and G. Cho, "Computer-controlled fabrication of ultra-sharp tungsten tips," *Journal of Vacuum Science & Technology B*, vol. 16, pp. 2079-2081, 1998.
- [89] E. Ernst, "Optimisation of the preparation process for tips used in scanning tunneling microscopy," *Physics, Technische Universität Dresden*, 2006.
- [90] M. C. Labs. <http://www.madcitylabs.com/madpll.html>.
- [91] M. F. Cordoba-Erazo and T. M. Weller, "Liquids characterization using a dielectric resonator-based microwave probe," in *Microwave Conference (EuMC), 2012 42nd European*, 2012, pp. 655-658.

- [92] C. P. Vlahacos, R. C. Black, S. M. Anlage, A. Amar, and F. C. Wellstood, "Near-field scanning microwave microscope with 100 μm resolution," *Applied Physics Letters*, vol. 69, pp. 3272-3274, 1996.
- [93] S. Botao, R. Weerasekera, A. T. Woldegiorgis, Z. Li-Rong, L. Ran, and W. Zapka, "High frequency characterization and modelling of inkjet printed interconnects on flexible substrate for low-cost RFID applications," in *Electronics System-Integration Technology Conference, 2008. ESTC 2008. 2nd*, 2008, pp. 695-700.
- [94] Y. Li and M. M. Tentzeris, "Design and Characterization of Novel Paper-based Inkjet-Printed RFID and Microwave Structures for Telecommunication and Sensing Applications," in *Microwave Symposium, 2007. IEEE/MTT-S International*, 2007, pp. 1633-1636.
- [95] S. Koulouridis, G. Kiziltas, Z. Yijun, D. J. Hansford, and J. L. Volakis, "Polymer-Ceramic Composites for Microwave Applications: Fabrication and Performance Assessment," *Microwave Theory and Techniques, IEEE Transactions on*, vol. 54, pp. 4202-4208, 2006.
- [96] V. T. Tung, S.A. Chizhik, T. X. Hoai, N. T. Tinh, and V. V. Chikunov, in *Scanning Probe Microscopy*, ed: In Tech, 2012.
- [97] M. F. Cordoba-Erazo and T. M. Weller, "Noncontact Electrical Characterization of Printed Resistors Using Microwave Microscopy," *Instrumentation and Measurement, IEEE Transactions on*, vol. 64, pp. 509-515, 2015.
- [98] "Carbon Conductor 7082 Technical Datasheet," DuPont, Ed., ed, 2012.
- [99] J. S. Bendat and A. G. Piersol, *Random Data: Analysis and Measurement Procedures*: Wiley, 2010.
- [100] P. I. G. Co. (2008). *M-110 · M-111· M-112 Compact Micro-Translation Stage-Datasheet*. Available: http://www.physikinstrumente.com/en/pdf/M110_Datasheet.pdf
- [101] J. C. Lotters, W. Olthuis, P. H. Veltink, and P. Bergveld, "The mechanical properties of the rubber elastic polymer polydimethylsiloxane for sensor applications," *Journal of Micromechanics and Microengineering*, p. 3, 1997.
- [102] H.-s. Noh, K.-s. Moon, A. Cannon, P. J. Hesketh, and C. P. Wong, "Wafer bonding using microwave heating of parylene intermediate layers," *Journal of Micromechanics and Microengineering*, vol. 14, p. 625, 2004.
- [103] N. J. Farcich, J. Salonen, and P. M. Asbeck, "Single-Length Method Used to Determine the Dielectric Constant of Polydimethylsiloxane," *Microwave Theory and Techniques, IEEE Transactions on*, vol. 56, pp. 2963-2971, 2008.
- [104] F. E. M. Systems, "Datasheet: Barium Strontium Titanate (BST) Additive/Dielectric Material," ed, 2009.
- [105] D.-H. Yoon, J. Zhang, and B. I. Lee, "Dielectric constant and mixing model of BaTiO₃ composite thick films," *Materials Research Bulletin*, vol. 38, pp. 765-772, 4/30/ 2003.
- [106] J. Catro, E. A. Rojas-Nastrucci, A. Perez, T. Weller, and J. Wang, "Enhancement of Microwave Dielectric Properties of Polymer-Ceramic Composites with MgCaTiO₂ and TiO₂ Micro-fillers through a High-Temperature Sintering Process," *Journal of American Ceramic Society*, Submitted

APPENDIX A: COPYRIGHT PERMISSIONS

A.1 Permissions for Chapter 1

LABORATOIRE D'ELECTROMAGNETISME ET D'ACOUSTIQUE

EPFL-STI-LEMA
Prof. Juan R. Mosig
Bât ELB, Station 11
CH 1015 Lausanne Switzerland

Phone : +4121 693 4628/2669
Fax : +4121 693 26 73
E-mail : Juan.Mosig@epfl.ch
Web site : http://lema.epfl.ch



Maria F. Cordoba-Erazo
Department of Electrical Engineering
University of South Florida
4202 East Fowler Ave. ENB 412
Tampa, FL 33620 USA

Lausanne, May 22, 2015

Dear Ms Cordoba-Erazo,

With this message and on behalf of EurAAP/EuCAP, I am granting you copyright permission for using the material referenced here below published in the EuCAP'2015 Conference for your PhD thesis.

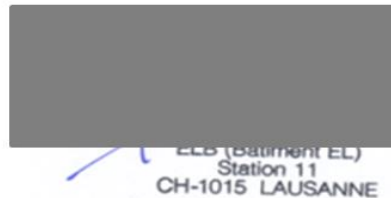
The original EuCAP papers must be acknowledged (or cited, if they are given in a list of references). When figures from EuCAP papers are used the following statement must appear in the figures' captions: "Taken from [*]; copyright EurAAP; used with permission".**

Although copyright for EuCAP papers belongs to EurAAP/EuCAP, we always strongly advise the applicants of an EuCAP copyright permission to inform by courtesy all the authors of the concerned papers. This is your personal responsibility and duty.

Yours sincerely,

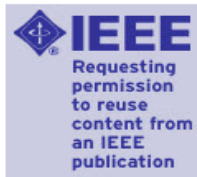
Prof. Juan Mosig,

Chair of the EurAAP Board



CONCERNED MATERIAL.

Fig. 1. "Fabricated model of sinuous cavity-backed PSA antenna" of the paper
Miniaturization of microwave components and antennas using 3D manufacturing
Published in: 9th European Conference on Antennas and Propagation (EuCAP), 13-17 April 2015



Title: 3D multi-layer additive manufacturing of a 2.45 GHz RF front end

Conference Proceedings: Microwave Symposium (IMS), 2015 IEEE MTT-S International

Author: Arnal, N.; Ketterl, T.; Vega, Y.; Stratton, J.; Perkowski, C.; Deffenbaugh, P.; Church, K.; Weller, T.

Publisher: IEEE

Date: 17-22 May 2015

Copyright © 2015, IEEE

[LOGIN](#)

If you're a [copyright.com](#) user, you can login to RightsLink using your [copyright.com](#) credentials. Already a [RightsLink](#) user or want to [learn more?](#)

Thesis / Dissertation Reuse

The IEEE does not require individuals working on a thesis to obtain a formal reuse license, however, you may print out this statement to be used as a permission grant:

Requirements to be followed when using any portion (e.g., figure, graph, table, or textual material) of an IEEE copyrighted paper in a thesis:

- 1) In the case of textual material (e.g., using short quotes or referring to the work within these papers) users must give full credit to the original source (author, paper, publication) followed by the IEEE copyright line © 2011 IEEE.
- 2) In the case of illustrations or tabular material, we require that the copyright line © [Year of original publication] IEEE appear prominently with each reprinted figure and/or table.
- 3) If a substantial portion of the original paper is to be used, and if you are not the senior author, also obtain the senior author's approval.

Requirements to be followed when using an entire IEEE copyrighted paper in a thesis:

- 1) The following IEEE copyright/ credit notice should be placed prominently in the references: © [year of original publication] IEEE. Reprinted, with permission, from [author names, paper title, IEEE publication title, and month/year of publication]
- 2) Only the accepted version of an IEEE copyrighted paper can be used when posting the paper or your thesis on-line.
- 3) In placing the thesis on the author's university website, please display the following message in a prominent place on the website: In reference to IEEE copyrighted material which is used with permission in this thesis, the IEEE does not endorse any of [university/educational entity's name goes here]'s products or services. Internal or personal use of this material is permitted. If interested in reprinting/republishing IEEE copyrighted material for advertising or promotional purposes or for creating new collective works for resale or redistribution, please go to http://www.ieee.org/publications_standards/publications/rights/rights_link.html to learn how to obtain a License from RightsLink.

If applicable, University Microfilms and/or ProQuest Library, or the Archives of Canada may supply single copies of the dissertation.

[BACK](#)
[CLOSE WINDOW](#)



Title: High-k and low-loss polymer composites with co-fired Nd and Mg-Ca titanates for 3D RF and microwave printed devices: Fabrication and characterization

Conference Proceedings: Wireless and Microwave Technology Conference (WAMICON), 2015 IEEE 16th Annual

Author: Castro, J.; Rojas, E.; Weller, T.; Jing Wang

Publisher: IEEE

Date: 13-15 April 2015

Copyright © 2015, IEEE

[LOGIN](#)

If you're a [copyright.com](#) user, you can login to RightsLink using your [copyright.com](#) credentials. Already a [RightsLink](#) user or want to [learn more?](#)

Thesis / Dissertation Reuse

The IEEE does not require individuals working on a thesis to obtain a formal reuse license, however, you may print out this statement to be used as a permission grant:

Requirements to be followed when using any portion (e.g., figure, graph, table, or textual material) of an IEEE copyrighted paper in a thesis:

- 1) In the case of textual material (e.g., using short quotes or referring to the work within these papers) users must give full credit to the original source (author, paper, publication) followed by the IEEE copyright line © 2011 IEEE.
- 2) In the case of illustrations or tabular material, we require that the copyright line © [Year of original publication] IEEE appear prominently with each reprinted figure and/or table.
- 3) If a substantial portion of the original paper is to be used, and if you are not the senior author, also obtain the senior author's approval.

Requirements to be followed when using an entire IEEE copyrighted paper in a thesis:

- 1) The following IEEE copyright/ credit notice should be placed prominently in the references: © [year of original publication] IEEE. Reprinted, with permission, from [author names, paper title, IEEE publication title, and month/year of publication]
- 2) Only the accepted version of an IEEE copyrighted paper can be used when posting the paper or your thesis on-line.
- 3) In placing the thesis on the author's university website, please display the following message in a prominent place on the website: In reference to IEEE copyrighted material which is used with permission in this thesis, the IEEE does not endorse any of [university/educational entity's name goes here]'s products or services. Internal or personal use of this material is permitted. If interested in reprinting/republishing IEEE copyrighted material for advertising or promotional purposes or for creating new collective works for resale or redistribution, please go to http://www.ieee.org/publications_standards/publications/rights/rights_link.html to learn how to obtain a License from RightsLink.

If applicable, University Microfilms and/or ProQuest Library, or the Archives of Canada may supply single copies of the dissertation.

[BACK](#)
[CLOSE WINDOW](#)



Title: Miniaturized 3D printed balun using high-k composites

Conference Proceedings: Wireless and Microwave Technology Conference (WAMICON), 2015 IEEE 16th Annual

Author: Abdin, M.M.; Castro, J.; Jing Wang; Weller, T.

Publisher: IEEE

Date: 13-15 April 2015

Copyright © 2015, IEEE

[LOGIN](#)

If you're a [copyright.com](#) user, you can login to RightsLink using your [copyright.com](#) credentials. Already a [RightsLink](#) user or want to [learn more?](#)

Thesis / Dissertation Reuse

The IEEE does not require individuals working on a thesis to obtain a formal reuse license, however, you may print out this statement to be used as a permission grant:

Requirements to be followed when using any portion (e.g., figure, graph, table, or textual material) of an IEEE copyrighted paper in a thesis:

- 1) In the case of textual material (e.g., using short quotes or referring to the work within these papers) users must give full credit to the original source (author, paper, publication) followed by the IEEE copyright line © 2011 IEEE.
- 2) In the case of illustrations or tabular material, we require that the copyright line © [Year of original publication] IEEE appear prominently with each reprinted figure and/or table.
- 3) If a substantial portion of the original paper is to be used, and if you are not the senior author, also obtain the senior author's approval.



Requirements to be followed when using an entire IEEE copyrighted paper in a thesis:

- 1) The following IEEE copyright/ credit notice should be placed prominently in the references: © [year of original publication] IEEE. Reprinted, with permission, from [author names, paper title, IEEE publication title, and month/year of publication]
- 2) Only the accepted version of an IEEE copyrighted paper can be used when posting the paper or your thesis on-line.
- 3) In placing the thesis on the author's university website, please display the following message in a prominent place on the website: In reference to IEEE copyrighted material which is used with permission in this thesis, the IEEE does not endorse any of [university/educational entity's name goes here]'s products or services. Internal or personal use of this material is permitted. If interested in reprinting/republishing IEEE copyrighted material for advertising or promotional purposes or for creating new collective works for resale or redistribution, please go to http://www.ieee.org/publications_standards/publications/rights/rights_link.html to learn how to obtain a License from RightsLink.


If applicable, University Microfilms and/or ProQuest Library, or the Archives of Canada may supply single copies of the dissertation.

[BACK](#)
[CLOSE WINDOW](#)

A.2 Permissions for Chapter 2



[Home](#) [Account Info](#) [Help](#) [Live Chat](#)



Title: Nondestructive superresolution imaging of defects and nonuniformities in metals, semiconductors, dielectrics, composites, and plants using evanescent microwaves

Author: M. Tabib-Azar, P. S. Pathak, G. Ponchak, et al.

Publication: Review of Scientific Instruments

Volume/Issue: 70/6

Publisher: AIP Publishing LLC

Date: Jun 1, 1999

Page Count: 10

Rights managed by AIP Publishing LLC.

Logged in as:
Maria Cordoba

[LOGOUT](#)

Order Completed

Thank you very much for your order.

Click [here](#) for Payment Terms and Conditions.

[Get a printable version for your records.](#)

License Number	3724261306815
Order Date	Oct 08, 2015
Publisher	AIP Publishing LLC
Publication	Review of Scientific Instruments
Article Title	Nondestructive superresolution imaging of defects and nonuniformities in metals, semiconductors, dielectrics, composites, and plants using evanescent microwaves
Author	M. Tabib-Azar, P. S. Pathak, G. Ponchak, et al.
Online Publication Date	Jun 1, 1999
Volume number	70
Issue number	6
Type of Use	Thesis/Dissertation
Requestor type	Student
Format	Electronic
Portion	Figure/Table
Number of figures/tables	2
Title of your thesis / dissertation	Near-field Microwave Microscopy for Surface and Subsurface Characterization of Materials
Expected completion date	Dec 2015
Estimated size (number of pages)	130
Total	0.00 USD

[ORDER MORE...](#) [CLOSE WINDOW](#)

Copyright © 2015 [Copyright Clearance Center, Inc.](#) All Rights Reserved. [Privacy statement](#). [Terms and Conditions](#).
Comments? We would like to hear from you. E-mail us at customercare@copyright.com



Title: Quantitative microwave near-field microscopy of dielectric properties
Author: C. Gao,X.-D. Xiang
Publication: Review of Scientific Instruments
Volume/Issue 69/11
Publisher: AIP Publishing LLC
Date: Nov 1, 1998
Page Count: 6
 Rights managed by AIP Publishing LLC.

Logged in as:

Maria Cordoba

LOGOUT

Order Completed

Thank you very much for your order.

Click [here](#) for Payment Terms and Conditions.

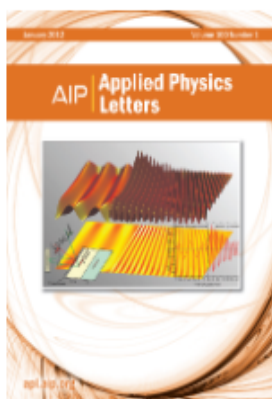
[Get a printable version for your records.](#)

License Number	3724270095006
Order Date	Oct 08, 2015
Publisher	AIP Publishing LLC
Publication	Review of Scientific Instruments
Article Title	Quantitative microwave near-field microscopy of dielectric properties
Author	C. Gao,X.-D. Xiang
Online Publication Date	Nov 1, 1998
Volume number	69
Issue number	11
Type of Use	Thesis/Dissertation
Requestor type	Student
Format	Electronic
Portion	Figure/Table
Number of figures/tables	1
Title of your thesis / dissertation	Near-field Microwave Microscopy for Surface and Subsurface Characterization of Materials
Expected completion date	Dec 2015
Estimated size (number of pages)	130
Total	0.00 USD

ORDER MORE...

CLOSE WINDOW

Copyright © 2015 Copyright Clearance Center, Inc. All Rights Reserved. [Privacy statement](#). [Terms and Conditions](#).
 Comments? We would like to hear from you. E-mail us at customercare@copyright.com



Title: Quantitative imaging of sheet resistance with a scanning near-field microwave microscope

Author: D. E. Steinhauer, C. P. Vlahacos, S. K. Dutta, et al.

Publication: Applied Physics Letters

Volume/Issue: 72/7

Publisher: AIP Publishing LLC

Date: Feb 16, 1998

Page Count: 3

Rights managed by AIP Publishing LLC.

Logged in as:

Maria Cordoba

LOGOUT

Order Completed

Thank you very much for your order.

Click [here](#) for Payment Terms and Conditions.

[Get a printable version for your records.](#)

License Number	3724270216010
Order Date	Oct 08, 2015
Publisher	AIP Publishing LLC
Publication	Applied Physics Letters
Article Title	Quantitative imaging of sheet resistance with a scanning near-field microwave microscope
Author	D. E. Steinhauer, C. P. Vlahacos, S. K. Dutta, et al.
Online Publication Date	Feb 16, 1998
Volume number	72
Issue number	7
Type of Use	Thesis/Dissertation
Requestor type	Student
Format	Electronic
Portion	Figure/Table
Number of figures/tables	2
Title of your thesis / dissertation	Near-field Microwave Microscopy for Surface and Subsurface Characterization of Materials
Expected completion date	Dec 2015
Estimated size (number of pages)	130
Total	0.00 USD

ORDER MORE...

CLOSE WINDOW

Copyright © 2015 Copyright Clearance Center, Inc. All Rights Reserved. [Privacy statement](#). [Terms and Conditions](#). Comments? We would like to hear from you. E-mail us at customer@copyright.com



Title: Detection of defects buried in metallic samples by scanning microwave microscopy
Author: C. Plassard et al.
Publication: Physical Review B
Publisher: American Physical Society
Date: Mar 28, 2011
 ©2011 American Physical Society

Logged in as:
 Maria Cordoba

[LOGOUT](#)

Order Completed

Thank you very much for your order.

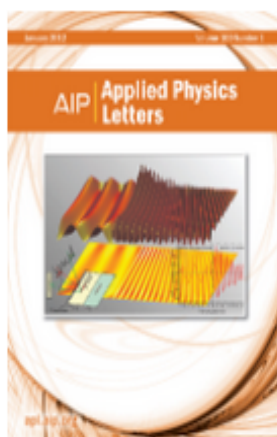
This is a License Agreement between Maria Cordoba ("You") and American Physical Society. The license consists of your order details, the terms and conditions provided by American Physical Society, and the [payment terms and conditions](#).

[Get the printable license.](#)

License Number	3724270554626
License date	Oct 08, 2015
Licensed content publisher	American Physical Society
Licensed content publication	Physical Review B
Licensed content title	Detection of defects buried in metallic samples by scanning microwave microscopy
Licensed copyright line	©2011 American Physical Society
Licensed content author	C. Plassard et al.
Licensed content date	Mar 28, 2011
Volume number	83
Type of use	Thesis/Dissertation
Requestor type	Student
Format	Electronic
Portion	chart/graph/table/figure
Number of charts/graphs/tables/figures	1
Portion description	FIG. 3. (Color online) Three-dimensional tomographic image of the metal sample according to the frequency.
Rights for	Main product
Duration of use	Life of current edition
Creation of copies for the disabled	no
With minor editing privileges	no
For distribution to	Worldwide
In the following language(s)	Original language of publication
With incidental promotional use	no
Lifetime unit quantity of new product	0 to 499
The requesting person/organization	Maria Cordoba, University of South Florida
Order reference number	None
Title of your thesis / dissertation	Near-field Microwave Microscopy for Surface and Subsurface Characterization of Materials
Expected completion date	Dec 2015
Expected size (number of pages)	130
Total	0.00 USD

[ORDER MORE...](#)
[CLOSE WINDOW](#)

Copyright © 2015 Copyright Clearance Center, Inc. All Rights Reserved. [Privacy statement](#). [Terms and Conditions](#).
 Comments? We would like to hear from you. E-mail us at customer@copyright.com



Title: Analysis of a transmission mode scanning microwave microscope for subsurface imaging at the nanoscale
Author: A. O. Oladipo, A. Lucibello, M. Kasper, et al.
Publication: Applied Physics Letters
Volume/Issue: 105/13
Publisher: AIP Publishing LLC
Date: Oct 2, 2014
Page Count: 4
Rights managed by AIP Publishing LLC.

Logged in as:
Maria Cordoba

LOGOUT

Order Completed

Thank you very much for your order.

Click [here](#) for Payment Terms and Conditions.

[Get a printable version for your records.](#)

License Number	3724270725600
Order Date	Oct 08, 2015
Publisher	AIP Publishing LLC
Publication	Applied Physics Letters
Article Title	Analysis of a transmission mode scanning microwave microscope for subsurface imaging at the nanoscale
Author	A. O. Oladipo, A. Lucibello, M. Kasper, et al.
Online Publication Date	Oct 2, 2014
Volume number	105
Issue number	13
Type of Use	Thesis/Dissertation
Requestor type	Student
Format	Electronic
Portion	Figure/Table
Number of figures/tables	1
Title of your thesis / dissertation	Near-field Microwave Microscopy for Surface and Subsurface Characterization of Materials
Expected completion date	Dec 2015
Estimated size (number of pages)	130
Total	0.00 USD

ORDER MORE...

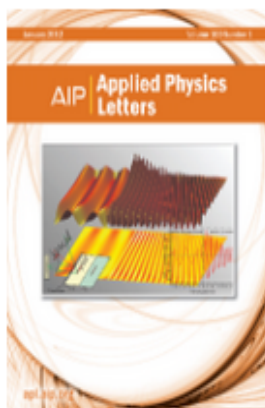
CLOSE WINDOW

Copyright © 2015 Copyright Clearance Center, Inc. All Rights Reserved. [Privacy statement](#), [Terms and Conditions](#).
Comments? We would like to hear from you. E-mail us at customercare@copyright.com

A.3 Permissions for Chapter 3



RightsLink®

[Home](#)[Account Info](#)[Help](#)

Title: Near-field scanning microwave microscope using a dielectric resonator

Author: Jooyoung Kim, Kiejin Lee, Barry Friedman, et al.

Publication: Applied Physics Letters

Volume/Issue: 83/5

Publisher: AIP Publishing LLC

Date: Jul 30, 2003

Page Count: 3

Rights managed by AIP Publishing LLC.

Logged in as:

Maria Cordoba

[LOGOUT](#)

Order Completed

Thank you very much for your order.

Click [here](#) for Payment Terms and Conditions.

[Get a printable version for your records.](#)

License Number	3724270997631
Order Date	Oct 08, 2015
Publisher	AIP Publishing LLC
Publication	Applied Physics Letters
Article Title	Near-field scanning microwave microscope using a dielectric resonator
Author	Jooyoung Kim, Kiejin Lee, Barry Friedman, et al.
Online Publication Date	Jul 30, 2003
Volume number	83
Issue number	5
Type of Use	Thesis/Dissertation
Requestor type	Student
Format	Electronic
Portion	Figure/Table
Number of figures/tables	1
Title of your thesis / dissertation	Near-field Microwave Microscopy for Surface and Subsurface Characterization of Materials
Expected completion date	Dec 2015
Estimated size (number of pages)	130
Total	0.00 USD

[ORDER MORE...](#)[CLOSE WINDOW](#)

Copyright © 2015 Copyright Clearance Center, Inc. All Rights Reserved. [Privacy statement](#). [Terms and Conditions](#).
Comments? We would like to hear from you. E-mail us at customercare@copyright.com

A.4 Permission to Use Miscellaneous Materials from Previous Publication in European Microwave Conference Included in Chapter 5



Prof. A. Vander Vorst
Rue Louis de Geer 6
B-1348 Louvain-la-Neuve
Belgium
vandervorst@eumwa.org

TO WHOM IT MAY CONCERN

Louvain-la-Neuve, October 09, 2015

On behalf of **EuMA**, the European Microwave Association, Prof. André VANDER VORST is granting Ms. Maria F. CORDOBA-ERAZO to use extensive material, including figures and tables of the paper by M.F. Cordoba-Erazo, T.W. Weller, « Liquids characterization using a dielectric resonator-based microwave probe », *Proc. 42nd European Microwave Conference*, pp. 655-658, Amsterdam, The Netherlands, October 2012, in her doctoral dissertation at University of South Florida, USA. This permission is granted on condition that the source of the material, including authors, date and copyright owner are acknowledged, the copyright owner being the European Microwave Association, **EuMA**.



EuMA Secretary-Treasurer

A.5 Permission to Use Miscellaneous Materials from Previous IEEE Publications Included in

Chapter 6



[Home](#) [Account Info](#) [Help](#)  [Live Chat](#)



Requesting permission to reuse content from an IEEE publication

Title: Noncontact Electrical Characterization of Printed Resistors Using Microwave Microscopy

Author: Cordoba-Erazo, M.F.; Weller, T.M.

Publication: Instrumentation and Measurement, IEEE Transactions on

Publisher: IEEE

Date: Feb. 2015

Copyright © 2015, IEEE

Logged in as:
Maria Cordoba

[LOGOUT](#)

Thesis / Dissertation Reuse

The IEEE does not require individuals working on a thesis to obtain a formal reuse license, however, you may print out this statement to be used as a permission grant:

Requirements to be followed when using any portion (e.g., figure, graph, table, or textual material) of an IEEE copyrighted paper in a thesis:

- 1) In the case of textual material (e.g., using short quotes or referring to the work within these papers) users must give full credit to the original source (author, paper, publication) followed by the IEEE copyright line © 2011 IEEE.
- 2) In the case of illustrations or tabular material, we require that the copyright line © [Year of original publication] IEEE appear prominently with each reprinted figure and/or table.
- 3) If a substantial portion of the original paper is to be used, and if you are not the senior author, also obtain the senior author's approval.

Requirements to be followed when using an entire IEEE copyrighted paper in a thesis:

- 1) The following IEEE copyright/ credit notice should be placed prominently in the references: © [year of original publication] IEEE. Reprinted, with permission, from [author names, paper title, IEEE publication title, and month/year of publication]
- 2) Only the accepted version of an IEEE copyrighted paper can be used when posting the paper or your thesis on-line.
- 3) In placing the thesis on the author's university website, please display the following message in a prominent place on the website: In reference to IEEE copyrighted material which is used with permission in this thesis, the IEEE does not endorse any of [university/educational entity's name goes here]'s products or services. Internal or personal use of this material is permitted. If interested in reprinting/republishing IEEE copyrighted material for advertising or promotional purposes or for creating new collective works for resale or redistribution, please go to http://www.ieee.org/publications_standards/publications/rights/rights_link.html to learn how to obtain a License from RightsLink.

If applicable, University Microfilms and/or ProQuest Library, or the Archives of Canada may supply single copies of the dissertation.

[BACK](#)

[CLOSE WINDOW](#)

Copyright © 2015 Copyright Clearance Center, Inc. All Rights Reserved. [Privacy statement](#). [Terms and Conditions](#).
Comments? We would like to hear from you. E-mail us at customercare@copyright.com



Title: Simultaneous RF electrical conductivity and topography mapping of smooth and rough conductive traces using microwave microscopy to identify localized variations

Conference Proceedings: Wireless and Microwave Technology Conference (WAMICON), 2015 IEEE 16th Annual

Author: Cordoba-Erazo, M.F.; Rojas-Nastrucci, E.A.; Weller, T.

Publisher: IEEE

Date: 13-15 April 2015

Copyright © 2015, IEEE

Logged in as:
Maria Cordoba

[LOGOUT](#)

Thesis / Dissertation Reuse

The IEEE does not require individuals working on a thesis to obtain a formal reuse license, however, you may print out this statement to be used as a permission grant:

Requirements to be followed when using any portion (e.g., figure, graph, table, or textual material) of an IEEE copyrighted paper in a thesis:

- 1) In the case of textual material (e.g., using short quotes or referring to the work within these papers) users must give full credit to the original source (author, paper, publication) followed by the IEEE copyright line © 2011 IEEE.
- 2) In the case of illustrations or tabular material, we require that the copyright line © [Year of original publication] IEEE appear prominently with each reprinted figure and/or table.
- 3) If a substantial portion of the original paper is to be used, and if you are not the senior author, also obtain the senior author's approval.

Requirements to be followed when using an entire IEEE copyrighted paper in a thesis:

- 1) The following IEEE copyright/ credit notice should be placed prominently in the references: © [year of original publication] IEEE. Reprinted, with permission, from [author names, paper title, IEEE publication title, and month/year of publication]
- 2) Only the accepted version of an IEEE copyrighted paper can be used when posting the paper or your thesis on-line.
- 3) In placing the thesis on the author's university website, please display the following message in a prominent place on the website: In reference to IEEE copyrighted material which is used with permission in this thesis, the IEEE does not endorse any of [university/educational entity's name goes here]'s products or services. Internal or personal use of this material is permitted. If interested in reprinting/republishing IEEE copyrighted material for advertising or promotional purposes or for creating new collective works for resale or redistribution, please go to http://www.ieee.org/publications_standards/publications/rights/rights_link.html to learn how to obtain a License from RightsLink.

If applicable, University Microfilms and/or ProQuest Library, or the Archives of Canada may supply single copies of the dissertation.

[BACK](#)

[CLOSE WINDOW](#)

ABOUT THE AUTHOR

María F. Córdoba-Erazo was born in Popayán, Colombia. She received the B.S. degree in physics engineering from Universidad del Cauca, Colombia, in 2005 and the M.S. in electrical engineering from University of Puerto Rico at Mayagüez in 2009. Since 2010 she is a Ph.D. student in the Electrical Engineering Department at University of South Florida, Tampa. In fall 2013 she worked as a RF Design Engineer Intern at Qorvo Inc. (former TriQuint Semiconductor). She has been recipient of the DOE-UPRM scholarship in 2008, the 2011 and 2014 USF College of Engineering Best Poster Award, the 2013 IEEE WAMICON Best Student Poster Award, and the 2013 International Microelectronics Assembly and Packaging Society (IMAPS) Best Student Poster Award. In 2014, she was one of the recipients of the ARFTG Roger Pollard Memorial Student Fellowship in Microwave Measurement. She was also one of the recipients of the 2015 IEEE MTT-S Graduate Fellowship.